AN EXPLORATION OF P-TYPE METAL OXIDE SEMICONDUCTORS FOR USE AS A HOLE TRANSPORT LAYER IN SOLAR ENERGY CONVERSION DEVICES

Shannon Marie McCullough

A dissertation submitted to the faculty at the University of North Carolina at Chapel Hill in partial fulfillment of the requirements for the degree of Doctor of Philosophy in the department of chemistry.

Chapel Hill
2018

Approved by:

James Cahoon

Jillian Dempsey

Gerald Meyer

Andrew Moran

Scott Warren

ABSTRACT

Shannon Marie McCullough: An Exploration of p-Type Metal Oxide Semiconductors for Use as a Hole Transport Layer in Solar Energy Conversion Devices
(Under the direction of James Cahoon)

As the global economy continues to develop, the demand for sustainable non-polluting fuel source continues to grow. Different solar energy conversion device architectures provide a variety of advantages and disadvantages. Specifically, moving to a photoelectrochemical cell would synthesize solar fuels obviating the need for a battery. Photoelectrochemical cells employ two photoactive electrodes which motivates the study and improvement of p-type metal oxide photocathode material. Here, several candidates are identified and their viability explored via characterization in a dye-sensitized solar cells (DSSCs).

Nickel oxide, the current champion p-DSSCs, is the first candidate explored. NiO is modified by introducing a shell of Cu_xO on the surface of the NiO electrode to introduce a staggered valence band alignment with the purpose of decreasing recombination. Further investigation on NiO extended into exploration of the various cations used in the electrolyte of the DSSC. Four different cations were tested: Li^+, Mg^{2+}, TBA^+, and Al^{3+}. Compared to the most commonly used cation, Li^+, the use of Mg^{2+} featured several device improvements with a 60 mV increase in V_{OC}. Moving to a novel photocathode material for p-DSSCs, zinc cobalt oxide is next explored. A mechanochemical nanoparticle synthesis is developed with a tunable Zn:Co stoichiometry. The tunable stoichiometry manipulates several significant parameters including bandgap, doping level, and mobility. All stoichiometries of zinc cobalt oxide were tested in

p-DSSCs. Another alternative material for photocathodes that was tested was CuO decorated TiO_2 nanoparticles. By introducing ultrasmall nanoparticles of CuO on the surface of TiO_2 nanoparticles, we can use the electronic properties of CuO while maintaining optical transparency. CuO is also deposited on Al_2O_3 which functions similarly to TiO_2 as a transparent scaffold that supports the CuO ultrananoparticles. The CuO decorated transparent nanoparticles are tested as materials via several physical and chemical techniques including characterization in a p-DSSC.

Throughout the work presented here, several tactics were employed to further understanding and improve performance of p-type metal oxide semiconductors. All the approaches successfully created a hole transport layer within a p-DSSC. Their performances varied with some aspects leaving room for future improvement and some aspects exceeding the benchmark NiO devices.

ACKNOWLEDGEMENTS

To my family and friends, thank you for your support throughout my many years of studies. To my academic adviser, Jim Cahoon, thank you for giving me a spot in your lab. Thank you to the National Science Foundation Graduate Fellowship Program for picking my application to fund. Thank you to the UNC EFRC for scholarly guidance and funding. Thank you to CHANL for all the assistance using equipment and running samples.

TABLE OF CONTENTS

LIST OF FIGURES

LIST OF EQUATIONS

LIST OF TABLES

LIST OF ABBREVIATIONS AND SYMBOLS

Å	Ångström
A	Ampere
AlCuO	CuO decorated Al_2O_3
Al_2O_3	aluminum(III) oxide
ALD	atomic layer deposition
AM1.5G	air mass 1.5 global solar irradiance spectra
$Cu(dmap)_2$	Bis(dimethlyamino-2-propoxy)Copper(II)
C	capacitance
°C	degrees Celsius
cm	centimeter
$Cu(NO_3)_2$	copper(II) nitrate
Cu_2O	copper(I) oxide
CuO	copper(II) oxide
CV	cyclic voltammogram
DOS	density of states
DSPEC	dye-sensitized photoelectrosynthesis cell
DSSC	dye-sensitized solar cell
ε	permittivity
ε_0	permittivity of free space
EDS	energy dispersive spectroscopy
EIS	electrochemical impedance spectroscopy
EMPA	electron micro probe analysis

eV	electron-volt
EQE	external quantum efficiency
FTO	fluorine doped tin oxide
G	conductance
H_2O	water
H_2O_2	hydrogen peroxide
HPC	hydroxypropyl cellulose
Hz	Hertz
I	current
I^-	iodide
I_2	iodine
I_3	triiodide
IDA	interdigitated array
J_0	dark saturation current
J-V	current density-voltage
J_{SC}	short circuit current density
K	Kelvin
L	film thickness
LUMO	lowest unoccupied molecular orbital
M	molarity
min	minute
MIBK	methyl-isobutyl ketone
mA	milliampere

mL	milliliter
mM	millimolar
MMA	methylmethacrylate
mV	millivolt
μm	micrometer (micron)
N_D	doping level
n-DSSC	n-type dye-sensitized solar cell
NiO	nickel(II) oxide
nm	nanometer
nmol	nanomolar
p	porosity
$PbTiO_3$	lead titanate
PCE	power conversion efficiency
p-DSSC	p-type dye-sensitized solar cell
PMMA	polymethylmethacrylate
PXRD	powder x-ray diffraction
q	fundamental charge
R_{CT}	charge transfer resistance
R_S	series resistance
R_{SH}	shunt resistance
SEM	scanning electron microscopy
SILAR	successive ionic layer adsorption and reaction
SnO_2	tin(IV) oxide

TEM	transmission electron microscopy
TiCuO	CuO decorated TiO_2
TiO_2	titanium(IV) dioxide
UPS	ultraviolet photoelectron spectroscopy
UVO	ultraviolet-ozone
UV-vis	ultraviolet-visible
VBE	valence band edge
V	volt
V_{FB}	flatband potential
V_{oc}	open circuit voltage
wt. %	weight percentage
XPS	x-ray photoelectron spectroscopy
$ZnCo_2O_4$	zinc cobalt oxide
$ZnCo_2(OH)_6$	zinc cobalt hydroxide
ZnO	zinc(II) oxide

Chapter 1: Introduction

1.1 Grand Scientific Challenges

Anthropogenic climate change largely caused by increased atmospheric carbon dioxide (CO_2) concentrations has become a pressing concern for the global community. Specifically, climate change poses several grand challenges to our scientific community and to our community on a global scale. Challenges include providing a reliable and renewable fuel source, decreasing future emissions as developing nations industrialize, and tackling the problem of excess atmospheric CO_2.[1] Currently, fossil fuels, such as coal and petroleum, provide a stable and inexpensive fuel source in our increasingly industrialized world. Unfortunately, the consumption of fossil fuels also produces significant pollution that impacts every facet of our lives. Consequently, we are motivated to find an alternative that is both as reliable and inexpensive as fossil fuels, and there is a great impetus to focus research on exploring more environmentally friendly options to fuel the globe.

1.2 Renewable Energy and Solar Energy Conversion

Presently, we employ several types of renewable energy including wind, solar, geothermal, biomass, and hydroelectric power. In the United States today, approximately 10% of total energy consumption is sourced from a combination of all those renewable sources. However, only approximately 0.6% of total energy consumption comes from solar energy conversion despite solar energy's abundance.[2] Although solar energy conversion only contributes a small percentage of today's total energy consumption, creating improved devices with higher efficiencies and lower

costs can increase the effectiveness solar energy conversion.

Among renewables, solar energy conversion provides several unique benefits. First, solar energy is abundant and far reaching. Each day sufficient solar irradiance reaches the Earth to meet the global energy requirements for over 27 years at current consumption rates. Harnessing only a fraction of the daily solar irradiance would more than exceed our global daily requirements for consumption. Solar energy is also fairly ubiquitous, especially when compared to hydropower that requires a river or tidal energy that requires hospitable coastline. Essentially, the sun reaches anywhere humans inhabit, which makes solar energy conversion a promising prospect for the future.

However, a fundamental challenge that solar energy conversion faces is the diurnal nature of the sun. Not only does the sun set each night, common weather events such as clouds can also prevent sunlight from reaching a device on any given day. Also, solar irradiation reaches the Earth at various intensities depending on location. For example, in the United States, the southwest (Arizona, New Mexico, Nevada) receives more days of sunshine than other portions of the country such as the Ohio River Basin. Using a solar fuels approach enables the solar energy to be stored in a transportable molecule, which allows us to imagine highly efficient solar fuel farms in Arizona that fuel the rest of the nation.

A large majority of current solar energy conversion uses photovoltaic cells. Photovoltaic cells or solar-to-electric devices offer a "use or lose" proposition. The generated electricity needs to be either used immediately or stored in some kind of a battery. Beyond photovoltaics which produce electricity from sunlight, we can envision a sunlight driven device that mirrors the processes and products of natural photosynthesis. The result is a dye-sensitized photoelectrosynthesis cell (DSPEC) (Figure 1.1) which can, in principle, use a combination of

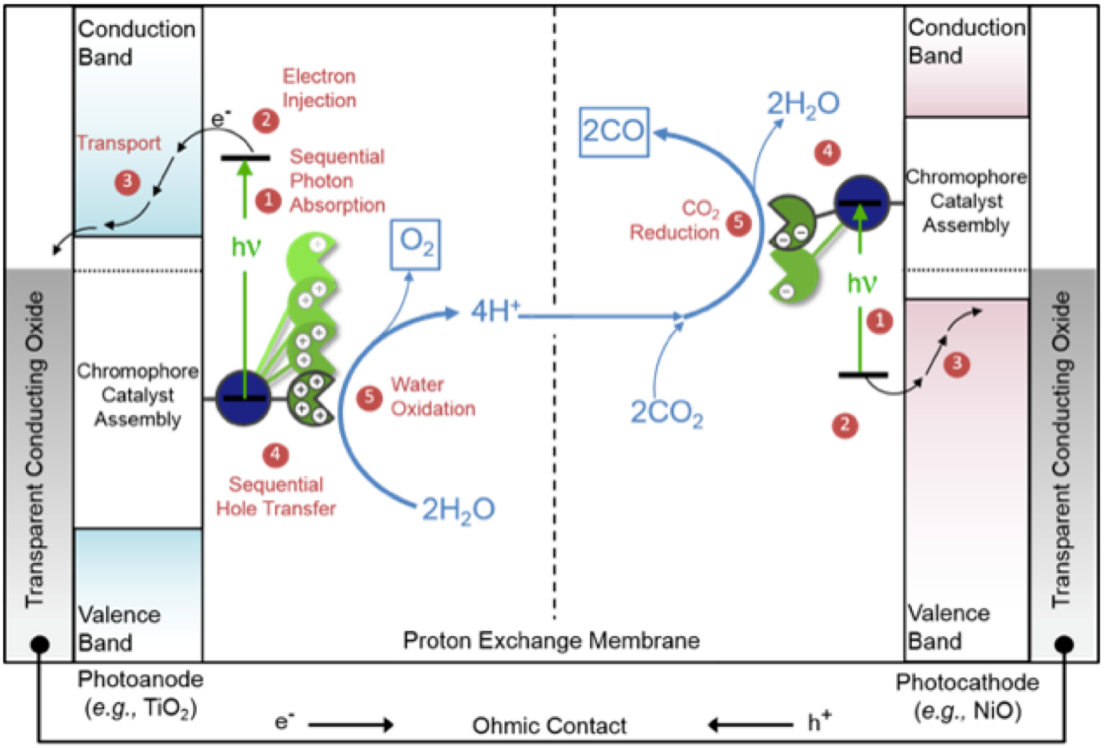

Figure 1.1. The dye-sensitized photoelectrosynthesis cell. The design features H_2O oxidation on the photoanode and CO_2 reduction on the photocathode side. The device includes two mesoporous electrodes with chromophore-catalyst assemblies adsorbed to them. Two half cells are separated by a proton exchange membrane and the cell is filled with an aqueous electrolyte. Image courtesy of UNC EFRC Center for Solar Fuels.

functional materials and molecules that work synchronistically to produce a solar fuel, a reduced hydrocarbon molecule. Producing a solar fuel sequesters atmospheric CO_2 and also prevents future emissions from being produced, motivating the use of a solar fuel approach as a long-run target.

Consequently, to provide a stable, storable fuel source, the DSPEC approach works when and where the solar energy is available, and the solar fuel products can be stored until needed. Another fundamental benefit of a solar fuels approach is that the DSPEC would produce a solar fuel that can be stored over months or even years similarly to how fossil fuels are stored. Additionally, using a solar fuel such as methane allows for the current infrastructure to still be used. Moreover, the DSPEC can be part of a closed loop system where the reduced hydrocarbon

cycles through a fuel cell, then the CO_2 produced from the combustion is cycled back through the DSPEC ad infinitum which is another factor that makes the target architecture of a DSPEC even more desirable.[3,4] The development of a high-efficiency photocathode is critical for the DSPEC which motivates the work presented in this thesis.

1.3 Metal Oxide Electrodes in Photoelectrochemical and Photovoltaic Devices

Using a mesoporous metal oxide electrode in place of a silicon electrode provides several benefits and challenges. A primary benefit of a metal oxide electrode is the lower production cost. The processing of a mesoporous nanoparticulate film is relatively facile compared to a silicon photovoltaic and using abundant elements helps maintain low costs as well. Additionally, using a mesoporous film enables the sensitization of the electrode using a large library of functional molecules. Featuring a dye-molecule as the absorbing entity instead of the electrode material itself allows for higher tunability in absorbance such that we can better match the solar spectrum. Additionally, using an electrode that can easily be sensitized or modified with a molecular entity opens the door to future work with surface bound catalysts as envisaged in the DSPEC design.

By using a tandem design with two photoactive electrodes, we can create sufficient photovoltage by connecting the electrodes in series to drive the required reactions (i.e. >1.5 V for water splitting) and also absorb a greater portion of the solar irradiance spectrum by using complementary absorbers on each half cell. In order to achieve a successful tandem design, all of the distinct components of the device architecture must work at equivalent efficiencies, and to most efficiently improve and to better understand the device, the strategy we employ is to separate individual components and pursue their development in parallel. By using a half-cell device with a dye-sensitized solar cell (DSSC) architecture, only one electrode is photoactive, and we can pursue advancement of each photoelectrode in parallel. In a p-type DSSC, we can study the

photocathode's ability to transport holes in an electrochemical environment using a molecular sensitizer (Figure 1.2) in a simpler design to more quickly isolate issues with the material and advance performance. DSSC efficiency is a useful benchmark for photocathode performance and can be predictive of efficiencies in a future DSPEC application. With respect to the two photoelectrodes current records, the photoanode in an n-type DSSC (n-DSSC) significantly outpaces the photocathode in a p-type DSSC (p-DSSC) for all figures of merit with record photoconversion efficiencies (PCE) for the TiO_2 photoanode reaching over 14% while the record PCE for a NiO photocathode has only reached 2.5% thus far.[5,6] Moving towards a tandem architecture, both photoanode and photocathode need to perform equivalently efficiently for optimal performance overall, and therefore additional efforts to improve the photocathode continue, and the work presented here focuses on p-type metal oxide semiconductors which can be used in a photocathode with emphasis on improving known materials and also developing new

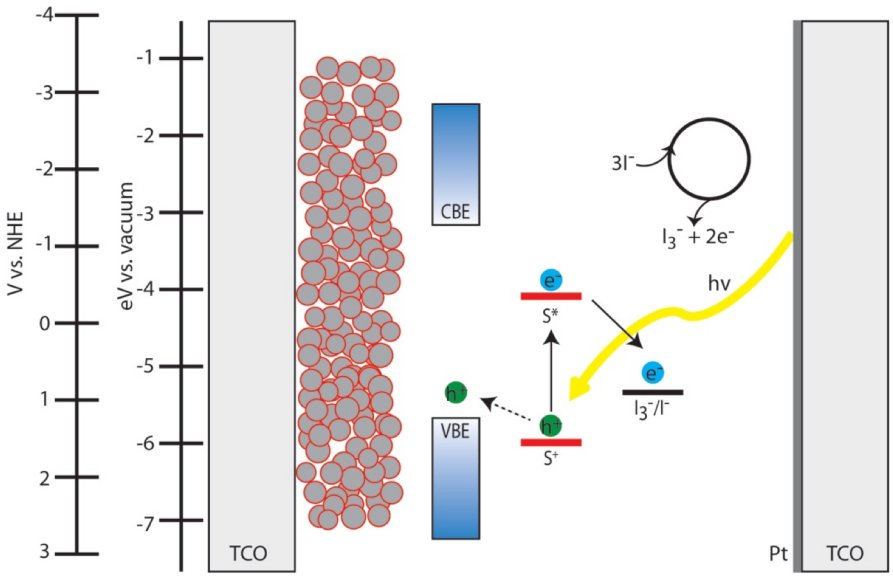

Figure 1.2. p-DSSC. The mesoporous wide bandgap metal oxide features a valence band edge sufficiently more positive on the vacuum energy scale (more negative on the electrochemical potential scale) compared the molecular sensitizer's excited state reductive potential such that a hole can inject into the metal oxide's band. The DSSC features an I^-, I_3^- redox mediator and a Pt counter electrode.

materials that are viable in the DSPEC architecture. When considering what type of material can be used as a photocathode, several constraints immediately present themselves. The material must feature a wide bandgap to maintain optical transparency and prevent competitive absorbance with the molecular sensitizers. The material must be stable under the operating conditions of the cell, so the material must be insoluble and not degrade under illumination. The design of the cell requires a high surface-area electrode, so a nanoparticulate mesoporous electrode film is desirable to keep dye-loading sufficiently high. Additionally, the material's electronic properties are critical when considering a hole transport layer, and consequently, conductivity, doping level, and mobility are all significant properties to consider. Band positions of several strong candidates for photocathode materials are shown in Figure 1.3. Another crucial consideration is the energetic position of the valence band edge of the specific semiconductor. The DSPEC depends on all of the materials and molecules working together with respect to the electrochemical potentials of all the components. Given all these constraints only a few known materials emerge as candidates for the photocathode electrode material. Materials of interest include nickel oxide (NiO), copper(I) delafossites, cobalt spinels, $PbTiO_3$, and copper(I) oxide among others.[7–14] Additionally, the crystal structures of several commonly used metal oxides in DSSCs are shown in Figure 1.4.

We address the goal of identifying a high-efficiency photocathode with a twofold approach. First, we use the current champion material, NiO, and improve upon it, and a second one we can explore an entirely different material to replace the NiO. From the first report in 1999 to the champion report in 2015, NiO has been the primary photocathode material studied in p-DSSCS.[6,7,15–20] NiO has several advantageous properties which make it a desirable candidate for

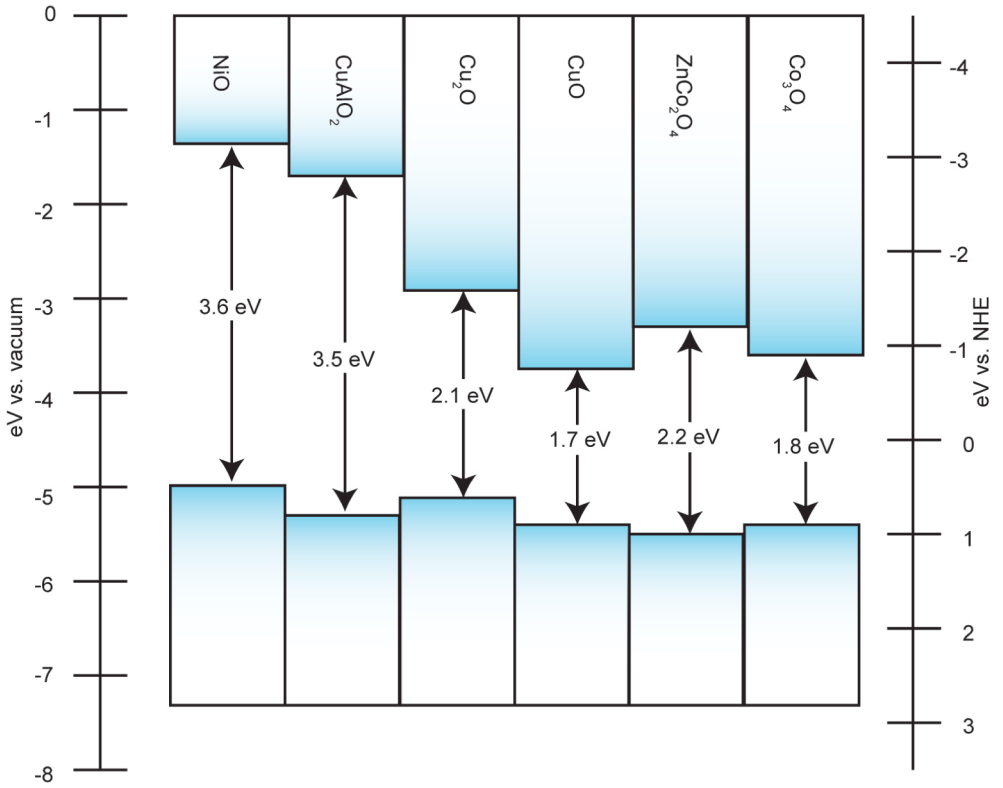

Figure 1.3. Band positions and bandgaps of several known p-type metal oxide semiconductors with valence band edges appropriate for use in a DSSC or DSPEC.

the hole transport layer in dye-sensitized devices including a 3.6 eV bandgap, facile nanoparticle synthetic techniques, and an appropriate valence band edge position. However, NiO also has presented challenges in producing high-efficiency results that match TiO_2 n-DSSCs. The biggest challenge facing NiO photocathodes is high rates of recombination. Recombination manifests several ways in a DSSC including low fill factors and low photocurrents measured in devices.[18,20–23] Several reports on modifying the photocathode material itself have been published including doping NiO with lithium and cobalt, various synthetic and post-processing studies, and several surface modifications.[7,17,20,22–32]

The second tactic we can employ is replacing NiO with an entirely different material. A few classes of p-type metal oxides including copper(I) delafossites provide an interesting

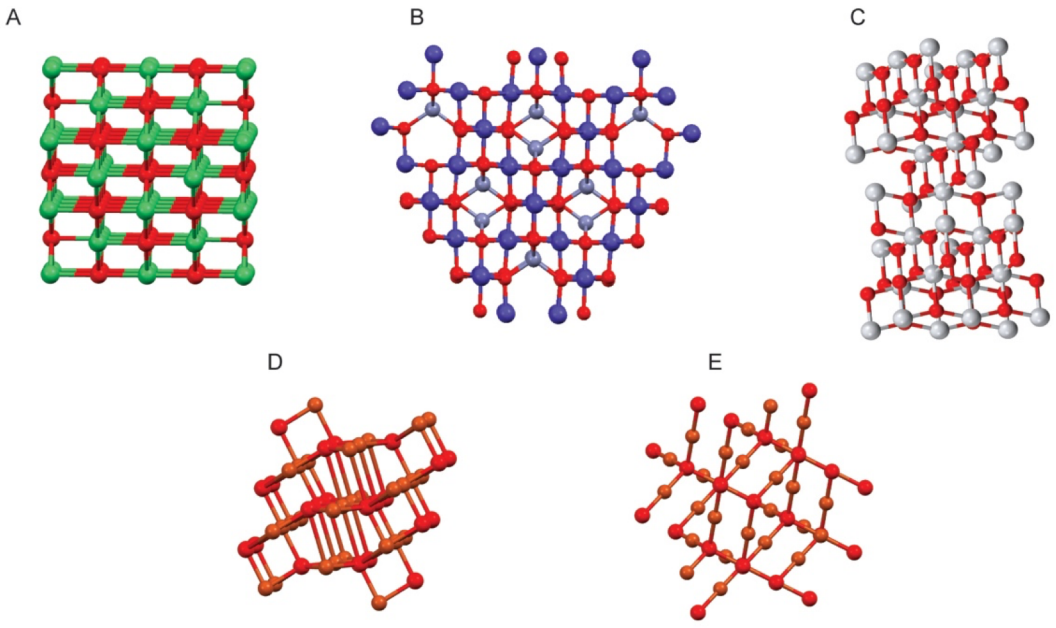

Figure 1.4. Crystal structures of several metal oxides used as DSSC electrodes. (A) Nickel oxide in a rock salt lattice. Green= nickel, red = oxygen. (B) Zinc cobalt oxide in a spinel lattice. Purple = cobalt, grey = zinc, red = oxygen. (C) white = titanium, red = oxygen. (D) Copper(II) oxide in a monoclinic lattice. Orange = copper, red = oxygen. (D) Copper(I) oxide in a cubic lattice.

alternative to NiO. Copper(I) delafossites have the general formula of $CuMO_2$ which feature monovalent Cu^+ and a trivalent cation which often is Al^{3+}, Ga^{3+}, Cr^{3+}, or B^{3+}. Advantages of using a copper(I) delafossite is the tunable wide bandgap (3.0-3.6 eV), a deeper valence band position (-5.2 to -5.5 eV vs. vacuum), and high conductivities.[13,33–37] Delafossites present several challenges as well, including poor crystallinity, low surface area electrodes, lattice strain, and difficult synthetic routes. Another class of ternary metal oxides viable for alternative photocathode materials includes cobalt-based spinels of the general formula, $M_xCo_{3-x}O_4$. M is a divalent cation which is often Co^{2+}, Zn^{2+}, or Ni^{2+}. Spinels feature a valence band edge appropriately positioned around -5.5 eV vs. vacuum and reasonable conductivities. However, a primary concern in pursuing spinels as a mesoporous photocathode is the small bandgap (~2 eV), although the bandgap is

tunable depending on which divalent cation is present in the lattice. Further exploration of zinc cobalt oxide is presented later in this report.

Beyond the electrode material, a DSSC also requires a sensitizer and an electrolyte which all operate in sync to create a successful device, and explicit focus on each component is critical for continued improvement. When transitioning from n-DSSCs to a p-DSSCs, the general device design is completely analogous with the opposite direction of net charge flow. Holes inject into the valence band of the p-type semiconductor in p-DSSCs rather than electrons injecting into the conduction band of the n-type semiconductor. Consequently, several adjustments must occur when designing a p-DSSC for optimal performance. For example, tuning a molecule's design such that the lowest unoccupied molecular orbital (LUMO) is spatially removed from the linker group and, therefore the metal oxide surface, increases charge separation and helps reduce surface recombination. Studies focusing on the sensitizing chromophore have also increased NiO p-DSSC efficiency by tuning the molecule's properties to the needs of the device and continued focus on chromophore design will be critical for the future of p-DSSCs.[38–46] In the data reported here, we use a commercially available molecular chromophore P1 which is a useful benchmark used for comparison across systems.[22,23,27,47,48]

Despite the challenges inherent in using a p-type metal oxide semiconductor in a DSSC, the high performance of n-DSSCs and the long-run target of creating a tandem DSPEC cell continue to motivate study on p-DSSCs. In fact, the continued efforts on understanding and improving n-DSSCs provides some insight on the most important physical and chemical parameters for device performance. Extensive studies have been published on n-DSSCs since the first report in 1991. TiO_2 is still the champion material for the photoanode, and it has been extensively characterized in the n-DSSC configuration.[49–53] In addition to TiO_2, alternatives n-type

metal oxides such as ZnO and SnO_2 have been investigated in n-DSSCs on their own and in architectures that combine more than one metal oxide.[54–62] By introducing a different electrode architecture, core-shell structures provide a new parameter space to explore, and the success of core-shell structures using TiO_2 as the core material and SnO_2 as the shell material in an n-DSSC motivates pursing a core-shell architecture for a photocathode as well.[63–67]

1.4 Photovoltaic Analysis

The general goal of high-efficiency devices is simultaneously both specific and vague. High efficiency is specific in that the objective is clear—a device that produces the most power per unit area. However, the goal is also vague in that the best path to use en-route to achieving a high-efficiency device is indeterminate. Consequently, we use several figures of merit to characterize solar-to-electric photovoltaic cells regardless of the type of electrode used or the design of the cell to compare performance across systems. Typically, performance metrics are collected using a current-voltage (*J-V*) curve which can be modeled using the ideal diode equation in accordance with DSSC convention:

$$J = J_{ph} - J_o\left(e^{\left(\frac{qV}{nk_BT}\right)} - 1\right), \tag{1.1}$$

where J is total current, J_{ph} is photocurrent, J_0 is the dark saturation current, q is the fundamental charge, n is the ideality factor, k_B is the Boltzmann constant, and T is temperature. Several figures of merit are extracted from *J*-V curves with open-circuit voltage (V_{OC}), short-circuit current density (J_{SC}), fill factor (FF), and power conversion efficiency (PCE) being the most commonly cited performance metrics. Power conversion efficiency is defined as:

$$PCE = \frac{V_{OC}J_{SC}FF}{P_{in}} \times 100\% = \frac{P_{max}}{P_{in}} \times 100\%, \tag{1.2}$$

where P_{in} is the incident power on the device, and P_{max} is the maximum power produced by the device. From Equation 1.2, it is evident that maximizing the V_{oc}, J_{sc}, and FF are all key targets for device performance maximization which is true for all photovoltaic devices including DSSCs. PCE encompasses all of the parameters which effect device performance in one expression, and PCE is a critical figure of merit, especially when comparing across photovoltaic systems and when considering commercialization. However, by unpacking the PCE expression, components detrimental to device performance can be identified and feasibly improved. Specifically, parasitic resistances play a significant role in p-DSSCs and cause deviations from ideal behavior. Shunt resistances (R_{SH}) ideally are infinite so that no alternative pathways are available for current flow. Low R_{SH} present in many p-DSSCs significantly decreases PCE and most notably decreases the FF. Additionally, high series resistances (R_S) negatively impact device performance by introducing unwanted resistance in pathways current is designed to flow. Introducing series resistance (R_S) modifies the ideal diode equation to yield:

$$J = J_{ph} - J_0 e^{\left(\frac{q(V+JR_S)}{nk_BT}\right)} \tag{1.3}$$

and introducing shunt resistance (R_{SH}) modifies the ideal diode equation to yield:

$$J = J_{ph} - J_0 e^{\left(\frac{qV}{nk_BT}\right)} - \frac{V}{R_{SH}} \tag{1.4}$$

Shunt and series resistances are calculated using experimental *J-V* curves by taking the linear region around J_{SC} for R_{SH} and V_{OC} for R_S and using the inverse of the slope from the line of best fit for the resistance value.

The influence of both R_S and R_{SH} can be most clearly observed in the fill factor, or the squareness of the *J-V* curve. Fill factor is defined as:

$$FF = \frac{V_{MP}J_{MP}}{V_{OC}J_{SC}} \times 100\% \quad (1.5)$$

where V_{MP} and J_{MP} are the voltage and current at the maximum power point on the *J-V* curve respectively. NiO p-DSSCs typically feature low FFs compared to TiO_2 n-DSSCs, and identifying the causes for decreases in FF or parasitic resistances can help elevate the p-DSSC performances to match n-DSSCs. Parasitic resistances also pose a problem for alternative materials for the photocathode such as $ZnCo_2O_4$ as discussed in Chapter 5.

1.5 Vetting Known Materials and Exploring Alternatives for DSSCs

Initially, a core-shell morphology is explored using NiO as the core material and CuO or Cu_2O as the shell material. When choosing materials for both the core and the shell, various conditions must be met, but the most critical is the valence band edge position energetically. The core-shell architecture of NiO/Cu_xO features a staggered valence band alignment that introduces an energetic staircase for the injected hole to cascade through. The staggered band alignment imposes an energetic penalty of either 0.2 V for Cu_2O or 0.4 V for CuO on a hole in the valence band to recombine. Core-shell morphologies have proven successful for the n-type photoanodes, although no report of a p-type core-shell electrode has been previously published.[63–66]

A core-shell design poses a synthetic challenge where the material demands an ultra-thin layer of the shell material (Cu_xO) of no more than a few nanometers thick with conformal quality over a heterogeneous scaffold. Typical synthetic approaches such as sputtering, pulsed laser deposition, and electron beam evaporation that produce films with thicknesses on nanometer length scale are directional in nature. Only a select few deposition techniques are viable for depositing a conformal coating on the mesoporous NiO film, and a successive ionic layer absorption and reaction (SILAR) technique and an atomic layer deposition (ALD) technique are

employed to introduce the conformal shell of Cu_xO. The deposition process and the NiO/Cu_xO photocathodes' performance is delineated in detail in Chapter 3.

When considering improving a photocathode, the focus typically lies on the material itself, and the metal oxide receives a majority of the attention. An alternative avenue to pursue in conjunction is adapting the environment the photocathode operates in. A fully assembled and operational device operates with molecular sensitizers on the metal oxide's surface and features the dye-loaded electrode immersed in an electrolyte solution. Within the electrolyte solution, the most critical components are the redox mediators, in this case the I^- and I_3^-. However, there are additional spectator ions also present in the electrolyte. The introduction of the charged particles interacting with the metal oxide's surface capacitive double layer effects can occur and ultimately the flatband potential (V_{FB}) shifts. By explicitly considering the cations' impact on the V_{FB}, the introduction of specific species can improve the device performance. The effects of cations and other additives in the electrolyte solution has received thorough study for n-type DSSCs. However, no systematic reports for p-type DSSCs have been yet reported. The results in Chapter 4 explores the effects of various cations in a p-type DSSC with NiO as the electrode material.[49,68–72]

Addressing the photocathode problem from a different angle, we explore a new photocathode material, zinc cobalt oxide ($ZnCo_2O_4$). In the search for an alternative to NiO, the current champion metal oxide photocathode material, several targets must be met including p-type conductivity, a wide bandgap, high surface area, and a valence band edge ideally between -5.0 and -5.5 eV vs. vacuum. After all of those considerations are met only a few viable candidates from known reports remain including copper delafossites and cobalt spinels. Cobalt spinels are a mixed metal oxide with a spinel crystal structure. With two distinct sites for metal ions within the lattice, typically for $ZnCo_2O_4$, the Zn^{2+} occupies a tetrahedrally coordinated site and the Co^{3+} occupies a

octahedrally coordinated site. As is true for many transition metals, cobalt ions are multivalent with the most common oxidation states of 2^+ and 3^+, and a pure cobalt oxide spinel (Co_3O_4) exists where the cobalt is in both the tetrahedral and octahedral position. Co_3O_4 is p-type and features other desirable characteristics, but a drawback is its small bandgap of 1.8 eV. The introduction of zinc widens the bandgap to 2.2 eV, and a controllable mechanochemical synthetic process is developed in detail. Several ratios of Zn:Co were chemically and electronically characterized with the ultimate characterization being their device performance in a p-DSSC. The complete report is presented in Chapter 5.

Lastly, Chapter 6 explores another alternative photocathode material, CuO decorated TiO_2 nanoparticles. A consistent challenge when moving from bulk materials to nanomaterials is that bulk characteristics which are often used to select a material do not necessarily translate to the nanoscale. Frequently this discrepancy is disadvantageous for the functionality of a nanomaterial. For example, electronic properties such as mobility for a bulk metal oxide is typically several orders of magnitude higher than a nanomaterial of the same chemical composition. Specifically, nanoparticulate NiO films typically feature a mobility on the order of 10^{-6} $cm^2/(Vs)$ whereas a bulk NiO film features a mobility on the order of 10^0 $cm^2/(Vs)$.[7,73] Conversely, the discrepancy between nano and bulk materials is often used advantageously. For example, the highly reactive surface area of metal and metal oxides is frequently used for catalysis.[74–80]

DSSCs use a nanoparticulate mesoporous film to increase surface area for a molecular dye. The use of a nanoparticulate semiconductor also decreases processing costs for the devices. Beyond the increased surface area and low production costs, the nanoparticulate nature of a DSSC electrode is rarely leveraged in unexpected ways. In this report, we use the reactive surface sites on a transparent metal oxide to allow for nucleation of ultrasmall CuO nanoparticles. The

deposition of the CuO in sufficiently small particles (~2 nm in diameter) maintains optical transparency which enables the use of CuO, a material typically eliminated from contention for use as a photocathode because of its small bandgap of 1.7 eV. By designing a material that controls the morphology of the CuO on the surface of the TiO_2, we can introduce enough of the p-type material such that a sufficient density of states is available for hole-injection from the chromophore without introducing debilitating competitive absorbance. Further exploration is conveyed in Chapter 6.

REFERENCES

(1) Omenn, G. S. Grand Challenges and Great Opportunities in Science, Technology, and Public Policy. *Science.* **2006**, *314* (5806), 1696–1704.

(2) U.S. Energy Information Administration, Monthly Energy Review, Table 1.3 and 10.1, April 2017, preliminary data.

(3) Brennaman, M. K.; Dillon, R. J.; Alibabaei, L.; Gish, M. K.; Dares, C. J.; Ashford, D. L.; House, R. L.; Meyer, G. J.; Papanikolas, J. M.; Meyer, T. J. Finding the Way to Solar Fuels with Dye-Sensitized Photoelectrosynthesis Cells. *J. Am. Chem. Soc.* **2016**, *138* (40), 13085–13102.

(4) Alibabaei, L.; Brennaman, M. K.; Norris, M. R.; Kalanyan, B.; Song, W.; Losego, M. D.; Concepcion, J. J.; Binstead, R. A.; Parsons, G. N.; Meyer, T. J. Solar Water Splitting in a Molecular Photoelectrochemical Cell. *Proc. Nat. Acad. Sci. USA* **2013**, *110*, 20008–20013.

(5) Kakiage, K.; Aoyama, Y.; Yano, T.; Oya, K.; Fujisawa, J.; Hanaya, M. Highly-Efficient Dye-Sensitized Solar Cells with Collaborative Sensitization by Silyl-Anchor and Carboxy-Anchor Dyes. *Chem. Commun.* **2015**, *51* (88), 15894–15897.

(6) Perera, I. R.; Daeneke, T.; Makuta, S.; Yu, Z.; Tachibana, Y.; Mishra, A.; Bäuerle, P.; Ohlin, C. A. A.; Bach, U.; Spiccia, L.; et al. Application of the tris(acetylacetonato)iron(III)/(II) Redox Couple in P-Type Dye-Sensitized Solar Cells. *Angew. Chemie - Int. Ed.* **2015**, *54* (12), 3758–3762.

(7) Flynn, C. J.; Oh, E. E.; McCullough, S. M.; Call, R. W.; Donley, C. L.; Lopez, R.; Cahoon, J. F. Hierarchically-Structured NiO Nanoplatelets as Mesoscale P-Type Photocathodes for Dye-Sensitized Solar Cells. *J. Phys. Chem. C* **2014**, *118* (26), 14177–14184.

(8) Brisse, R.; Faddoul, R.; Bourgeteau, T.; Tondelier, D.; Leroy, J.; Campidelli, S.; Berthelot, T.; Geffroy, B.; Jousselme, B. Ink-Jet Printing NiO-Based P-Type Dye Sensitized Solar Cells. *ACS Appl. Mater. Interfaces* **2017**, *9* (3), 2369–2377.

(9) Nattestad, A.; Ferguson, M.; Kerr, R.; Cheng, Y.-B.; Bach, U. Dye-Sensitized nickel(II)oxide Photocathodes for Tandem Solar Cell Applications. *Nanotechnology* **2008**, *19* (29), 295304.

(10) Yu, M.; Draskovic, T. I.; Wu, Y. Cu(I)-Based Delafossite Compounds as Photocathodes in P-Type Dye-Sensitized Solar Cells. *Phys. Chem. Chem. Phys.* **2014**, *16* (11), 5026–5033.

(11) Moot, T.; Isayev, O.; Call, R. W.; McCullough, S. M.; Zemaitis, M.; Lopez, R.; Cahoon, J. F.; Tropsha, A. Material Informatics Driven Design and Experimental Validation of Lead Titanate as an Aqueous Solar Photocathode. *Mater. Discov.* **2017**, *6*, 1–8.

(12) McCullough, S. M.; Flynn, C. J.; Mercado, C. C.; Nozik, A. J.; Cahoon, J. F. Compositionally-Tunable Mechanochemical Synthesis of Zn X Co 3−x O 4 Nanoparticles for Mesoporous P-Type Photocathodes. *J. Mater. Chem. A* **2015**, *3*, 21990–21994.

(13) Jiang, T.; Bujoli-Doeuff, M.; Farré, Y.; Blart, E.; Pellegrin, Y.; Gautron, E.; Boujtita, M.; Cario, L.; Odobel, F.; Jobic, S. Copper Borate as a Photocathode in P-Type Dye-Sensitized Solar Cells. *RSC Adv.* **2016**, *6* (2), 1549–1553.

(14) Mercado, C. C.; Zakutayev, A.; Zhu, K.; Flynn, C. J.; Cahoon, J. F.; Nozik, A. J. Sensitized Zinc–Cobalt–Oxide Spinel P-Type Photoelectrode. *J. Phys. Chem. C* **2014**, *118* (44), 25340–25349.

(15) He, J.; Lindström, H.; Hagfeldt, A.; Lindquist, S.-E. Dye-Sensitized Nanostructured P-Type Nickel Oxide Film as a Photocathode for a Solar Cell. *J. Phys. Chem. B* **1999**, *103*, 8940–8943.

(16) Powar, S.; Daeneke, T.; Ma, M. T.; Fu, D.; Duffy, N. W.; Gotz, G.; Weidelener, M.; Mishra, A.; Bauerle, P.; Spiccia, L.; et al. Highly Efficient P-Type Dye-Sensitized Solar Cells Based on tris(1,2-diaminoethane)cobalt(II)/(III) Electrolytes. *Angew. Chemie - Int. Ed.* **2013**, *52* (2), 602–605.

(17) Natu, G.; Hasin, P.; Huang, Z.; Ji, Z.; He, M.; Wu, Y. Valence Band-Edge Engineering of Nickel Oxide Nanoparticles via Cobalt Doping for Application in P-Type Dye-Sensitized Solar Cells. *ACS Appl. Mater. Interfaces* **2012**, *4* (11), 5922–5929.

(18) Daeneke, T.; Yu, Z.; Lee, G. P.; Fu, D.; Duffy, N. W.; Makuta, S.; Tachibana, Y.; Spiccia, L.; Mishra, A.; Bauerle, P.; et al. Dominating Energy Losses in NiO P-Type Dye-Sensitized Solar Cells. *Adv. Energy Mater.* **2015**, *5* (4).

(19) Zhang, X. L.; Huang, F.; Nattestad, A.; Wang, K.; Fu, D.; Mishra, A.; Bäuerle, P.; Bach, U.; Cheng, Y.-B. Enhanced Open-Circuit Voltage of P-Type DSC with Highly Crystalline NiO Nanoparticles. *Chem. Commun. (Camb).* **2011**, *47* (16), 4808–4810.

(20) Wei, L.; Jiang, L.; Yuan, S.; Ren, X.; Zhao, Y.; Wang, Z.; Zhang, M.; Shi, L.; Li, D. Valence Band Edge Shifts and Charge-Transfer Dynamics in Li-Doped NiO Based P-Type DSSCs. *Electrochim. Acta* **2016**, *188*, 309–316.

(21) D'Amario, L.; Antila, L. J.; Pettersson Rimgard, B.; Boschloo, G.; Hammarström, L. Kinetic Evidence of Two Pathways for Charge Recombination in NiO-Based Dye-Sensitized Solar Cells. *J. Phys. Chem. Lett.* **2015**, *6* (5), 779–783.

(22) Flynn, C. J.; McCullough, S. M.; Oh, E.; Li, L.; Mercado, C. C.; Farnum, B. H.; Li, W.; Donley, C. L.; You, W.; Nozik, A. J.; et al. Site-Selective Passivation of Defects in NiO Solar Photocathodes by Targeted Atomic Deposition. *ACS Appl. Mater. Interfaces* **2016**, *8*, 4754–4761.

(23) Huang, Z.; Natu, G.; Ji, Z.; Hasin, P.; Wu, Y. P-Type Dye-Sensitized NiO Solar Cells : A Study by Electrochemical Impedance Spectroscopy. *J. Phys. Chem. C* **2011**, *115* (50),

25109–25114.

(24) Sharma, R.; Acharya, A. D.; Shrivastava, S. B.; Shripathi, T.; Ganesan, V. Preparation and Characterization of Transparent NiO Thin Films Deposited by Spray Pyrolysis Technique. *Opt. - Int. J. Light Electron Opt.* **2014**, *125* (22), 6751–6756.

(25) Kerli, S.; Alver, U.; Yaykaşlı, H. Investigation of the Properties of In Doped NiO Films. *Appl. Surf. Sci.* **2014**, 2–5.

(26) Shan, B.; Sherman, B. D.; Klug, C. M.; Nayak, A.; Marquard, S. L.; Liu, Q.; Bullock, R. M.; Meyer, T. J. Modulating Hole Transport in Multilayered Photocathodes with Derivatized P-Type Nickel Oxide and Molecular Assemblies for Solar-Driven Water Splitting. *J. Phys. Chem. Lett.* **2017**, 4374–4379.

(27) Wood, C. J.; Summers, G. H.; Clark, C. A.; Kaeffer, N.; Braeutigam, M.; Carbone, L. R.; D'Amario, L.; Fan, K.; Farré, Y.; Narbey, S.; et al. A Comprehensive Comparison of Dye-Sensitized NiO Photocathodes for Solar Energy Conversion. *Phys. Chem. Chem. Phys.* **2016**, *18*, 10727–10738.

(28) D'Amario, L.; Boschloo, G.; Hagfeldt, A.; Hammarström, L. Tuning of Conductivity and Density of States of NiO Mesoporous Films Used in P-Type DSSCs. *J. Phys. Chem. C* **2014**, *118* (34), 19556–19564.

(29) Dini, D.; Halpin, Y.; Vos, J. G.; Gibson, E. a. The Influence of the Preparation Method of NiOx Photocathodes on the Efficiency of P-Type Dye-Sensitized Solar Cells. *Coord. Chem. Rev.* **2015**, *304–305*, 179–201.

(30) Powar, S.; Daeneke, T.; Ma, M. T.; Fu, D.; Duffy, N. W.; Götz, G.; Weidelener, M.; Mishra, A.; Bäuerle, P.; Spiccia, L.; et al. Highly Efficient P-Type Dye-Sensitized Solar Cells Based on tris(1,2-diaminoethane)cobalt(II)/(III) Electrolytes. *Angew. Chemie - Int. Ed.* **2013**, *52* (2), 602–605.

(31) Ho, P.; Bao, L. Q.; Ahn, K.-S.; Cheruku, R.; Kim, J. H. P-Type Dye-Sensitized Solar Cells: Enhanced Performance with a NiO Compact Blocking Layer. *Synth. Met.* **2016**, *217*, 314–321.

(32) Natu, G.; Huang, Z.; Ji, Z.; Wu, Y. The Effect of an Atomically Deposited Layer of Alumina on NiO in P-Type Dye-Sensitized Solar Cells. *Langmuir* **2012**, *28* (1), 950–956.

(33) Santra, S.; Das, N. S.; Chattopadhyay, K. K. $CuBO_2$: A New Photoconducting Material. *AIP Conf. Proc.* **2013**, *1536* (1), 723–724.

(34) Santra, S.; Das, N. S.; Chattopadhyay, K. K. Sol–gel Synthesis and Characterization of Wide Band Gap P-Type Nanocrystalline CuBO2. *Mater. Lett.* **2013**, *92*, 198–201.

(35) Renaud, A.; Chavillon, B.; Le Pleux, L.; Pellegrin, Y.; Blart, E.; Boujtita, M.; Pauporté, T.; Cario, L.; Jobic, S.; Odobel, F. CuGaO2: A Promising Alternative for NiO in P-Type Dye Solar Cells. *J. Mater. Chem.* **2012**, *22* (29), 14353.

(36) Xu, Z.; Xiong, D.; Wang, H.; Zhang, W.; Zeng, X.; Ming, L.; Chen, W.; Xu, X.; Cui, J.; Wang, M.; et al. Remarkable Photocurrent of P-Type Dye-Sensitized Solar Cell Achieved by Size Controlled CuGaO2 Nanoplates. *J. Mater. Chem. A* **2014**, *2* (9), 2968.

(37) Xiong, D.; Xu, Z.; Zeng, X.; Zhang, W.; Chen, W.; Xu, X.; Wang, M.; Cheng, Y. B. Hydrothermal Synthesis of Ultrasmall CuCrO2 Nanocrystal Alternatives to NiO Nanoparticles in Efficient P-Type Dye-Sensitized Solar Cells. *J. Mater. Chem.* **2012**, 24760–24768.

(38) Bao, L. Q.; Ho, P.; Chitumalla, R. K.; Jang, J.; Thogiti, S.; Kim, J. H. Single and Double Branched Organic Dyes Based on Carbazole and Red-Absorbing Cationic Indolium for P-Type Dye-Sensitized Solar Cells: A Combined Experimental and Theoretical Investigation. *Dye. Pigment.* **2017**.

(39) Le Pleux, L.; Smeigh, A. L.; Gibson, E.; Pellegrin, Y.; Blart, E.; Boschloo, G.; Hagfeldt, A.; Hammarström, L.; Odobel, F. Synthesis, Photophysical and Photovoltaic Investigations of Acceptor-Functionalized Perylene Monoimide Dyes for Nickel Oxide P-Type Dye-Sensitized Solar Cells. *Energy Environ. Sci.* **2011**, *4* (6), 2075.

(40) Sheibani, E.; Zhang, L.; Liu, P.; Xu, B.; Mijangos, E.; Boschloo, G.; Hagfeldt, A.; Hammarström, L.; Kloo, L.; Tian, H. A Study of Oligothiophene-Acceptor Dyes in P-Type Dye-Sensitized Solar Cells. *RSC Adv.* **2016**, 18165–18177.

(41) Qin, P.; Zhu, H.; Edvinsson, T.; Boschloo, G.; Hagfeldt, A.; Sun, L. Design of an Organic Chromophore for P-Type Dye-Sensitized Solar Cells. *J. Am. Chem. Soc.* **2008**, *130* (27), 8570–8571.

(42) Wu, F.; Zhu, L.; Zhao, S.; Song, Q.; Yang, C. Engineering of Organic Dyes for Highly Efficient P-Type Dye-Sensitized Solar Cells. *Dye. Pigment.* **2016**, *124*, 93–100.

(43) Lyu, S.; Farré, Y.; Ducasse, L.; Pellegrin, Y.; Toupance, T.; Olivier, C.; Odobel, F. Push–pull Ruthenium Diacetylide Complexes: New Dyes for P-Type Dye-Sensitized Solar Cells. *RSC Adv.* **2016**, *6* (24), 19928–19936.

(44) Bonomo, M.; Barbero, N.; Matteocci, F.; Di Carlo, A.; Barolo, C.; Dini, D. Beneficial Effect of Electron Withdrawing Groups on the Sensitizing Action of Squaraines for P-Type Dye Sensitized Solar Cells. *J. Phys. Chem. C* **2016**, *120* (30), 16340–16353.

(45) Zhang, F.; Yu, P.; Shen, W.; Li, M.; He, R. Effect of "push-Pull" Sensitizers with Modified Conjugation Bridges on the Performance of P-Type Dye-Sensitized Solar Cells. *RSC Adv.* **2015**.

(46) Hao, Y.; Wood, C. J.; Clark, C. A.; Calladine, J. A.; Horvath, R.; Hanson-Heine, M. W. D.; Sun, X.-Z.; Clark, I. P.; Towrie, M.; George, M. W.; et al. Can Aliphatic Anchoring Groups Be Utilised with Dyes for P-Type Dye Sensitized Solar Cells? *Dalt. Trans.* **2016**, *46*, 7708–7719.

(47) Ahmed, J.; Blakely, C. K.; Prakash, J.; Bruno, S. R.; Yu, M.; Wu, Y.; Poltavets, V. V.

Scalable Synthesis of Delafossite $CuAlO_2$ Nanoparticles for P-Type Dye-Sensitized Solar Cells Applications. *J. Alloys Compd.* **2014**, *591*, 275–279.

(48) Yu, M.; Natu, G.; Ji, Z.; Wu, Y. P-Type Dye-Sensitized Solar Cells Based on Delafossite $CuGaO_2$ Nanoplates with Saturation Photovoltages Exceeding 460 mV. *J. Phys. Chem. Lett.* **2012**, *3* (9), 1074–1078.

(49) Jeanbourquin, X. A.; Li, X.; Law, C.; Barnes, P. R. F.; Humphry-Baker, R.; Lund, P.; Asghar, M. I.; Oregan, B. C. Rediscovering a Key Interface in Dye-Sensitized Solar Cells: Guanidinium and Iodine Competition for Binding Sites at the Dye/electrolyte Surface. *J. Am. Chem. Soc.* **2014**, *136* (20), 7286–7294.

(50) Xie, M.; Bai, F. Q.; Wang, J.; Kong, C. P.; Chen, J.; Zhang, H. X. Theoretical Description of Dye Regeneration on the TiO_2-Dye-Electrolyte Model. *Comput. Mater. Sci.* **2016**, *111*, 239–246.

(51) Kim, D. H.; Losego, M. D.; Hanson, K.; Alibabaei, L.; Lee, K.; Meyer, T. J.; Parsons, G. N. Stabilizing Chromophore Binding on TiO_2 for Long-Term Stability of Dye-Sensitized Solar Cells Using Multicomponent Atomic Layer Deposition. *Phys. Chem. Chem. Phys.* **2014**, *16*, 8615–8622.

(52) Salvador, P.; Hidalgo, M. G.; Zaban, A.; Bisquert, J. Illumination Intensity Dependence of the Photovoltage in Nanostructured TiO_2 Dye-Sensitized Solar Cells. *J. Phys. Chem. B* **2005**, *109* (33), 15915–15926.

(53) Mosconi, E.; Selloni, A.; De Angelis, F. Solvent Effects on the Adsorption Geometry and Electronic Structure of Dye-Sensitized TiO2: A First-Principles Investigation. *J. Phys. Chem. C* **2012**, *116* (9), 5333–5341.

(54) Qian, J.; Liu, P.; Xiao, Y.; Jiang, Y.; Cao, Y.; Ai, X.; Yang, H. TiO_2-Coated Multilayered SnO_2 Hollow Microspheres for Dye-Sensitized Solar Cells. *Adv. Mater.* **2009**, *21* (36), 3663–3667.

(55) Lee, J. H.; Park, N. G.; Shin, Y. J. Nano-Grain SnO_2 Electrodes for High Conversion Efficiency SnO2DSSC. *Sol. Energy Mater. Sol. Cells* **2011**, *95* (1), 179–183.

(56) Justin Raj, C.; Karthick, S. N.; Dennyson Savariraj, A.; Hemalatha, K. V.; Park, S. K.; Kim, H. J.; Prabakar, K. Electrochemical Properties of TiO_2 Encapsulated ZnO Nanorod Aggregates Dye Sensitized Solar Cells. *J. Alloys Compd.* **2012**, *537*, 159–164.

(57) Lee, C. H.; Chiu, W. H.; Lee, K. M.; Yen, W. H.; Lin, H. F.; Hsieh, W. F.; Wu, J. M. The Influence of Tetrapod-like ZnO Morphology and Electrolytes on Energy Conversion Efficiency of Dye-Sensitized Solar Cells. *Electrochim. Acta* **2010**, *55* (28), 8422–8429.

(58) Ku, C.-H.; Wu, J.-J. Electron Transport Properties in ZnO Nanowire Array/nanoparticle Composite Dye-Sensitized Solar Cells. *Appl. Phys. Lett.* **2007**, *91* (9), 93117.

(59) Gubbala, S.; Chakrapani, V.; Kumar, V.; Sunkara, M. K. Band-Edge Engineered Hybrid

Structures for Dye-Sensitized Solar Cells Based on SnO_2 Nanowires. *Adv. Funct. Mater.* **2008**, *18* (16), 2411–2418.

(60) Martinson, A. B. F.; Elam, J. W.; Hupp, J. T.; Pellin, M. J. ZnO Nanotube Based Dye-Sensitized Solar Cells. *Nano Lett.* **2007**, *7* (8), 2187.

(61) Ko, S. H.; Lee, D.; Kang, H. W.; Nam, K. H.; Yeo, J. Y.; Hong, S. J.; Grigoropoulos, C. P.; Sung, H. J. Nanoforest of Hydrothermally Grown Hierarchical ZnO Nanowires for a High Efficiency Dye-Sensitized Solar Cell. *Nano Lett.* **2011**, *11* (2), 666–671.

(62) Ramasamy, E.; Lee, J. Ordered Mesoporous SnO_2 −Based Photoanodes for High-Performance Dye-Sensitized Solar Cells. *J. Phys. Chem. C* **2010**, *114* (50), 22032–22037.

(63) Diamant, Y.; Chappel, S.; Chen, S. G.; Melamed, O.; Zaban, A. Core-Shell Nanoporous Electrode for Dye Sensitized Solar Cells: The Effect of Shell Characteristics on the Electronic Properties of the Electrode. *Coord. Chem. Rev.* **2004**, *248* (13–14), 1271–1276.

(64) Gish, M. K.; Lapides, A. M.; Brennaman, M. K.; Templeton, J. L.; Meyer, T. J.; Papanikolas, J. M. Ultrafast Recombination Dynamics in Dye-Sensitized SnO_2 /TiO_2 Core/Shell Films. *J. Phys. Chem. Lett.* **2016**, 5297–5301.

(65) Wee, K.-R.; Sherman, B. D.; Brennaman, M. K.; Sheridan, M. V.; Nayak, A.; Alibabaei, L.; Meyer, T. J. An Aqueous, Organic Dye Derivatized SnO_2/TiO_2 Core/shell Photoanode. *J. Mater. Chem. A* **2016**, *4* (8), 2969–2975.

(66) Sherman, B. D.; Ashford, D. L.; Lapides, A. M.; Sheridan, M. V.; Wee, K. R.; Meyer, T. J. Light-Driven Water Splitting with a Molecular Electroassembly-Based Core/Shell Photoanode. *J. Phys. Chem. Lett.* **2015**, *6* (16), 3213–3217.

(67) Knauf, R. R.; Kalanyan, B.; Parsons, G. N.; Dempsey, J. L. Charge Recombination Dynamics in Sensitized SnO_2/TiO_2 Core/Shell Photoanodes. *J. Phys. Chem. C* **2015**, *119* (51), 28353–28360.

(68) Gupta, R. K.; Bedja, I. Cationic Effect on Dye-Sensitized Solar Cell Properties Using Electrochemical Impedance and Transient Absorption Spectroscopy Techniques. *J. Phys. D-Applied Phys.* **2017**, *50*, 245501–245507.

(69) O'Donnell, R. M.; Sampaio, R. N.; Barr, T. J.; Meyer, G. J. Electric Fields and Charge Screening in Dye Sensitized Mesoporous Nanocrystalline TiO_2 Thin Films. *J. Phys. Chem. C* **2014**, *118* (30), 16976–16986.

(70) Kelly, C. A.; Farzad, F.; Thompson, D. W.; Stipkala, J. M.; Meyer, G. J. Cation-Controlled Interfacial Charge Injection in Sensitized Nanocrystalline TiO_2. *Langmuir* **1999**, *15* (20), 7047–7054.

(71) Watson, D. F.; Meyer, G. J. Cation Effects in Nanocrystalline Solar Cells. *Coord. Chem. Rev.* **2004**, *248* (13–14), 1391–1406.

(72) Wang, H.; Peter, L. M. Influence of Electrolyte Cations on Electron Transport and Electron Transfer in Dye-Sensitized Solar Cells. *J. Phys. Chem. C* **2012**, *116* (19), 10468–10475.

(73) Osburn, C. M.; Vest, R. W. Defect Structure and Electrical Properties of NiO—I. High Temperature. *J. Phys. Chem. Solids* **1971**, *32* (6), 1331–1342.

(74) Guo, S.; Zhang, S.; Sun, S. Tuning Nanoparticle Catalysis for the Oxygen Reduction Reaction. *Angew. Chemie - Int. Ed.* **2013**, *52* (33), 8526–8544.

(75) Xia, Y.; Yang, H.; Campbell, C. T. Nanoparticles for Catalysis. *Acc. Chem. Res.* **2013**, *46* (8), 1671–1672.

(76) Rodriguez, J. A.; Hanson, J. C.; Frenkel, A. I.; Kim, J. Y.; Pérez, M. Experimental and Theoretical Studies on the Reaction of H_2 with NiO: Role of O Vacancies and Mechanism for Oxide Reduction. *J. Am. Chem. Soc.* **2002**, *124* (2), 346–354.

(77) Harriman, A.; Pickering, I. J.; Thomas, J. M.; Christensen, P. A. Metal Oxides as Heterogeneous Catalysts for Oxygen Evolution under Photochemical Conditions. *J. Chem. Soc. Faraday Trans. 1 Phys. Chem. Condens. Phases* **1988**, *84* (8), 2795.

(78) Haruta, M. When Gold Is Not Noble: Catalysis by Nanoparticles. *Chem. Rec.* **2003**, *3* (2), 75–87.

(79) Liu, Z.-P.; Gong, X.-Q.; Kohanoff, J.; Sanchez, C.; Hu, P. Catalytic Role of Metal Oxides in Gold-Based Catalysts: A First Principles Study of CO Oxidation on TiO_2 Supported Au. *Phys. Rev. Lett.* **2003**, *91* (26), 266102.

(80) Oelerich, W.; Klassen, T.; Bormann, R. Metal Oxides as Catalysts for Improved Hydrogen Sorption in Nanocrystalline Mg-Based Materials. *J. Alloys Compd.* **2001**, *315* (1–2), 237–242.

Chapter 2: Experimental Methods

2.1 Analytical Characterization Techniques

Ultraviolet-visible (UV-vis) spectroscopy was performed on an Agilent Cary 5000 UV-Vis-NIR spectrophotometer with a scan rate of 600 nm per minute and an integrating sphere attachment. Film thicknesses were measured using a KLA Tencor P-6 Stylus Profiler by using step height analysis. Powder x-ray diffraction (PXRD) patterns were collected using a Rigaku Multiflex Diffractometer with a Cu $\alpha 1$ source, 1 mm slit widths, and a 2° 2θ per minute. PXRD patterns were either collected using bulk powder or on thin films prepared on glass substrates. Resistance measurements were performed using Au microelectrode patterns fabricated on silicon nitride wafers with a methylmethacrylate/polymethymethacrylate (MMA/PMMA) resist stack. The microelectrode pattern was defined using electron beam lithography on a JC Nabity Lithography system, and the metallic electrode material (3 nm Cr adhesion layer followed by 100 nm Au) was deposited using electron beam evaporation on a Thermionics VE-100 system. The metal oxide thin film was spincast on top of the fabricated Au microelectrode pattern and calcined at 450 °C unless otherwise noted. Resistance measurements were taken using a Keithley 2636A SourceMeter and Signatone micromanipulators (S725) with probetips (SE-TL). Scanning electron microscopy was performed using a FEI Helios 600 Nanolab Dual Beam Focused Ion Beam System. Bulk energy dispersive spectroscopy (EDS) was measured using an INCA PentaFet –x3 system installed on the FEI Helios instrument. Transmission electron microscopy was performed on either a FEI Titan 80-300 probe aberration corrected scanning transmission

electron microscope with a Bruker 4 SDD EDS system for EDS mapping or a FEI Tecnai Osiris digital 200 kV S/TEM with ChemiSTEM EDX signal detection. X-ray photoelectron spectroscopy (XPS) and ultraviolet photoelectron spectroscopy (UPS) was performed on a Kratos Axis Ultra DLD x-ray photoelectron spectrometer.

2.2 Electrochemical Analysis

Electrochemical analysis was performed using a three electrode cell with the metal oxide film as the working electrode, a Pt mesh counter electrode, and an Ag/AgCl reference electrode. The supporting electrolyte is a 0.1 M $LiClO_4$ acetonitrile solution unless otherwise noted. Three electrode cell measurements were executed on a CH Instruments 604E potentiostat. Cyclic voltammograms (CVs) were collected using a 0.02 V/s scan rate. The density of states (DOS) were calculated using the equation

$$\mathrm{DOS} = \mathrm{C}/[(1-\mathrm{p}) * \mathrm{L} * \mathrm{q}] \quad \textbf{(2.1)}$$

where C is the capacitance (current density/scan rate), p is the porosity of the metal oxide film, L is the film thickness, and q is the fundamental charge. Mott-Schottky analysis was performed using a variety of frequencies ranging from 1-1000 Hz. The linear portion of the Mott-Schottky $1/C^2$ plot is fit to a regression line. From the fitted line, the x-intercept is the flat band potential (V_{FB}) and the slope corresponds to the doping level. The doping level (N_D) is calculated from the following equation

$$slope = \frac{2}{\varepsilon\varepsilon_0 N_D q^2} \quad \textbf{(2.2)}$$

where ε is the permittivity of the material being measured, ε_0 is the permittivity of free space, N_D is the doping level, and q is the fundamental charge. Electrochemical impedance spectroscopy

(EIS) was performed on a Gamry Reference 600 electrochemical impedance spectrometer and modeled using a double-Randles circuit. EIS measurements were performed using a two electrode system, both the counter and reference electrodes were a Pt electrode and the working electrode was the metal oxide film on FTO. Conductance measurements were performed using a CH Instruments 760E bipotentiostat on a platinum interdigitated array (IDA) electrode purchased from CH Instruments. The desired metal oxide material was spin-cast and annealed on top of the IDA electrode at 600 °C for 40 minutes. An external Ag/AgCl reference electrode was used in a three electrode cell set up with a 1.0 M $LiClO_4$ acetonitrile electrolyte. Conductance (G) was calculated using the following equation:

$$G = \frac{I_1 + I_2}{2 * \text{bias}} \quad \textbf{(2.3)}$$

where I_1 and I_2 are the currents measured from working electrode 1 and working electrode 2 respectively.

2.3 Metal Oxide Nanoparticle Syntheses and Preparations

2.3.a Cu_2O thin film deposition on NiO nanoparticles via SILAR

Cu_2O was deposited using a successive ionic layer adsorption and reaction (SILAR) technique using a modified literature technique.[1] The SILAR deposition was performed by dipping substrate in a $Cu(NO_3)_2$ ammonia solution followed by a 30% H_2O_2 solution with deionized H_2O rinses in between. The successive dipping was performed manually on the benchtop at room temperature. Each step lasted for 20 seconds, and the deposition continued until the desired number of cycles was achieved.

2.3.b CuO thin film deposition on NiO nanoparticles via ALD

CuO was deposited using atomic layer deposition (ALD) Ultratech/Cambridge Nanotech Savannah S200 system. The precursors used for CuO deposition were bis(dimethylamino-2-propoxy)Cu(II) ($Cu(dmap)_2$) and distilled H_2O. A nitrogen carrier gas was used for all ALD deposition. The precursor was heated to 85 °C. The reactor chamber was heated to 120 °C. The Cu precursor pulse time was 2 seconds, and the H_2O pulse time was 0.015 seconds. After each reactor pulse, a 90 second wait time occurred. No more than four samples were placed in the chamber at during any given deposition.

2.3.c Zinc Cobalt Oxide Nanoparticle Synthesis

A mechanochemical synthesis of $Zn_xCo_{3-x}O_4$ was developed using zinc nitrate, cobalt nitrate, and sodium hydroxide which produced a $Zn_xCo_{3-x}(OH)_6$ as an intermediate. The preparation was done by combining the appropriate ratios of the metal salts and sodium hydroxide in an agate mortar and pestle on the open bench top. Although the preparation was done without any addition of solvent, all of the precursors are highly hygroscopic and working in a humid environment introduced a non-negligible quantity of water to the synthesis. The precursors were ground together manually for three minutes in an agate mortar and pestle. The $Zn_xCo_{3-x}(OH)_6$ was then rinsed with water and dried at 40 °C overnight. To convert to $Zn_xCo_{3-}xO_4$, the $Zn_xCo_{3-x}(OH)_6$ was calcined in a quartz boat at 450 °C in a box furnace. The stoichiometry of the Zn and Co was controlled by adjusting the ratios of the metal salts used in the synthesis. Complete experimental details are detailed in Chapter 5.

2.3.d CuO Decorated TiO_2 Nanoparticle Synthesis

CuO ultrasmall nanoparticles were deposited on commercially purchased TiO_2 or Al_2O_3 nanoparticles using a Teflon lined non-stirring pressure reactor. The TiO_2 nanoparticles were

submerged in a $Cu(NO_3)_2 \cdot 3H_2O$ aqueous solution and held at 80 °C for one week. The reactor was left to cool to room temperature ambiently. The powder was then collected via centrifugation, rinsed with 50 mL water, and dried at 40 °C. Complete experimental details are detailed in Chapter 7.

2.4 Nanoparticle Spin-Coating Paste Preparation

To process the metal oxide nanoparticles into mesoporous thin films, various spin-coating pastes were prepared. The general procedure involved combining the metal oxide nanoparticles with ethyl cellulose, ethanol, and α-terpineol. The paste was then homogenized using sonication, ball milling, and vigorous mechanical stirring. After homogenization, the spin-coating paste was stored in a covered glass jar at room temperature with constant mechanical stirring. If the paste became too viscous caused by solvent evaporation over time, additional ethanol was added as needed. Films were cast on the desired substrate using a Laurell WS-650Mz-23NPP spin coater. Films were spun at 100 rpm for 5 seconds followed by 1000 rpm for 30 seconds unless otherwise noted. The films were typically calcined in a box furnace at temperatures ranging from 300-600 °C for 40 minutes.

2.5 Dye-Sensitized Solar Cell Fabrication

Dye-sensitized solar cells (DSSCs) were fabricated using the mesoporous metal oxide nanoparticle film as the working electrode on fluorine doped tin oxide (FTO). Post-calcination, the metal oxide film was dye-loaded using a 0.1 mM solution of commercially available molecular chromophore, P1, in acetonitrile. The molecular structure of P1 is drawn in Figure 2.1. After removing the dye-loaded film from the loading solution, the film was rinsed with ~3 mL of acetonitrile and then dried using nitrogen gas. The active area of the film was defined by trimming

to the selected area by manually removing the excess material using a Kimwipe. The remaining active area was typically ~0.5 cm^2. The active area of each film was measured manually using a ruler. A counter electrode was fabricated by dropcasting a 5 mM H_2PtCl_6 solution in isopropanol

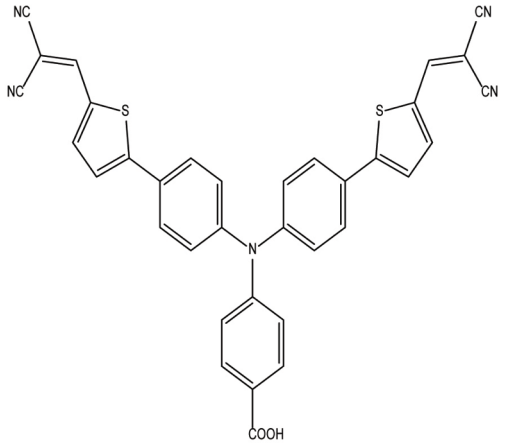

Figure 2.1. Molecular structure of the chromophore P1. The carboxylic acid group links to the metal oxide surface.

onto an FTO slide followed by a calcination at 380 °C for 30 minutes. The counter electrode had a manually sandblasted pinhole placed in the upper corner used to fill the electrolyte. The dyed film (working electrode) is then sandwiched with the counter electrode using a 25 μm thick Surlyn gasket as a spacer. The Surlyn was heated to 150 °C with pressure applied for approximately 10 seconds using a homebuilt system to seal the devices. The assembled device was vacuum back-filled through the sandblasted pinhole with an electrolyte typically consisting of a 10:1 LiI:I_2 acetonitrile solution unless otherwise specified using a homebuilt vacuum chamber. The pinhole of the filled DSSC was sealed using a piece of the Surlyn polymer and a microscope coverslip heated for five seconds using a Gecko heat press set at 150 °C. Complete experimental details on DSSC assembly are conveyed in Chapters 3-6.

2.6 Dye-Sensitized Solar Cell Characterization

DSSC characterization consisted of current density-voltage (*J-V*) scans using a AM 1.5G illumination source and a Keithley 2636A SourceMeter for all photovoltaic measurements. Devices where scanned from negative bias to positive bias usually starting at -0.2 V and scanning to 0.3 V. First, the device was scanned in the dark immediately followed by scanning in the light. Blackout curtains were used to create a completely dark container for measuring dark curves, and the blackout curtains were used to prevent any additional light to reach the device besides the one-sun illumination. The direction of illumination was through the working electrode first. A typical sample size for one set of devices was four. The one-sun illumination was calibrated to a Newport 91150 V reference solar cell prior to each use. External quantum efficiency (EQE) measurements were collected on fully assembled DSSCs using a Newport Instruments tungsten lamp and a Princeton Instruments SP-2300 spectrometer with a 1200 g/mm grating.

REFERENCES

(1) Pathan, H. M.; Lokhande, C. D. Deposition of Metal Chalcogenide Thin Films by Successive Ionic Layer Adsorption and Reaction (SILAR) Method. *Bull. Mater. Sci.* **2004**, *27* (2), 85–111.

Chapter 3: Ultrathin Layers of Copper Oxide on Nickel Oxide Photocathodes

3.1 Introduction

Achieving artificial photosynthesis, where the goal is the synthesis of a reducing carbon dioxide into a hydrocarbon molecule, would enable a solar-to-fuel system that stores the incident solar energy in a stable chemical fuel. Similar to the photosynthetic systems found in plants, a dye-sensitized photoelectrosynthesis cell (DSPEC) requires a tandem or Z-scheme design with two active photoelectrodes connected in series to produce sufficient photovoltage for required reactions. An additional requirement for maximized efficiency is that the photocurrent must be matched from the photoanode and the photocathode. When considering each photoelectrode, the current champion materials are TiO_2 for the photoanode and NiO for the photocathode, and the peak performance of TiO_2 significantly outpaces that of NiO.[1,2] Consequently, to realize a high-efficiency tandem cell, specific focus and analysis on the photocathode material in a dye-sensitized solar cell (DSSC) architecture is employed. Using a DSSC design, which is a solar-to-electric approach, allows us to probe the performance of the hole transport layer in a more straightforward fashion.

Over the past 19 years, considerable effort has been put forth to improve NiO as an electrode material for use in a p-type DSSC, although a core-shell morphology has yet to be reported.[2–13] Using NiO as the core electrode features several desirable qualities including stability, high surface area, facile syntheses and appropriate p-type conductivity. However, NiO also features some undesirable properties with high recombination rates being the most problematic for

a DSSC application.[8,14–20] One tactic used to combat the high surface recombination is to modifythe surface entirely with a new material, which physically encapsulates the NiO surface entirely and separates the NiO from direct contact with the electrolyte. Previous reports of successful core-shell geometries for n-type metal oxide DSSC electrodes indicate that the structure is viable for these types of metal oxide electrodes in general, and this architecture allows for the desirable characteristics of the core material and the shell material to be exploited.[21–26] By introducing an ultrathin shell material on top of the NiO nanoparticle scaffold in a core-shell architecture, we can introduce a staggered band alignment that will create an energetic barrier to some recombination pathways with an energetic penalty of 400 mV for CuO and 200 mV for Cu_2O for an electron that was injected into the NiO core to move back through to the Cu_XO shell. Highly contributing recombination pathways in NiO p-DSSCs include back electron transfer from the electrolyte or recombination from the excited state dye molecule.[11,13,27]

In choosing an effective material for the shell we need a material that has a valence band edge (VBE) between NiO's VBE at -5.0 eV vs. vacuum and the reductive potential of the chromophore, P1, at -5.88 eV vs. vacuum, p-type conductivity, optical transparency, dye-loading capability, and stability in the electrolyte solution. When looking for a material with those criteria in mind, both Cu_2O and CuO stand out as top contenders. Although both have been extensively characterized as electronic materials on their own, neither has ever been previously reported as a shell material on mesoporous NiO nor been used as an electrode material in a p-DSSC in part because of the small bandgaps of 2.1 eV and 1.7 eV for Cu_2O and CuO respectively. Any material with a bandgap below ~3 eV has typically been excluded from consideration when designing a DSSC. With the DSSC design, a transparent electrode is required such that the molecular dye can absorb the solar radiation without competition. However, because the shells of Cu_2O and CuO are

ultrathin, the competitive absorbance is negligible. Considering all these parameters, the core-shell architecture using NiO as the core and Cu_XO as the shell is reported here.

3.2 Experimental Materials and Methods

3.2.a Materials and reagents

All materials and reagents were used as received. Acetonitrile (HPLC grade), anhydrous α-terpineol, nickel nitrate hexahydrate (puriss, p.a.), copper nitrate trihydrate (puriss, p.a.), lithium iodide (99.9%), and iodine (99.99%) were purchased from Sigma Aldrich. Ethanol (200 proof), ammonium hydroxide (certified ACS plus), and hydrogen peroxide (30% w/w in water) were purchased from Fisher Scientific. NiO nanoparticles were purchased from Inframat. TiO_2 aeroxide nanoparticles were purchased from Acros Organics. FTO was purchased from Hartford glass. Surlyn polymer (25 μm thick) was purchased from Solaronix. P1 was purchased from Dyenamo. Bis(dimethlyamino-2-propoxy)Copper(II) was purchased from Strem for ALD.

3.2.b NiO mesoporous electrode preparation

A NiO spin-coating paste was prepared using a 25 wt. % NiO, 15 wt. %, ethyl-cellulose, 15 wt. % terpineol, and 45 wt. % ethanol. NiO nanoparticles were purchased from Inframat and used as received. NiO nanoplatelets used for imaging were synthesized by dropwise addition of 20 mL of 1.0 M NH_4OH to 980 mL of 0.01 M aqueous solution of $Ni(NO_3)•6H_2O$ at reflux.[28] After addition of all components, the paste was homogenized using mechanical stirring, ball-milling, and sonication. A homogenized paste was spin-cast on FTO glass (Harford glass) substrates using a Laurell WS-650Mz-23NPP spin coater. NiO films were calcined at 450 °C for 40 mins.

3.2.c TiO_2 mesoporous electrode preparation

A TiO_2 spin-coating paste was prepared identically to the NiO spin-coating paste except the NiO nanoparticles were replaced with TiO_2 nanoparticles.

3.2.d Cu_2O thin film deposition

Cu_2O was deposited using a solution of $Cu(NO_3)_2$ in 1 M NH_3 and a 30% H_2O_2 solution, which is a previously reported technique.[29] Films were deposited via manual successive dipping into designated solutions on the benchtop. Each dip lasted for 20 seconds. Post-deposition, the film was blown dry with N_2(g). Selected films were annealed post-deposition using a tube furnace with a controlled ramp rate and a hold temperature of 450 °C and duration of 40 minutes.

3.2.e CuO atomic layer deposition

CuO deposition used bis(dimethlyamino-2-propoxy)Copper(II) as the copper precursor and H_2O was the oxygen precursor. The precursor was heated to 85 °C for 20 minutes prior to deposition. The reactor chamber was heated to 120 °C . The Cu precursor and water pulse times were 2 seconds with 90 second wait times. The films were deposited using an Ultratech Savannah S200. After deposition, selected films were annealed at 450 °C for 40 mins.

3.2.f Cation exchange reaction

NiO nanoparticles (inframat) were suspended in a 1.0 M $Cu(NO_3)$ aqueous solution and mechanically stirred under various temperatures ranging from room temperature to full reflux.

3.2.g Dye-Sensitized Solar Cell assembly

All working electrodes (NiO, NiO/Cu_2O, and NiO/CuO films) were submerged in a 0.1 mM P1 acetonitrile solution overnight to dye-load. Pt counter electrodes were made using chloroplatinic acid dissolved in ethanol. The Pt solution was drop cast on FTO with a pre-fabricated pin hole and calcined at 380 °C for 30 mins. A 25 μm thick Surlyn polymer (Solaronix) gasket was used as a spacer between the two stacked electrodes. Electrolyte solution was prepared using 1.0 M LiI and 0.1 M I_2 in acetonitrile. The assembled devices were backfilled with electrolyte

through the pinhole using a custom built vacuum compartment. Filled devices were sealed with a piece of Surlyn and a microscope coverslip.

3.2.h Analytical techniques

Powder x-ray diffraction measurements were taken on a Rigaku Multiflex diffractometer with a scan rate of 2° 2θ/min on films. Scanning electron microscopy imaging was performed on a FEI Helios NanLab DualBeam D600 Focused Ion Beam System. Optical UV-Vis measurements were collected on a Cary 5000 UV-Vis-NIR spectrometer with an integrating sphere attachment. Electron microprobe analysis was performed on a JXA-8530FPlus Field Emission Electron Probe Microanalyzer. *J-V* measurements were collected using a Newport Oriel 150W Class ABB solar simulator calibrated with a certified reference Newport 91150 V solar cell. A Keithley 2636A SourceMeter was used for electrical measurements.

3.3 Results and Discussion

Cu_xO shells were deposited on NiO mesoporous scaffolds via SILAR for Cu_2O and ALD for CuO. Various numbers of cycles corresponding to various shell thicknesses were studied for both shell materials. The thin film Cu_2O SILAR deposition was first characterized on a planar

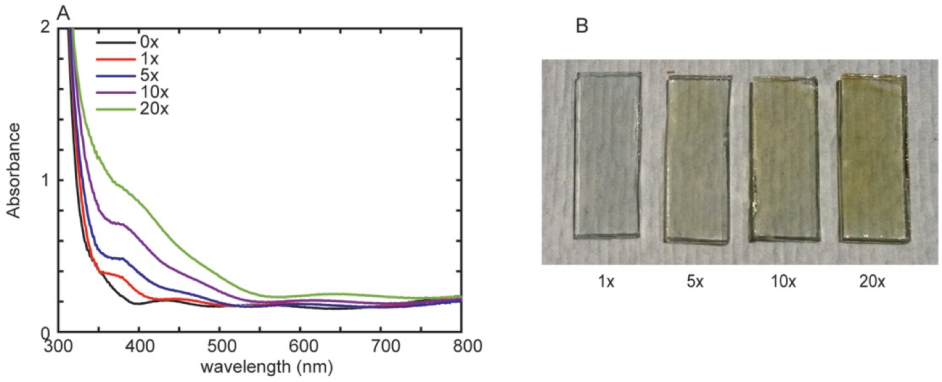

Figure 3.1. Optical characterization of Cu_2O SILAR deposition on a planar substrate. (A) UV-Vis absorbance of Cu_2O SILAR deposition from 0-20 cycles on an FTO substrate. (B) Optical photo of 1, 5, 10, and 20 cycles of Cu_2O SILAR on FTO.

substrate by UV-vis spectroscopy which indicated a 2.1 eV band gap and increasing absorbance as the deposition thickness increases as shown in Figure 3.1. Figure 3.1B features an optical photo of the SILAR Cu_2O deposition on FTO glass demonstrating the orange color and how the ultrathin films are still sufficiently transparent for a DSSC application. Notably, many SILAR depositions result in polycrystalline films with crystal grains as large as 20 nms across.[29–33] However, for this device architecture, a conformal coating of the shell material on the mesoscopic NiO is essential, and, consequently, an amorphous material is necessitated such that the heterogeneous surface is homogeneously covered.

In addition to pursing depositing a homogenous deposition, a cation exchange reaction was investigated. Several materials, including cadmium sulfide, silver sulfide, and lead sulfide, successfully use cation exchange driven by hard-soft acid-base chemistry to complete the reaction.[34–38] Cation exchange can produce precisely controlled geometries of material such as the core-shell structure targeted for NiO/Cu_XO photocathodes, and the target would be to exchange only the first few nanometers of Ni^{2+} with Cu^{2+} or Cu^{+}. In successful cation exchange reactions, the lattice mismatch must be minimized. The cation radii for Ni^{2+}, Cu^{2+}, and Cu^{+} are 0.55 Å, 0.57 Å, and 0.46 Å respectively making the exchange feasible, although the crystal structures of each oxide differ. A cation exchange reaction was attempted using a NiO nanoparticles suspended in a $Cu(NO_3)$ solution. Under reflux conditions, complete exchange was observed, and a pure-phase CuO product was collected. The conversion from the NiO rock salt lattice to the CuO monoclinic lattice are shown in Figure 3.2. Decreasing the temperature of the reaction yielded no exchange

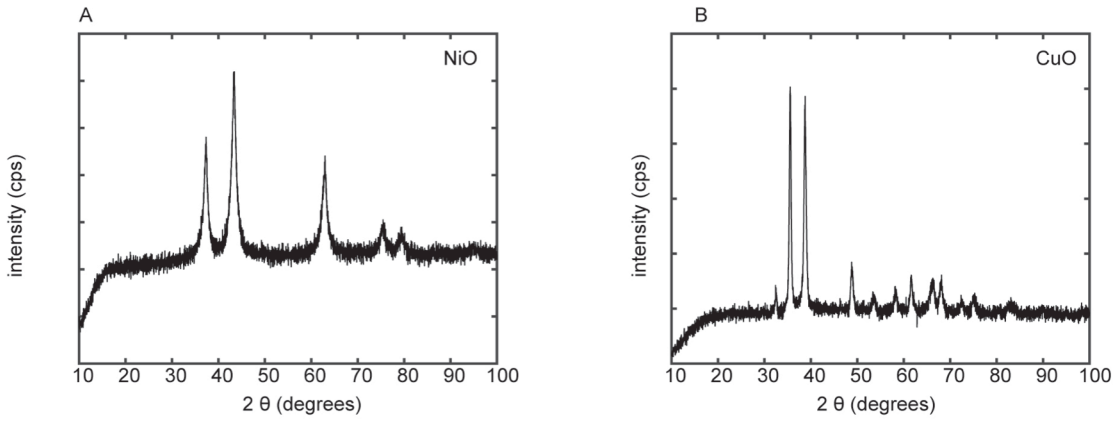

Figure 3.2. Powder x-ray diffraction patterns from Ni^{2+}-Cu^{2+} cation exchange reactions. (A) NiO before reaction. (B) Collected product post reaction indicating pure phase CuO.

within a 24 hour period and other attempts to control the depth of deposition were unsuccessful. Therefore, the alternative deposition technique of atomic layer deposition was explored.

To deposit conformal coatings of copper oxide that are thinner than 1.5 nm, atomic layer deposition (ALD) remains the only viable technique. ALD uses alternating pulses of gaseous precursors to adsorb and react to the oxygen terminated surface of the nano-particulate metal oxide

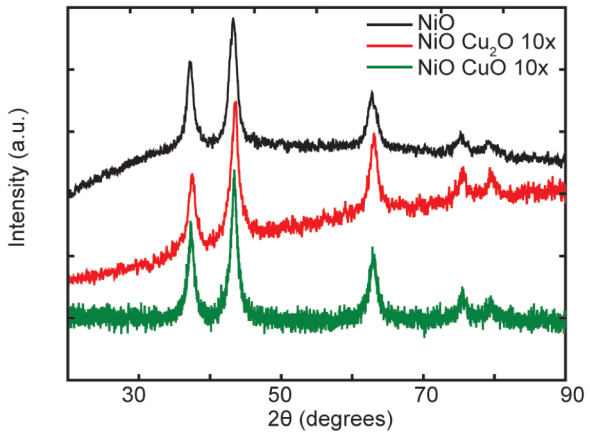

Figure 3.3. Powder x-ray diffraction patterns of NiO, NiO/Cu_2O, and NiO/CuO thin films. Diffraction peaks from only the NiO lattice are observed for all traces indicating amorphous character of the Cu_XO shell.

electrode. Several literature preparations exist for Cu_2O deposition with various copper precursors used including bis(tri-n-butylphosphane)copper acetylacetonate, copper hexafluoroacetylacetonate, and copper diisopropylacetamidinate.[39–45] The ALD deposition reported here uses Bis(dimethylamino-2-propoxy)Cu(II) ($Cu(dmap)_2$) which deposits Cu^{2+} cations and subsequently reacts to form CuO. CuO features a valence band edge (VBE) at -5.4 eV vs. vacuum which is ~400 meV more negative than NiO VBE at -5.0 eV vs. vacuum allowing for hole injection from the dye to the CuO and from the CuO shell into the NiO core.[46] The VBE of CuO at -5.4 eV vs. vacuum is slightly more negative than the VBE of Cu_2O at -5.2 eV vs. vacuum, which would in principle increase the driving force for hole injection from the shell material into the core NiO nanoparticle.

Because the Cu_2O material deposited via SILAR is amorphous, the PXRD patterns feature

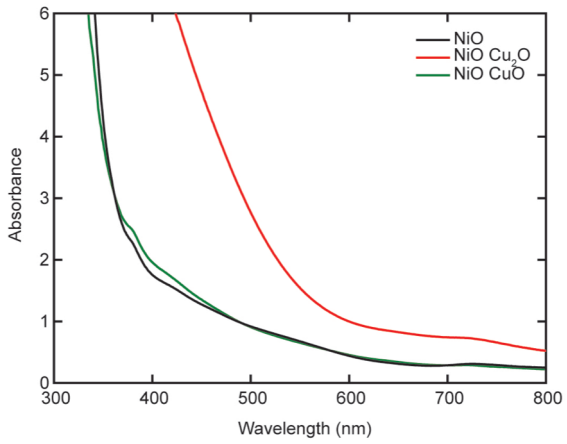

Figure 3.4. UV-vis absorbance of NiO, NiO/Cu_2O, and NiO/CuO thin films with 10 cycles of both Cu_2O and CuO on the NiO scaffold on FTO.

peaks only from the NiO rock salt lattice form the core (Figure 3.3). Additionally, for the CuO ALD deposition, no diffraction peaks are present from a CuO lattice indicating amorphous deposition. Figure 3.3 includes the UV-vis absorbance profile of bare NiO, NiO/Cu_2O, and NiO/CuO materials. As shown in Figure 3.4, a significant increase in absorbance in the range

between 350-600 nm is observed for NiO/Cu_2O as the number of SILAR cycles increases and the shell thickness increases. For the NiO/CuO ALD deposition, a negligible change in absorbance is observed and the absorbance in the visible for the core-shell material is nearly identical to the bare NiO because the CuO shell is ultrathin.

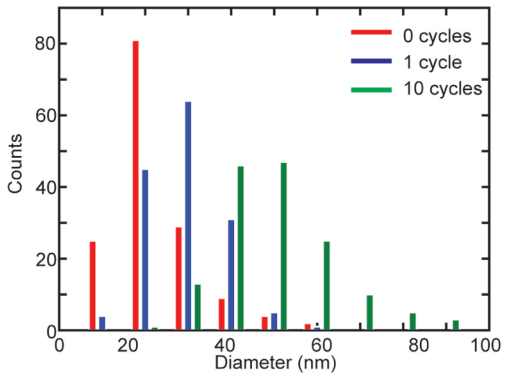

Figure 3.5. Diameter distribution of Cu_2O SILAR deposition on TiO_2 nanoparticles.

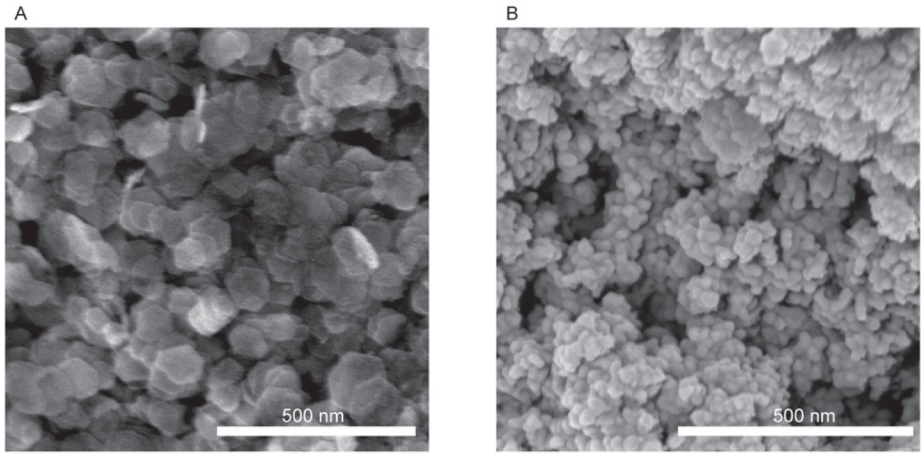

Figure 3.6. SEM images of Cu_2O thin films deposited on NiO nanoplatelets and TiO_2 nanoparticles. (A) 10 cycles of Cu_2O SILAR deposition on NiO and (B) TiO_2 nanoparticulate films. The TiO_2/Cu_2O film has 5 nm of Au deposited on top to improve contrast.

Using SEM images of the deposition of several different numbers of cycles on spherical nanoparticles, we found that the material deposits 1.5 nm per cycle. The distribution of diameters before and after one and ten cycles of the deposition can be seen in Figure 3.5. The diameter

distribution was measured on TiO_2 nanoparticles because of their spherical geometry and to demonstrate the generalizability of the Cu_2O deposition on any nanoparticulate thin film. Because SILAR is a solution based deposition technique, any part of the mesoscopic metal oxide film that is wetted by the solution will encounter deposition. In contrast, several commonly used deposition techniques for planar thin films can be used to deposit Cu_2O in a directional fashion, which would fail to completely encapsulate the nanoparticulate scaffold. Techniques such as pulsed laser deposition, metal evaporation, and sputter have all been demonstrated effective for Cu_2O deposition, but because of their directional nature have been not been pursued in this specific architecture.[47–49] Figure 3.6 demonstrates that the mesoporous nature of the metal oxide electrodes are maintained post Cu_2O deposition as shown via SEM imaging.

To confirm that the Cu_2O deposition penetrates through the entire thickness of the mesoporous metal oxide film, electron microprobe analysis (EMPA) was used. Figure 3.7 indicates that the Cu_2O deposits throughout the thickness of a TiO_2 mesoporous film using a linescan through the film. The linescan data was collected using an electron microprobe analyzer (EMPA). The EMPA linescan results indicate that although there is Cu_2O deposition throughout the TiO_2

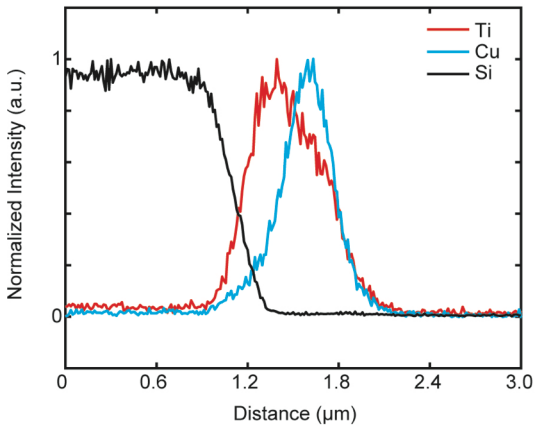

Figure 3.7. EMPA normalized line scans of TiO_2/Cu_2O films on a glass substrate. The Si signal is present from the substrate.

film, there is a slight preference for Cu_2O to deposit closer to the surface as indicated by the slight offset in the normalized peaks of Cu and Ti. The film was prepared on a glass slide and the Si signal is present from the substrate.

When first deposited, the amorphous Cu_2O led to *J-V* performance inferior to bare NiO. The decrease in performance, notably the average V_{oc} decreasing from ~100 mV to ~30 mV. The Cu_2O deposited had a high water content as a result of the aqueous deposition technique. To improve electrical contact and dry the shell material, an annealing process was implemented. Because Cu_2O can oxidize when annealed in an oxygen containing environment, the NiO/Cu_2O

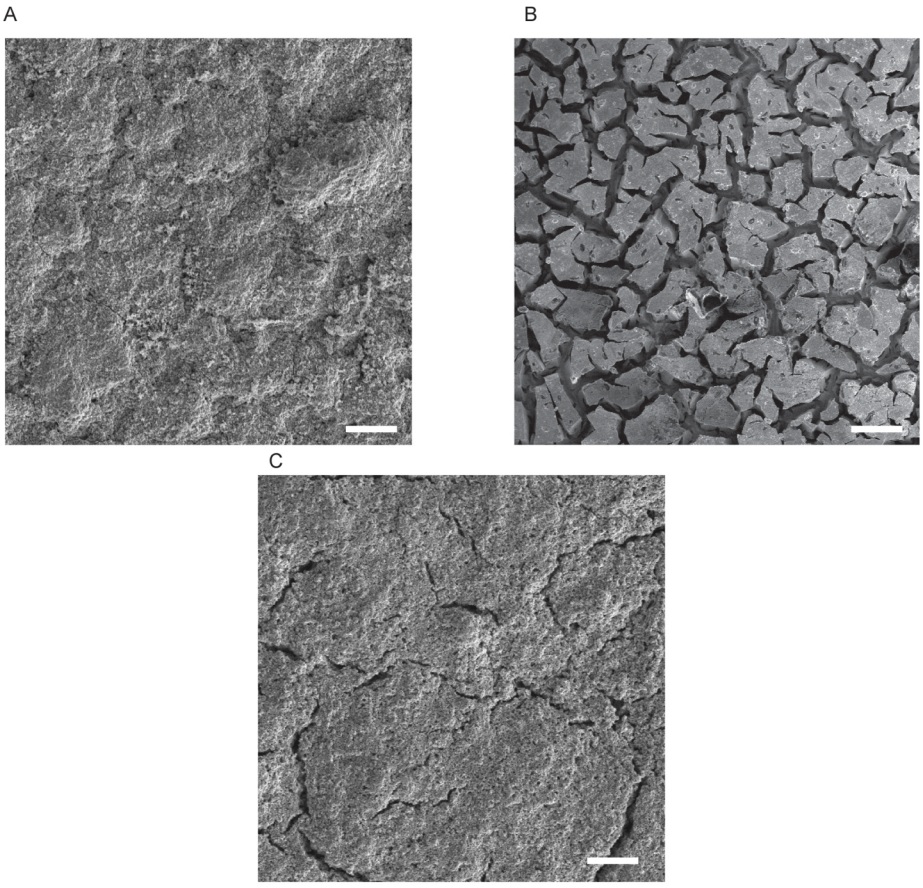

Figure 3.8. SEM images of TiO_2/Cu_2O films with 50 cycles of SILAR deposition. (A) TiO_2/Cu_2O film with 50 cycles of SILAR deposition with no post-anneal. (B) TiO_2/Cu_2O film with 50 cycles of SILAR deposition with a fast ramp 450 °C anneal (40 °C/min). (C) TiO_2/Cu_2O film with 50 cycles of SILAR deposition with a slow ramp to 450 °C post-anneal (1 °C/min). Scale bars represent 10 μm.

films were annealed post Cu_2O deposition in a nitrogen atmosphere. The high concentration of water remaining in the material caused desiccation cracks as large as several microns wide throughout the film, severely limiting the electrical properties of the material. To prevent the desiccation cracks and preserve the geometry of the mesoporous core scaffold, a ramp rate of 1 °C/min was introduced to the anneal process to slowly extract the excess water without disturbing the film overall. Figure 3.8 shows the results of desiccation cracks caused the fast versus slow ramping anneal processes.

Several iterations of testing indicated that the most effective Cu_2O shell for NiO was the thinnest possible at 1.5 nm from one cycle of SILAR with a post-deposition anneal at 450 °C. The overall performance of the DSSC was recovered with PCE values ranging from $2.5 \times 10^{-4} \pm 6.3 \times 10^{-5}$ % to $5.3 \times 10^{-2} \pm 1.5 \times 10^{-3}$ % for the SILAR Cu_2O shell. However, the shell at best provided only minimal improvements and often presented additional obstacles. Full *J-V* statistics are included in Table 3.1. Notably, the solution phase SILAR deposition was limited to the lower bound of 1.5 nm of Cu_2O from one cycle. To introduce a thinner shell that was also conformal, we turned to atomic layer deposition (ALD) as an alternative technique.

ALD deposits materials in atomically thin layers via surface limiting reactions and has been reported for several metal oxides including copper oxide. The use of $Cu(dmap)_2$ as the copper containing precursor resulted in deposition of Cu^{2+} cations and subsequently reacted to form CuO. Because the vapor pressure of $Cu(dmap)_2$ is significantly lower than several other ALD metal salt precursors such as trimethylaluminum, the deposition rate of CuO is significantly lower than other metal oxides at sub-monolayer thicknesses per cycle. Previous reports indicate thicknesses of 0.3 Å per cycle using $Cu(dmap)_2$, and ellipsometry measurements confirmed this result.[41] The average bond length between copper and oxygen atoms in solid CuO is on the order of 0.193 ± 0.002 nm.[50]

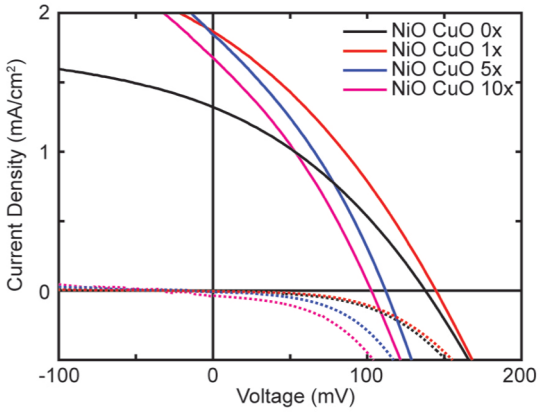

Figure 3.9. DSSC *J-V* curves for NiO/CuO electrodes with no post-deposition anneal featuring untreated NiO in black and 1, 5, and 10 cycles in red, blue, and pink respectively.

Consequently we can deduce that one cycle of deposition produces incomplete coverage. Interestingly, the highest J_{sc} values result from only one cycle of CuO deposition. Sub-monolayer deposition of other materials have previously been reported to passivate surface defects on NiO.[13] Possibly, the Cu^{2+} cations are performing a similar role to the Al^{3+} or B^{3+} ions reported previously, although with a lower efficiency. The ionic radii of Cu^{2+} and Ni^{2+} are 0.6 and 0.55 Å, and substituting a singular Cu^{2+} cation in the rock salt lattice would be feasible. As we approach a full monolayer of coverage with 10 cycles of ALD CuO, the DSSC performance starts to drop off possibly due to poor electronic contact between the CuO shell and the NiO core or ALD precursor residues. Consequently, a post-deposition thermal anneal treatment was performed on the NiO/CuO films. However, the *J-V* performance for the devices that received the post-deposition anneal either decreased or was maintained. Champion *J-V* curves are shown in Figure 3.9. Post-deposition annealed device metrics are included in Table 3.2. Although we successfully created the targeted device architecture, which was intended to decrease recombination and increase device efficiency, DSSC performances were essentially unchanged after the addition of an ultrathin film of CuO or Cu_2O.

Table 3.1. *J-V* Characteristics of Cu_xO shells on NiO mesoporous photocathodes in p-DSSCs

	J_{SC} (mA/cm^2)	V_{OC} (mV)	Fill Factor (%)	PCE x 10^{-2} (%)
NiO CuO 0x	1.29 ± 0.07	117 ±11	29 ± 1	4.4 ± 0.7
NiO CuO 1x	1.34 ± 0.05	127 ±11	32.1 ± 0.5	5.6 ± 0.2
NiO CuO 5x	1.58 ± 0.03	113 ± 4	31.6 ± 0.4	5.7 ± 1.0
NiO CuO 10x	1.52 ± 0.02	102 ± 3	30.4 ± 0.5	4.7 ± 0.5
NiO Cu_2O 1x	1.24 ± 0.06	122 ± 9	31.5 ± 0.2	5.0 ± 0.2
NiO Cu_2O 3x	1.44 ± 0.04	111 ± 6	33.2 ± 0.2	5.3 ± 0.1

Table 3.2 *J-V* Characteristics of CuO shells on NiO mesoporous photocathodes with a post-deposition thermal treatment.

	J_{SC} (mA/cm^2)	V_{OC} (mV)	Fill Factor (%)	PCE x 10^{-2} (%)
NiO CuO 0x	1.29 ± 0.07	117 ±11	29 ± 1	4.4 ± 0.7
NiO CuO 1x	0.93 ± 0.04	118 ±10.	28 ± 2	3.1 ± 0.2
NiO CuO 5x	1.56 ± 0.05	115 ± 2	28 ± 1	5.0 ± 0.2
NiO CuO 10x	1.30 ± 0.03	102 ± 12	30. ± 1	4.1 ± 0.1

3.4 Conclusions

Both Cu_2O and CuO materials were successfully deposited on mesoporous NiO electrodes to create a core/shell architecture. Using two different deposition techniques and various post-deposition treatments, p-DSSCs were assembled and tested with mixed results. In general, the device performance only marginally improved and, in some instances, performance deteriorated. Poor electrical contact between core and shell materials likely contributed to lackluster performance. Additionally, several of the issues that contribute to NiO's poor performance are present for other p-type metal oxides including Cu_2O and CuO. Therefore, putting a shell of Cu_xO on NiO via either SILAR or ALD has not and will not provide the desired increase in performance to match TiO_2. Consequently, the search for a superior photocathode material continues.

3.5 Acknowledgements

This work was primarily funded by the UNC Energy Frontier Research Center, and EFRC funded by the U.S. Department of Energy, Office of Science, Office of Basic Energy Sciences, under award DE-SC0001011. Thank you to Jake Evans for assisting with running experiments related to the ALD CuO work.

REFERENCES

(1) Kakiage, K.; Aoyama, Y.; Yano, T.; Oya, K.; Fujisawa, J.; Hanaya, M. Highly-Efficient Dye-Sensitized Solar Cells with Collaborative Sensitization by Silyl-Anchor and Carboxy-Anchor Dyes. *Chem. Commun.* **2015**, *51* (88), 15894–15897.

(2) Perera, I. R.; Daeneke, T.; Makuta, S.; Yu, Z.; Tachibana, Y.; Mishra, A.; Bäuerle, P.; Ohlin, C. A.; Bach, U.; Spiccia, L. Application of the Tris(acetylacetonato)iron(III)/(II) Redox Couple in P-Type Dye-Sensitized Solar Cells. *Angew. Chemie Int. Ed.* **2015**, *54*, 3758–3761.

(3) Daeneke, T.; Yu, Z.; Lee, G. P.; Fu, D.; Duffy, N. W.; Makuta, S.; Tachibana, Y.; Spiccia, L.; Mishra, A.; Bäuerle, P.; et al. Dominating Energy Losses in NiO P-Type Dye-Sensitized Solar Cells. *Adv. Energy Mater.* **2015**, *5* (4), 1401387.

(4) Powar, S.; Daeneke, T.; Ma, M. T.; Fu, D.; Duffy, N. W.; Götz, G.; Weidelener, M.; Mishra, A.; Bäuerle, P.; Spiccia, L.; et al. Highly Efficient P-Type Dye-Sensitized Solar Cells Based on tris(1,2-diaminoethane)cobalt(II)/(III) Electrolytes. *Angew. Chemie - Int. Ed.* **2013**, *52* (2), 602–605.

(5) Qin, P.; Linder, M.; Brinck, T.; Boschloo, G.; Hagfeldt, A.; Sun, L. High Incident Photon-to-Current Conversion Efficiency of P-Type Dye-Sensitized Solar Cells Based on NiO and Organic Chromophores. *Adv. Mater.* **2009**, *21* (29), 2993–2996.

(6) Sharma, R. K.; Ghose, R. Synthesis of Porous Nanocrystalline NiO with Hexagonal Sheet-like Morphology by Homogeneous Precipitation Method. *Superlattices Microstruct.* **2015**, *80*, 169–180.

(7) Kerli, S.; Alver, U.; Yaykaşlı, H. Investigation of the Properties of In Doped NiO Films. *Appl. Surf. Sci.* **2014**, 2–5.

(8) Wei, L.; Jiang, L.; Yuan, S.; Ren, X.; Zhao, Y.; Wang, Z.; Zhang, M.; Shi, L.; Li, D. Valence Band Edge Shifts and Charge-Transfer Dynamics in Li-Doped NiO Based P-Type DSSCs. *Electrochim. Acta* **2016**, *188*, 309–316.

(9) Ho, P.; Bao, L. Q.; Ahn, K.-S.; Cheruku, R.; Kim, J. H. P-Type Dye-Sensitized Solar Cells: Enhanced Performance with a NiO Compact Blocking Layer. *Synth. Met.* **2016**, *217*, 314–321.

(10) Dini, D.; Halpin, Y.; Vos, J. G.; Gibson, E. a. The Influence of the Preparation Method of NiOx Photocathodes on the Efficiency of P-Type Dye-Sensitized Solar Cells. *Coord. Chem. Rev.* **2015**, *304–305*, 179–201.

(11) D'Amario, L.; Antila, L. J.; Pettersson Rimgard, B.; Boschloo, G.; Hammarström, L. Kinetic Evidence of Two Pathways for Charge Recombination in NiO-Based Dye-Sensitized Solar Cells. *J. Phys. Chem. Lett.* **2015**, *6* (5), 779–783.

(12) Brisse, R.; Faddoul, R.; Bourgeteau, T.; Tondelier, D.; Leroy, J.; Campidelli, S.; Berthelot, T.; Geffroy, B.; Jousselme, B. Ink-Jet Printing NiO-Based P-Type Dye Sensitized Solar Cells. *ACS Appl. Mater. Interfaces* **2017**, *9* (3), 2369–2377.

(13) Flynn, C. J.; McCullough, S. M.; Oh, E.; Li, L.; Mercado, C. C.; Farnum, B. H.; Li, W.; Donley, C. L.; You, W.; Nozik, A. J.; et al. Site-Selective Passivation of Defects in NiO Solar Photocathodes by Targeted Atomic Deposition. *ACS Appl. Mater. Interfaces* **2016**, *8*, 4754–4761.

(14) Nattestad, A.; Ferguson, M.; Kerr, R.; Cheng, Y.-B.; Bach, U. Dye-Sensitized Nickel(II) Oxide Photocathodes for Tandem Solar Cell Applications. *Nanotechnology* **2008**, *19* (29), 295304.

(15) Li, M.-H.; Yum, J.-H.; Moon, S.-J.; Chen, P. Inorganic P-Type Semiconductors: Their Applications and Progress in Dye-Sensitized Solar Cells and Perovskite Solar Cells. *Energies* **2016**, *9* (5), 331.

(16) D'Amario, L.; Boschloo, G.; Hagfeldt, A.; Hammarström, L. Tuning of Conductivity and Density of States of NiO Mesoporous Films Used in P-Type DSSCs. *J. Phys. Chem. C* **2014**, *118* (34), 19556–19564.

(17) Farré, Y.; Zhang, L.; Pellegrin, Y.; Planchat, A.; Blart, E.; Boujtita, M.; Hammarström, L.; Jacquemin, D.; Odobel, F. Second Generation of Diketopyrrolopyrrole Dyes for NiO-Based Dye-Sensitized Solar Cells. *J. Phys. Chem. C* **2016**, *120* (15), 7923–7940.

(18) Liu, Q.; Wei, L.; Yuan, S.; Ren, X.; Zhao, Y.; Wang, Z.; Zhang, M.; Shi, L.; Li, D.; Li, A. Influence of Interface Properties on Charge Density, Band Edge Shifts and Kinetics of the Photoelectrochemical Process in P-Type NiO Photocathodes. *RSC Adv.* **2015**, *5* (88), 71778–71784.

(19) Daeneke, T.; Yu, Z.; Lee, G. P.; Fu, D.; Duffy, N. W.; Makuta, S.; Tachibana, Y.; Spiccia, L.; Mishra, A.; Bauerle, P.; et al. Dominating Energy Losses in NiO P-Type Dye-Sensitized Solar Cells. *Adv. Energy Mater.* **2015**, *5* (4).

(20) Natu, G.; Huang, Z.; Ji, Z.; Wu, Y. The Effect of an Atomically Deposited Layer of Alumina on NiO in P-Type Dye-Sensitized Solar Cells. *Langmuir* **2012**, *28* (1), 950–956.

(21) Knauf, R. R.; Kalanyan, B.; Parsons, G. N.; Dempsey, J. L. Charge Recombination Dynamics in Sensitized SnO_2/TiO_2 Core/Shell Photoanodes. *J. Phys. Chem. C* **2015**, *119* (51), 28353–28360.

(22) Gish, M. K.; Lapides, A. M.; Brennaman, M. K.; Templeton, J. L.; Meyer, T. J.; Papanikolas, J. M. Ultrafast Recombination Dynamics in Dye-Sensitized SnO_2 /TiO_2 Core/Shell Films. *J. Phys. Chem. Lett.* **2016**, 5297–5301.

(23) Sherman, B. D.; Ashford, D. L.; Lapides, A. M.; Sheridan, M. V.; Wee, K. R.; Meyer, T. J. Light-Driven Water Splitting with a Molecular Electroassembly-Based Core/Shell Photoanode. *J. Phys. Chem. Lett.* **2015**, *6* (16), 3213–3217.

(24) Wee, K.-R.; Sherman, B. D.; Brennaman, M. K.; Sheridan, M. V.; Nayak, A.; Alibabaei, L.; Meyer, T. J. An Aqueous, Organic Dye Derivatized SnO_2/TiO_2 Core/shell Photoanode. *J. Mater. Chem. A* **2016**, *4* (8), 2969–2975.

(25) Nayak, A.; Roy, S.; Sherman, B. D.; Alibabaei, L.; Lapides, A. M.; Brennaman, M. K.; Wee, K. R.; Meyer, T. J. Phosphonate-Derivatized Porphyrins for Photoelectrochemical Applications. *ACS Appl. Mater. Interfaces* **2016**, *8* (6), 3853–3860.

(26) Tarini, M.; Prakash, N.; Sahib, I. K. M. M.; Hayakawa, Y. Novel Sugar Apple-Shaped SnO_2 Microspheres With Light Scattering Effect in Dye-Sensitized Solar Cell Application. *IEEE J. Photovoltaics* **2017**, *7* (4), 1050–1057.

(27) Flynn, C. J.; McCullough, S. M.; Li, L.; Donley, C. L.; Kanai, Y.; Cahoon, J. F. Passivation of Nickel Vacancy Defects in Nickel Oxide Solar Cells by Targeted Atomic Deposition of Boron. *J. Phys. Chem. C* **2016**, *120* (30), 16568–16576.

(28) Flynn, C. J.; Oh, E. E.; McCullough, S. M.; Call, R. W.; Donley, C. L.; Lopez, R.; Cahoon, J. F. Hierarchically-Structured NiO Nanoplatelets as Mesoscale P-Type Photocathodes for Dye-Sensitized Solar Cells. *J. Phys. Chem. C* **2014**, *118* (26), 14177–14184.

(29) Pathan, H. M.; Lokhande, C. D. Deposition of Metal Chalcogenide Thin Films by Successive Ionic Layer Adsorption and Reaction (SILAR) Method. *Bull. Mater. Sci.* **2004**, *27* (2), 85–111.

(30) Jambure, S. B.; Patil, S. J.; Deshpande, A. R.; Lokhande, C. D. A Comparative Study of Physico-Chemical Properties of CBD and SILAR Grown ZnO Thin Films. *Mater. Res. Bull.* **2014**, *49*, 420–425.

(31) Abdel Rafea, M.; Roushdy, N. Determination of the Optical Band Gap for Amorphous and Nanocrystalline Copper Oxide Thin Films Prepared by SILAR Technique. *J. Phys. D. Appl. Phys.* **2009**, *42* (1), 15413.

(32) Chatterjee, S.; Saha, S. K.; Pal, A. J. Formation of All-Oxide Solar Cells in Atmospheric Condition Based on Cu_2O Thin-Films Grown through SILAR Technique. *Sol. Energy Mater. Sol. Cells* **2016**, *147*, 17–26.

(33) Mageshwari, K.; Sathyamoorthy, R. Physical Properties of Nanocrystalline CuO Thin Films Prepared by the SILAR Method. *Mater. Sci. Semicond. Process.* **2013**, *16* (2), 337–343.

(34) Mukherjee, B.; Peterson, A.; Subramanian, V. R. 1D CdS/PbS Heterostructured Nanowire Synthesis Using Cation Exchange. *Chem. Commun. (Camb).* **2012**, *48* (18), 2415–2417.

(35) Sadtler, B.; Demchenko, D. O.; Zheng, H.; Hughes, S. M.; Merkle, M. G.; Dahmen, U.; Wang, L.-W.; Alivisatos, a P. Selective Facet Reactivity during Cation Exchange in Cadmium Sulfide Nanorods. *J. Am. Chem. Soc.* **2009**, *131* (14), 5285–5293.

(36) Zheng, H.; Sadtler, B.; Habenicht, C.; Freitag, B.; Alivisatos, A. P.; Kisielowski, C. Controlling Electron Beam-Induced Structure Modifications and Cation Exchange in Cadmium Sulfide-Copper Sulfide Heterostructured Nanorods. *Ultramicroscopy* **2013**, *134*, 207–213.

(37) Kelly, D.; Singh, A.; Barrett, C. A.; O'Sullivan, C.; Coughlan, C.; Laffir, F. R.; O'Dwyer, C.; Ryan, K. M. A Facile Spin-Cast Route for Cation Exchange of Multilayer Perpendicularly-Aligned Nanorod Assemblies. *Nanoscale* **2011**, *3* (11), 4580–4583.

(38) Ning, J.; Xiao, G.; Wang, L.; Zou, B.; Liu, B.; Zou, G. Facile Synthesis of Magnetic Metal (Mn, Fe, Co, and Ni) Oxides Nanocrystals via a Cation-Exchange Reaction. *Nanoscale* **2011**, *3* (2), 741–745.

(39) Li, Z.; Barry, S. T.; Gordon, R. G. Synthesis and Characterization of copper(I) Amidinates as Precursors for Atomic Layer Deposition (ALD) of Copper Metal. *Inorg. Chem.* **2005**, *44* (6), 1728–1735.

(40) Waechtler, T.; Oswald, S.; Roth, N.; Jakob, A.; Lang, H.; Ecke, R.; Schulz, S. E.; Gessner, T.; Moskvinova, A.; Schulze, S.; et al. Copper Oxide Films Grown by Atomic Layer Deposition from Bis(tri-N-butylphosphane)copper(I)acetylacetonate on Ta, TaN, Ru, and SiO[sub 2]. *J. Electrochem. Soc.* **2009**, *156* (6), H453.

(41) Iivonen, T.; Hämäläinen, J.; Marchand, B.; Mizohata, K.; Mattinen, M.; Popov, G.; Kim, J.; Fischer, R. A.; Leskelä, M. Low-Temperature Atomic Layer Deposition of copper(II) Oxide Thin Films. *J. Vac. Sci. Technol. A Vacuum, Surfaces, Film.* **2016**, *34* (1), 01A109.

(42) Gordon, P. G.; Kurek, A.; Barry, S. T. Trends in Copper Precursor Development for CVD and ALD Applications. *ECS J. Solid State Sci. Technol.* **2015**, *4* (1), N3188–N3197.

(43) Kim, H.; Lee, M. Y.; Kim, S. H.; Bae, S. I.; Ko, K. Y.; Kim, H.; Kwon, K. W.; Hwang, J. H.; Lee, D. J. Highly-Conformal P-Type copper(I) Oxide (Cu_2O Thin Films by Atomic Layer Deposition Using Fluorine-Free Amino-Alkoxide Precursor. *Appl. Surf. Sci.* **2015**, *349*, 673–682.

(44) Dhakal, D.; Waechtler, T.; Schulz, S. E.; Gessner, T.; Lang, H.; Mothes, R.; Tuchscherer, A. Surface Chemistry of a Cu(I) Beta-Diketonate Precursor and the Atomic Layer Deposition of Cu_2O on SiO_2 Studied by X-Ray Photoelectron Spectroscopy. *J. Vac. Sci. Technol. A Vacuum, Surfaces, Film.* **2014**, *32* (4), 41505.

(45) Melzer, M.; Waechtler, T.; Müller, S.; Fiedler, H.; Hermann, S.; Rodriguez, R. D.; Villabona, A.; Sendzik, A.; Mothes, R.; Schulz, S. E.; et al. Copper Oxide Atomic Layer Deposition on Thermally Pretreated Multi-Walled Carbon Nanotubes for Interconnect Applications. *Microelectron. Eng.* **2013**, *107*, 223–228.

(46) Koffyberg, F. P.; Benko, F. A. A Photoelectrochemical Determination of the Position of the Conduction and Valence Band Edges of P-Type CuO. *J. Appl. Phys.* **1982**, *53* (2), 1173–1177.

(47) Akimoto, K.; Ishizuka, S.; Yanagita, M.; Nawa, Y.; Paul, G. K.; Sakurai, T. Thin Film Deposition of Cu_2O and Application for Solar Cells. *Sol. Energy* **2006**, *80* (6), 715–722.

(48) Espinós, J. P.; Morales, J.; Barranco, A.; Caballero, A.; Holgado, J. P.; González-Elipe, A. R.; Gonza, A. R. Interface Effects for Cu, CuO, and Cu_2O Deposited on SiO_2 and ZrO_2. XPS Determination of the Valence State of Copper in Cu/SiO_2 and Cu/ZrO_2 Catalysts. *J. Phys. Chem. B* **2002**, *106* (27), 6921–6929.

(49) Ishizuka, S.; Suzuki, K.; Okamoto, Y.; Yanagita, M.; Sakurai, T.; Akimoto, K.; Fujiwara, N.; Kobayashi, H.; Matsubara, K.; Niki, S. Polycrystallinen-ZnO/p-Cu_2O Heterojunctions Grown by RF-Magnetron Sputtering. *Phys. Status Solidi* **2004**, *1*, 1067–1070.

(50) Ahmed, A.; Elvati, P.; Violi, A. Size-and Phase-Dependent Structure of copper(II) Oxide Nanoparticles. *RSC Adv.* **2015**, *5* (44), 35033–35041.

Chapter 4: Cation Effects in p-Type Dye-Sensitized Solar Cells

4.1 Introduction

In the past 25 years, significant efforts have been made towards bettering conventional TiO_2 Grätzel cells with over 25,000 citations of the seminal 1991 paper.[1] As with all solar devices, improved power conversion efficiency has been a perennial target, and incremental improvements have been consistently reported. Moving forward in device design complexity, two photoactive electrodes, one cathode and one anode, will be required for tandem cells, which provide the only avenues for target reactions including water splitting and CO_2 reduction. Despite their necessity for successful tandem cells, fundamentally instrumental components of photocathodes still continue to require significant study, and improvement.

A standard DSSC contains three primary components: the semiconductor, the chromophore, and the electrolyte. For n-DSSCs, dedicated studies have been reported for each component.[2–7] However, for p-DSSCs only the semiconductor and the chromophore have received systematic improvements.[8–12] The appropriate electronic and optical properties in a solar cell are critical for its successful functioning. Most importantly, the energetics of each component of the cell must align so that circuit can operate efficiently. Through systematic study of individual components of the standard NiO p-DSSC, we believe significant improvements can result from intentional electrolyte design adjustments. The work presented here begins to address the previously unreported impact of the cation in electrolyte solution.

Thus far, performance improvements on the p-type side have dawdled since the first NiO device report in 1999.[13] Recently, a thorough investigation of various preparations of NiO has been reported.[11] Although there have been reports on replacing I^-/I_3^- the electrolyte redox couple[14,15] the interaction between the electrolyte components, dye, and metal oxide surface has received little explicit attention despite being a significant—perhaps the most significant—component of the device. On the n-type side, a conventional Grätzel cell, several tactics have been used to precisely probe what is causing the cell to perform well, and, conversely, perform poorly. Notably, the first dedicated study on cation effects in TiO_2 devices was published just over a year after the seminal paper in 1991.[1,16] Largely because of the explicit consideration of the interface between the semiconductor and the electrolyte, TiO_2 devices have achieved a record efficiency of 14.3%.[17] On the p-type side, a reverse Grätzel cell, performance has lagged behind. With a record performance of only 2.5% efficiency thus far[15], significant strides still need to be made on the photocathode half-cell for the envisioned tandem cell to function efficiently.[18,19] Here, we present a facile approach to tuning available states near the valence band edge by selectively choosing the cation in the electrolyte. Furthermore, probing fundamental physical and chemical properties of the interface between the metal oxide semiconductor and the electrolyte is relevant for any DSSC system and results on NiO can be generalized to any p-type semiconductor electrode used in a DSSC.

Although spectators with respect to the redox chemistry, the cations influence device performance by self-assembling on the electrode's surface introducing a slew of effects. Cation effects have been studied on TiO_2 n-DSSCs concurrently with broader n-DSSC's studies and are known to impact significant parameters for device performance.[2,16,20–22] Notable parameters affected include the flat band potential and the density of states near the band edge.

Conveniently the I^-/I_3^- Nernstian potential of 0.2 vs Ag/AgCl lands at a favorable potential for both TiO_2 and NiO DSSCs. However, the circuit for p-DSSCs operates in reverse in comparison to n-DSSCs, and the cations impact performance in reverse trends as well. Equipped with the understanding that all components in the electrolyte, including 'spectator' cations, we can begin to intentionally design an advantageous electrolyte to favor p-DSSCs' energetics. Through analytical techniques including electrochemical impedance spectroscopy (EIS), cyclic voltammetry (CV), Mott-Schottky analysis, and current-voltage (*J-V*) sweeps, we begin to elucidate the impact of cations on the overall performance of NiO p-DSSCs.

When introduced to the electrolyte, cations can adsorb to the metal oxide's surface, introducing a dipole on the surface which disturbs the charge balance pushing states deeper electronically. The extent of the shift depends on the strength of the dipole, and the change in the flat band potential is measured experimentally using a three electrode cell and Mott-Schottky analysis. The trends observed for flat band positions as shown in Figure 1 are consistent with other reports on cation effects on TiO_2.[2,20,21] Typically Li^+ is used because for n-DSSCs it gives the largest V_{OC} because the V_{FB} is shifted farthest negative, resulting in the largest difference from the from the Nernst potential. Because the valence band is relevant for p-DSSCs instead of the conduction band for n-DSSCs, shifting the V_{FB} more negative by introducing Li^+ actually decreases maximum theoretical V_{oc} for p-DSSCs. Based on the cations tested in this study, the evidence suggests that the commonly used Li^+ allows for the smallest possible V_{OC} for NiO and a significant increase in performance can be achieved by simply changing the cation.

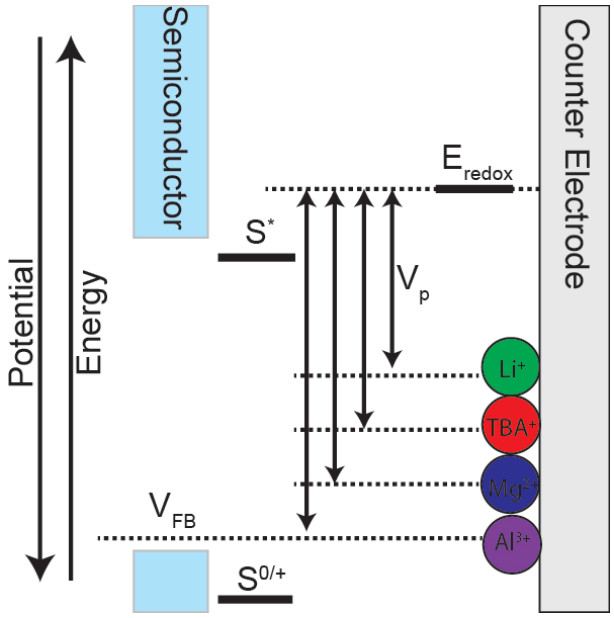

Figure 4.1. Flat band positions under the influence of different cations present at the interface of the p-type semiconductor and the electrolyte within a DSSC energetic scheme.

4.2 Experimental Materials and Methods

4.2.a Materials and Reagents.

Acetonitrile (99.6%), iodine (>99.99%), lithium iodide (99.9%), lithium perchlorate (>95.0%), magnesium iodide (98%), magnesium perchlorate (ACS reagent grade), tetrabutylammonium iodide (98%), aluminum perchlorate nonahydrate (98%), α-terpineol (anhydrous), and ethyl cellulose (300 cP viscosity) were all purchased from Sigma-Aldrich. Absolute ethanol was purchased from Fisher Scientific. NiO nanoparticles (product #28N-0801) were purchased from Inframat Advanced Materials. 1,3-dimethylimidazolium iodide and 25 μm thick Surlyn polymer was purchased from Solaronix. P1 chromophore was purchased from Dynamo. All chemicals were used as received. Fluorine-doped tin oxide (FTO) glass (TEC 15 $\Omega \cdot cm^2$) was purchased from Hartford glass and cleaned with typical organic solvents and sonication.

4.2.b Spin coating paste preparation

NiO spin coating paste was prepared using a literature method with Inframat NiO nanoparticles and standard homogenization techniques. [23]

4.2.c Analytical methods.

Mott-Schottky analysis was performed via AC impedance spectroscopy in a three-electrode cell with 0.1 M perchlorate acetonitrile electrolyte. The working electrode was the NiO mesoscopic film on FTO, the counter electrode was Pt mesh, and the reference electrode was Ag/AgCl. Cyclic voltammetry measurements were performed in the same three-electrode cells. Both Mott-Schottky and cyclic voltammetry measurements were performed on a CH Instruments model 604E potentiostat. EIS measurements were performed on a Gamry Reference 600 electrochemical impedance spectrometer in a two electrode configuration where the counter and the reference electrode were both the Pt electrode. *J-V* measurements were performed using a Newport Oriel 150W Class ABB solar simulator calibrated with a certified reference Newport 91150 V solar cell, and a Keithley 2636A SourceMeter was used for all electrical measurements. Optical absorbance measurements were obtained with a Cary 5000 UV-Vis-NIR spectrometer.

4.2.d DSSC assembly and characterization.

DSSC assembly was performed identically to previous reports except changing the electrolyte cation as appropriate.[24]

4.3: Results and Discussion

In addition to directly affecting the maximum V_{oc} of the cell, cations in the electrolyte also affects the driving force for the reduction of the excited dye molecule on the electrode surface. Because the chromophore's potential is fixed, there is a lower bound for the V_{FB} while still allowing for photoinjection from the chromophore. Between the least positive V_{FB} corresponding to Li^+ (0.13 V vs. Ag/AgCl) and most positive V_{FB} corresponding to Al^{3+} (0.93 V vs. Ag/AgCl), we observe a difference of 800 mV as shown in Figure 4.2.

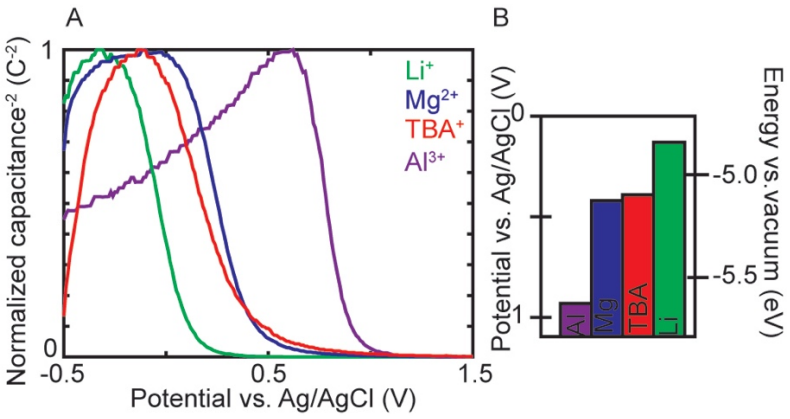

Figure 4.2. Flat band measurements on NiO. (A) Mott-Schottky plots of NiO in different electrolyte solutions with various cations. (B) Extracted V_{FB} values from the Mott-Schottky plots.

In principle, pushing the V_{FB} to more electrochemically positive potentials should correspond to an increase in the Voc in DSSCs and a decrease in driving force for the excited state chromophore to inject. We do observe an increase in V_{OC} moving from Li^+ to Mg^{2+} with average values of 109 ± 5 mV and 172 ± 3 mV respectively. *J-V* metrics are listed in Table 4.1. Incident photon to current efficiency (IPCE) measurements indicate that, despite the decrease in driving force, the chromophore injects similarly for both Li^+ and Mg^{2+} as shown in Figure 4.3.

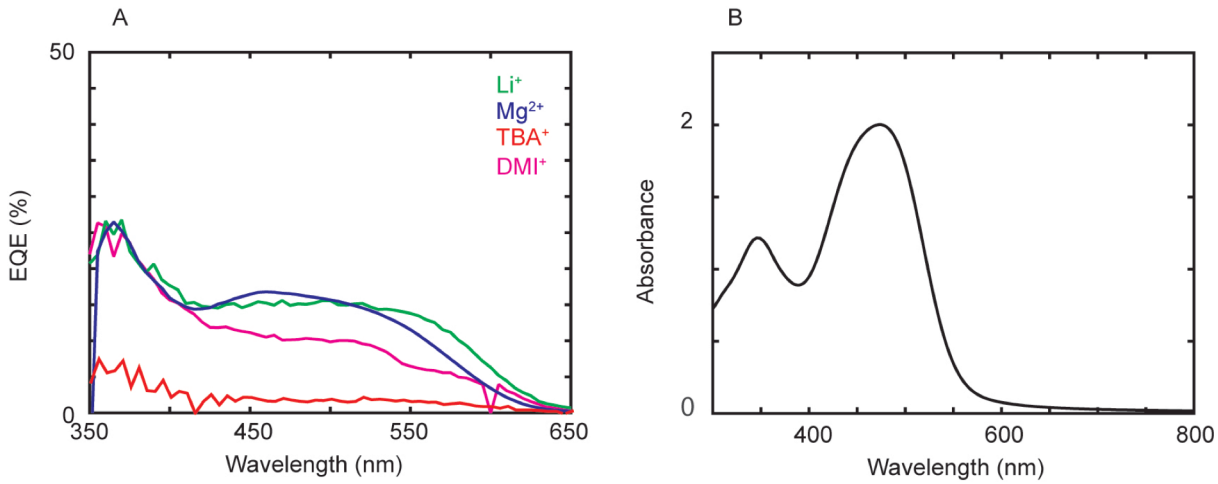

Figure 4.3. (A): IPCE of NiO DSSCs with various cations present in the electrolyte. Panel (B): UV-Vis absorbance for P1 in acetonitrile.

The cyclic voltammetry (CV) measures electronically active density of states (DOS) directly in solution by DOS=$C/(p \bullet L \bullet e)$ where C is capacitance (current density/scan rate of the CV), p is porosity, L is film thickness, and e is fundamental charge. The CV traces and extracted DOS plots are shown in Figure 4.4.

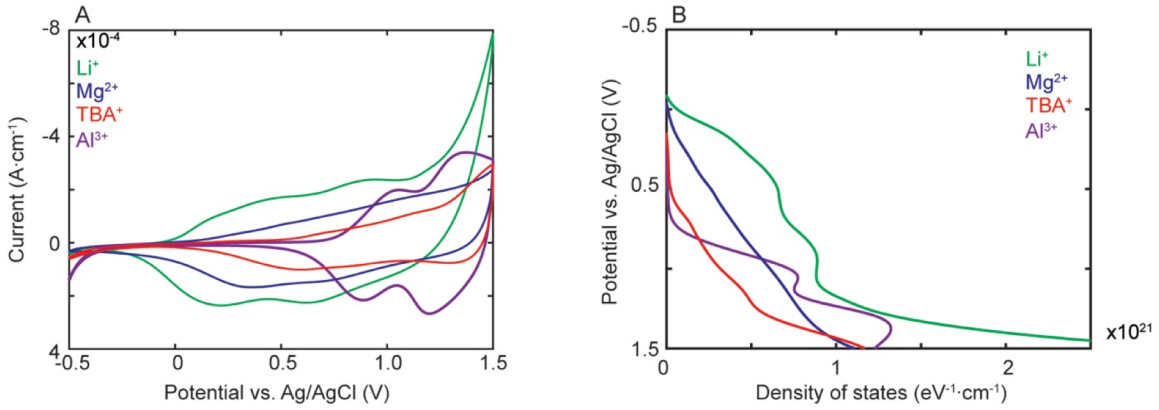

Figure 4.4. Electrochemical measurements on NiO. (A) Cyclic voltammograms of NiO in 0.1 M $XClO_4$ where X is Li^+, Mg^{2+}, TBA^+, Al^{3+}. (B) Calculated density of states maps for NiO

Previous work with NiO indicates that modifying the lattice with atomic additions in the vapor phase can electronically passivate defects throughout the material which decreases recombination at the electrode's surface.[25,26] The metal vacancies that give rise to the p-type dopant in NiO also result in dangling oxygen bonds. The unsaturated dangling oxygen bond cause a rise in interband trap state density which causes the black color of NiO. We attribute the decrease in DOS between 0-0.5 V vs. Ag/AgCl in solution to a similar type of mechanism observed in the gas phase. The data presented in Figure 4.3 suggests that available DOS near NiO VBE can be significantly tuned using different cations. Note that DMI^+ analysis is omitted because the appropriate salt is not commercially available.

Electrochemical impedance spectroscopy (EIS) was used to determine the impact of different cations on charge transfer efficiencies and other kinetic parameters. EIS has become an increasingly powerful technique for characterizing DSSCs, and several significant parameters have been quantified using this technique including charge transfer resistances and recombination resistances.[27,28] We focus on comparing the best cation, Mg^{2+} to the standard Li^+ to further elucidate the difference in *J-V* performance between the two. Using a double-Randle's circuit to model the system, we observe that moving from Li^+ to Mg^{2+}, the cell becomes overall less resistive as indicated by the dramatically smaller sizes of the semicircles in the Nyquist plot (Figure 4.5A). A decrease in resistance indicates an increase in kinetic rates of charge transfer. The Bode plot (Figure 4.5B) indicates a significant change in frequency response between the two cations. The lower frequencies observed with Mg^{2+} present indicate a longer hole lifetime compared to when Li^+ is present. The change between Mg^{2+} and Li^+ is most clearly observed by noting the change in curvature of the traces. The exponential decay present with Mg^{2+}, but not Li^+, is indicative of a more diode-like characteristics. With Li^+ present, the charge transfer rate

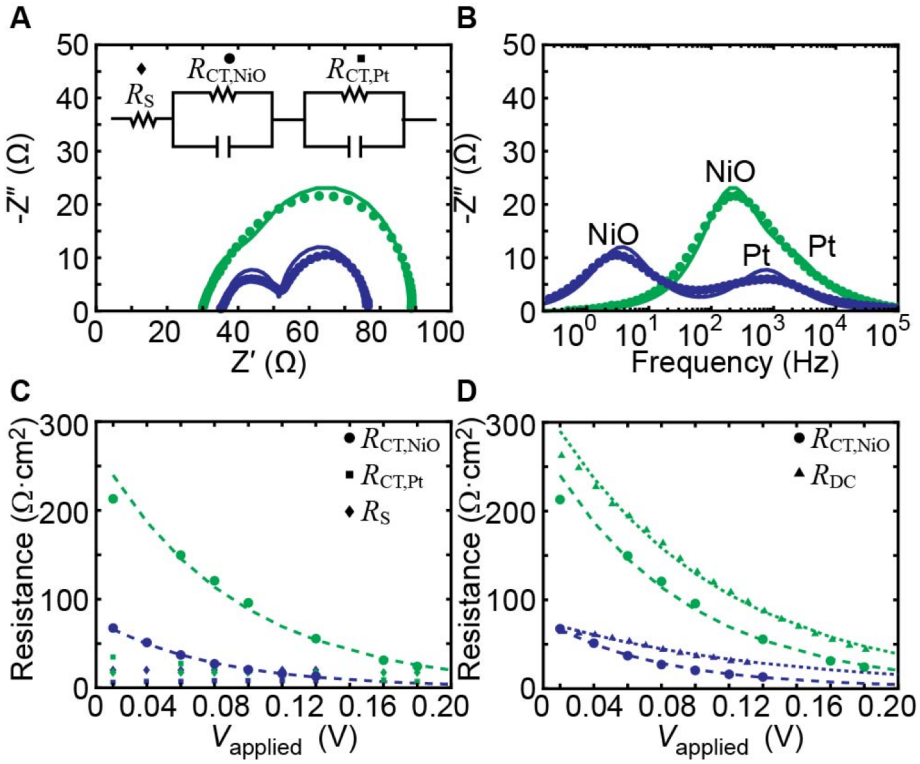

Figure 4.5. Electrochemical Impedance Spectroscopy on NiO. Li^+ data is plotted in green and Mg^{2+} data is plotted in blue. (A) Nyquist plots fitted with a double Randle's circuit. Dots are data points and the lines are the fitted curves. (B) Bode plot. (C-D) Charge transfer resistances (R_{CT}), and series resistance (R_S) measurements. Dashed lines are exponential fits.

(R_{ct}) is low enough that any charge can pass through the material without any selectivity. This improvement is reflected in device metrics as well. We can see an improvement in dark saturation current density, J_0, with 1.4 x 10^5 ± 0.5 x 10^5 A/cm^2 for Li^+ and 3.3 x 10^6 ± 0.8 x 10^6 A/cm^2 for Mg^{2+}. The higher dark saturation current is indicative of larger quantities of leaky current and higher rates of recombination.[29] We attribute improvement in diode characteristics as evidenced by an increase in shunt resistance from 1800 ± 200 Ω·cm^2 for Li^+ to 7300 ± 1400 Ω·cm^2 for Mg^{2+}. Additionally, we observe a significant increase in fill factor moving from 30.7 ± 0.3% with Li^+ present to 35.9 ± 0.8% with Mg^{2+} present.

Current-voltage (*J-V*) characterization indicates that the several cations studied introduce significant effects on device performance as is expected based on the previously discussed results as demonstrated in Figure 4.6A with selected trends plotted in Figure 4.6B.

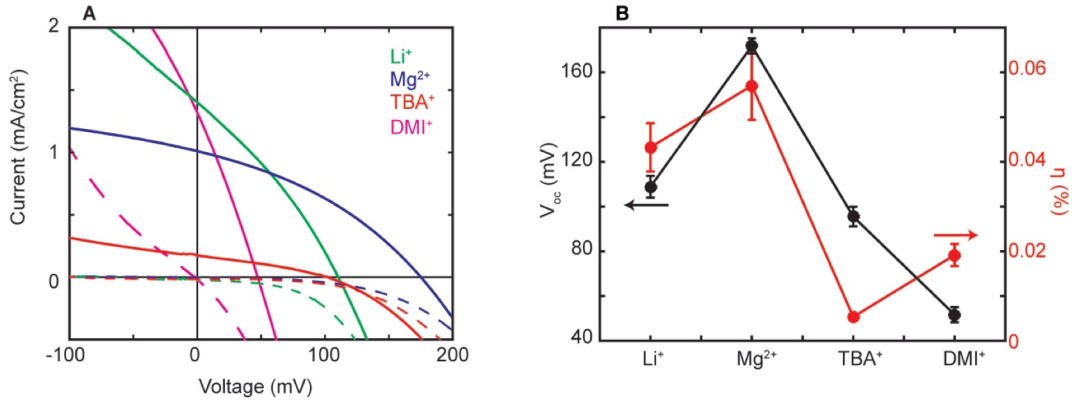

Figure 4.6. DSSC device characterization. (A) *J-V* curves for electrolytes containing various cations. (B) Device trends for V_{OC} and PCE from the average device metrics.

Table 4.1. *J-V* Metrics for NiO p-DSSCs using various cations.

Cation	J_{sc} (mA/cm^2)	V_{oc} (mV)	FF (%)	η (%)	J_0 x 10^{-5}(A/cm2)
Li^+	1.3 ± 0.1	109 ± 5	30.7 ± 0.3	0.043 ± 0.005	1.4 ± 0.5
Mg^{2+}	0.92 ± 0.1	172 ± 3	36.0 ± 0.8	0.057 ± 0.008	0.33 ± 0.06
TBA^+	0.18 ± 0.008	96 ± 4	31.3 ± 0.8	0.0053 ± 0.0004	0.66 ± 0.07
DMI^+	1.3 ± 0.1	51 ± 3	27.7 ± 0.3	0.019 ± 0.002	30 ± 8

Although there is a decrease in J_{sc} when Mg^{2+} is present, there is a dramatic increase in V_{oc} to 172 ± 3 mV from the second highest value with Li^+ of 109 ± 5 mV. The ~60 mV increase in V_{oc} can be attributed to a shift in the flat band potential (V_{FB}) of NiO as influenced by the various cations as shown in Figure 4.1. The maximum possible photovoltage is the difference between the Nernstian potential of the redox couple (I^-, I_3^-) and the V_{FB} of the semiconductor (NiO).

Consequently, if the flat band potential is significantly shifted to deeper states, the maximum photovoltage value also increases (assuming constant Nernstian potential), explaining the increase in V_{oc} measured from Mg^{2+} compared to other cations tested. The use of either TBA^+ resulted in a similar V_{oc} as Li^+ but the drop in J_{sc} from 1.3 ± 0.1 mA/cm^2 for Li^+ to 0.18 ± 0.008 mA/cm^2 caused TBA^+ to not be recommended for NiO devices in future. Additionally, although DMI^+ features the highest photocurrent produced matching that of Li^+, the poor dark curve performance and low V_{oc} of only 51 ± 3 mV, half of that of Li^+ devices, indicate that DMI^+ is also not a strong candidate for the cation present in NiO devices. Note AlI_3 is a reactive precursor and, consequently, devices using AlI_3 were not successfully pursued.

4.4: Conclusions

Cations in the electrolyte solution often produce unintended effects on significant parameters including the density of states near the band edge. Within the p-DSSC literature, cation effects have been ignored despite substantial attention paid within the n-DSSC community. The results presented here begin to investigate how cations impact p-DSSC performance yielding preliminary results that indicated substantial improvements can be gained with intentional choices regarding cations. Choosing a higher valence cation such as Mg^{2+} instead of Li^+ results in a boost to DSSC performance and most significantly a ~60 mV increase in V_{OC} and a twofold increase in PCE. Future work on the other components of the electrolyte including the redox couple itself and the additives is necessary to fully elucidate how p-DSSCs work.

4.5: Acknowledgements

This work was primarily funded by the UNC Energy Frontier Research Center, and EFRC funded by the U.S. Department of Energy, Office of Science, Office of Basic Energy Sciences, under award DE-SC0001011. Thank you to Taylor Moot for running EIS measurements.

REFERENCES

(1) O'Regan, B.; Grätzel, M. A Low-Cost, High-Efficiency Solar Cell Based on Dye-Sensitized Colloidal TiO_2 Films. *Nature* **1991**, *353*, 737–740.

(2) Kelly, C. A.; Farzad, F.; Thompson, D. W.; Stipkala, J. M.; Meyer, G. J. Cation-Controlled Interfacial Charge Injection in Sensitized Nanocrystalline TiO_2. *Langmuir* **1999**, *15* (20), 7047–7054.

(3) Maitani, M. M.; Tsukushi, Y.; Hansen, N. D. J.; Sato, Y.; Mochizuki, D.; Suzuki, E.; Wada, Y. Low-Temperature Annealing of Mesoscopic TiO_2 Films by Interfacial Microwave Heating Applied to Efficiency Improvement of Dye-Sensitized Solar Cells. *Sol. Energy Mater. Sol. Cells* **2016**, *147*, 198–202.

(4) Wang, H.; Liu, Y.; Li, M.; Huang, H.; Xu, H. M.; Hong, R. J.; Shen, H. Multifunctional TiO_2 Nanowires-Modified Nanoparticles Bilayer Film for 3D Dye-Sensitized Solar Cells. *Optoelectron. Adv. Mater. Rapid Commun.* **2010**, *4* (8), 1166–1169.

(5) Sigdel, S.; Dubey, A.; Elbohy, H.; Aboagye, A.; Galipeau, D.; Zhang, L.; Fong, H.; Qiao, Q. Dye-Sensitized Solar Cells Based on Spray-Coated Carbon nanofiber/TiO_2 Nanoparticle Composite Counter Electrodes. *J. Mater. Chem. A* **2014**, *2* (29), 11448.

(6) Dell'Orto, E.; Raimondo, L.; Sassella, A.; Abbotto, A. Dye-Sensitized Solar Cells: Spectroscopic Evaluation of Dye Loading on TiO_2. *J. Mater. Chem.* **2012**, *22* (22), 11364.

(7) Crossland, E. J. W.; Noel, N.; Sivaram, V.; Leijtens, T.; Alexander-Webber, J. A.; Snaith, H. J. Mesoporous TiO_2 Single Crystals Delivering Enhanced Mobility and Optoelectronic Device Performance. *Nature* **2013**, *495* (7440), 215–219.

(8) Flynn, C. J.; Oh, E. E.; McCullough, S. M.; Call, R. W.; Donley, C. L.; Lopez, R.; Cahoon, J. F. Hierarchically-Structured NiO Nanoplatelets as Mesoscale P-Type Photocathodes for Dye-Sensitized Solar Cells. *J. Phys. Chem. C* **2014**, *118* (26), 14177–14184.

(9) Wei, L.; Jiang, L.; Yuan, S.; Ren, X.; Zhao, Y.; Wang, Z.; Zhang, M.; Shi, L.; Li, D. Valence Band Edge Shifts and Charge-Transfer Dynamics in Li-Doped NiO Based P-Type DSSCs. *Electrochim. Acta* **2016**, *188*, 309–316.

(10) Dini, D.; Halpin, Y.; Vos, J. G.; Gibson, E. a. The Influence of the Preparation Method of NiOx Photocathodes on the Efficiency of P-Type Dye-Sensitized Solar Cells. *Coord. Chem. Rev.* **2015**, *304–305*, 179–201.

(11) Wood, C. J.; Summers, G. H.; Clark, C. A.; Kaeffer, N.; Braeutigam, M.; Carbone, L. R.; D'Amario, L.; Fan, K.; Farré, Y.; Narbey, S.; et al. A Comprehensive Comparison of Dye-Sensitized NiO Photocathodes for Solar Energy Conversion. *Phys. Chem. Chem. Phys.* **2016**, *18*, 10727–10738.

(12) Click, K. A.; Beauchamp, D. R.; Garrett, B. R.; Huang, Z.; Hadad, C. M.; Wu, Y. A Double-Acceptor as a Superior Organic Dye Design for P-Type DSSCs: High Photocurrents and the Observed Light Soaking Effect. *Phys. Chem. Chem. Phys.* **2014**, *16* (47), 26103–26111.

(13) He, J.; Lindström, H.; Hagfeldt, A.; Lindquist, S.-E. Dye-Sensitized Nanostructured P-Type Nickel Oxide Film as a Photocathode for a Solar Cell. *J. Phys. Chem. B* **1999**, *103*, 8940–8943.

(14) Powar, S.; Daeneke, T.; Ma, M. T.; Fu, D.; Duffy, N. W.; Gotz, G.; Weidelener, M.; Mishra, A.; Bauerle, P.; Spiccia, L.; et al. Highly Efficient P-Type Dye-Sensitized Solar Cells Based on tris(1,2-diaminoethane)cobalt(II)/(III) Electrolytes. *Angew. Chemie - Int. Ed.* **2013**, *52* (2), 602–605.

(15) Perera, I. R.; Daeneke, T.; Makuta, S.; Yu, Z.; Tachibana, Y.; Mishra, A.; Bäuerle, P.; Ohlin, C. A. A.; Bach, U.; Spiccia, L.; et al. Application of the tris(acetylacetonato)iron(III)/(II) Redox Couple in P-Type Dye-Sensitized Solar Cells. *Angew. Chemie - Int. Ed.* **2015**, *54* (12), 3758–3762.

(16) Redmond, G.; Fitzmaurice, D. Spectroscopic Determination of Flatband Potentials for Polycrystalline Titania Electrodes in Nonaqueous Solvents. *J. Phys. Chem.* **1993**, *97* (7), 1426–1430.

(17) Kakiage, K.; Aoyama, Y.; Yano, T.; Oya, K.; Fujisawa, J.; Hanaya, M. Highly-Efficient Dye-Sensitized Solar Cells with Collaborative Sensitization by Silyl-Anchor and Carboxy-Anchor Dyes. *Chem. Commun.* **2015**, *51* (88), 15894–15897.

(18) Green, M. A. Third Generation Photovoltaics: Solar Cells for 2020 and beyond. *Phys. E Low-Dimensional Syst. Nanostructures* **2002**, *14* (1–2), 65–70.

(19) Alibabaei, L.; Luo, H.; House, R. L.; Hoertz, P. G.; Lopez, R.; Meyer, T. J. Applications of Metal Oxide Materials in Dye Sensitized Photoelectrosynthesis Cells for Making Solar Fuels: Let the Molecules Do the Work. *J. Mater. Chem. A* **2013**, *1* (13), 4133.

(20) O'Donnell, R. M.; Sampaio, R. N.; Barr, T. J.; Meyer, G. J. Electric Fields and Charge Screening in Dye Sensitized Mesoporous Nanocrystalline TiO_2 Thin Films. *J. Phys. Chem. C* **2014**, *118* (30), 16976–16986.

(21) Wang, H.; Peter, L. M. Influence of Electrolyte Cations on Electron Transport and Electron Transfer in Dye-Sensitized Solar Cells. *J. Phys. Chem. C* **2012**, *116* (19), 10468–10475.

(22) Jeanbourquin, X. A.; Li, X.; Law, C.; Barnes, P. R. F.; Humphry-Baker, R.; Lund, P.; Asghar, M. I.; Oregan, B. C. Rediscovering a Key Interface in Dye-Sensitized Solar Cells: Guanidinium and Iodine Competition for Binding Sites at the Dye/electrolyte Surface. *J. Am. Chem. Soc.* **2014**, *136* (20), 7286–7294.

(23) Ito, S.; Murakami, T. N.; Comte, P.; Liska, P.; Grätzel, C.; Nazeeruddin, M. K.; Grätzel,

M. Fabrication of Thin Film Dye Sensitized Solar Cells with Solar to Electric Power Conversion Efficiency over 10%. *Thin Solid Films* **2008**, *516* (14), 4613–4619.

(24) McCullough, S. M.; Flynn, C. J.; Mercado, C. C.; Nozik, A. J.; Cahoon, J. F. Compositionally-Tunable Mechanochemical Synthesis of $Zn_xCo_{3-x}O_4$ Nanoparticles for Mesoporous P-Type Photocathodes. *J. Mater. Chem. A* **2015**, *3*, 21990–21994.

(25) Flynn, C. J.; McCullough, S. M.; Li, L.; Donley, C. L.; Kanai, Y.; Cahoon, J. F. Passivation of Nickel Vacancy Defects in Nickel Oxide Solar Cells by Targeted Atomic Deposition of Boron. *J. Phys. Chem. C* **2016**, *120* (30), 16568–16576.

(26) Flynn, C. J.; McCullough, S. M.; Oh, E.; Li, L.; Mercado, C. C.; Farnum, B. H.; Li, W.; Donley, C. L.; You, W.; Nozik, A. J.; et al. Site-Selective Passivation of Defects in NiO Solar Photocathodes by Targeted Atomic Deposition. *ACS Appl. Mater. Interfaces* **2016**, *8*, 4754–4761.

(27) Huang, Z.; Natu, G.; Ji, Z.; Hasin, P.; Wu, Y. P-Type Dye-Sensitized NiO Solar Cells : A Study by Electrochemical Impedance Spectroscopy. *J. Phys. Chem. C* **2011**, *115* (50), 25109–25114.

(28) Wang, Q.; Moser, J.; Grätzel, M. Electrochemical Impedance Spectroscopic Analysis of Dye-Sensitized Solar Cells. *J. Phys. Chem. B* **2005**, 14945–14953.

(29) Cuevas, A. The Recombination Parameter J_0. *Energy Procedia* **2014**, *55*, 53–62.

Chapter 5: Compositionally-Tunable Mechanochemical Synthesis of $Zn_XCo_{3-X}O_4$ Nanoparticle for Mesoporous Photocathodes[1]

5.1 Introduction

A key challenge facing the modern world lies in the development and implementation environmentally-friendly energy sources. Mesoporous dye-sensitized solar cells (DSSCs) have been extensively studied since their first report in 1991.[1] The highest performing DSSCs in the literature feature power conversion efficiencies exceeding 12% and use an n-type TiO_2 photoanode as the working electrode.[2] Analogous p-type DSSCs can, in principle, achieve comparable efficiencies with the circuit operating in reverse by replacing the photoanode with a photocathode. However, the current efficiency record is 2.55% using NiO, the champion photocathode material to-date.[3] The underperformance of NiO compared to TiO_2 demands the investigation of alternate materials, which is an active area of research including, for instance, efforts to develop $Ni_xCo_{3-x}O_4$ and Cu(I) delafossites.[4–6]

A DSSC is a solar-to-electric photovoltaic device that typically features one photoactive electrode, either an n-type anode or a p-type cathode, and one dark counter

[1] This chapter previously appeared as an article in the Journal of Materials Chemistry A. The original citation is as follows: McCullough, S. M.; Flynn, C. J.; Mercado, C. C.; Nozik, A. J.; Cahoon, J. F. Compositionally-Tunable Mechanochemical Synthesis of $Zn_XCo_{3-x}O_4$ Nanoparticles for Mesoporous P-Type Photocathodes. *J. Mater. Chem. A* **2015**, *3*, 21990–21994.

electrode, typically Pt. In a tandem configuration, however, the anode and cathode are placed in series and both are photoactive, allowing for complementary light absorbance and a larger photovoltage. Moreover, tandem solar fuel devices, such as dye-sensitized photoelectrosynthesis cells (DSPECs),[7] can synthesize solar fuels by integrating molecular catalysts that store solar energy in a chemical bond. With current materials, the photocathode significantly limits the performance of a DSPEC or similar tandem device, further motivating interest in identifying new materials.[7–12]

$ZnCo_2O_4$ is a candidate p-type semiconductor that crystallizes in the cubic spinel lattice.[13–15] The general spinel formula, AB_2O_4, features a divalent metal, A, tetrahedrally coordinated to oxygen, and a trivalent metal, B, octahedrally coordinated to oxygen. For example, Co_3O_4 is a spinel, consisting of one Co^{2+} and two Co^{3+}. $ZnCo_2O_4$ can be considered a substituted Co_3O_4 material, where Zn^{2+} replace the Co^{2+} cations. The Zn^{2+} substitution results in a change in several material properties that are beneficial to p-type DSSCs including increasing the optical band gap, conductivity, doping level, and hole mobility.[14,15] A dense thin-film of $ZnCo_2O_4$ has previously been reported in a DSSC configuration.[13] However, a high surface area mesoscale form is critical for increasing the light-harvesting efficiency of $ZnCo_2O_4$. Nanostructures of $ZnCo_2O_4$ have been reported for applications in catalysis and batteries.[16–22] Here, we present a novel solid-state synthesis of phase-pure $Zn_xCo_{3-x}O_4$ nanoparticles with highly tunable Zn stoichiometry, and we present the first report of p-type DSSCs using mesoscopic $Zn_xCo_{3-x}O_4$ films.

5.2 Experimental Materials and Methods

5.2.a Materials and Reagents.

Acetonitrile (99.6%), cobalt nitrate hexahydrate (reagent grade), iodine (>99.99%), lithium iodide, lithium perchlorate (>99%), and zinc nitrate hexahydrate (reagent grade) were all purchased from Sigma-Aldrich. Methyl methacrylate (MMA) and poly(methyl methacrylate) (PMMA) were purchased from Microchem. Absolute ethanol (Decon Laboratories), isopropyl alcohol (IPA; electronics grade), and sodium hydroxide (pellets/certified ACS) were purchased from Fisher Scientific. 25 μm thick Surlyn polymer was purchased from Solaronix. P1 chromophore was purchased from Dynamo. All chemicals were used as received. Fluorine-doped tin oxide (FTO) glass (TEC 15 $\Omega \cdot cm^2$) was purchased from Hartford glass and cleaned with typical organic solvents and sonication.

5.2.b $Zn_xCo_{3-x}O_4$ Nanoparticle Synthesis

$Zn_xCo_{3-x}O_4$ was prepared by manually grinding together desired ratios of $Zn(NO_3)_2 \cdot 6H_2O$, $Co(NO_3)_2 \cdot 6H_2O$, and NaOH in an agate mortar and pestle for 3 minutes to form a hydroxide precursor, $Zn_xCo_{3-x}(OH)_6$. $Zn_xCo_{3-x}(OH)_6$ was rinsed with 50 mL deionized H_2O, collected via centrifugation, and dried at 40°C in air overnight prior to calcination. $Zn_xCo_{3-x}(OH)_6$ was calcined at 400°C in an open air furnace (40 mins) to produce nanoparticulate $Zn_xCo_{3-x}O_4$.

5.2.c Spin casting paste preparation

Spin coating pastes were prepared with 10% weight metal oxide, 10% weight hydroxypropyl cellulose (HPC), 40% weight deionized water, and 40% weight ethylene glycol. Homogenization procedures included sonication, vigorous magnetic stirring, and ball milling.

Thin film mesoscopic electrodes were prepared using a Laurell WS-650Mz-23NPP spin coater. Spin coated films were subsequently annealed at specified temperatures in various atmospheres. Annealed films were trimmed to an active area of ~0.25 cm^2.

5.2.d Analytical methods.

Powder x-ray diffraction (PXRD) studies were performed on a Rigaku Multiflex diffractometer at a scan rate of 2^o 2θ/min on powder samples. Profilometry measurements were performed on a KLA Tencore P-6 profilometer on mesoscopic films with a step edge. Scanning electron microscopy imaging was performed on a FEI Helios NanoLab DualBeam D600 FIB system. TEM imaging was performed on a FEI Titan 80-300 probe aberration corrected scanning transmission electron microscope with a Bruker 4 SDD EDS system for EDS mapping. Bulk elemental composition was measured using an INCA PentaFet –x3 system installed on the FIB system. Optical absorbance measurements were obtained with a Cary 5000 UV-Vis-NIR spectrometer using an integrating sphere. X-ray photoelectron spectroscopy (XPS) and ultraviolet photoelectron spectroscopy (UPS) were performed on a Kratos Axis Ultra DLD X-ray Photoelectron Spectrometer. Mott-Schottky analysis was performed via AC impedance spectroscopy in a three electrode cell with 0.1 M $LiClO_4$ acetonitrile electrolyte. The working electrode was the $Zn_xCo_{3-x}O_4$ mesoscopic film on FTO, the counter electrode was Pt mesh, and the reference electrode was Ag/AgCl. Electrochemical measurements were performed on a CH Instruments model 604E potentiostat. Seebeck measurements were performed on ~7 μm thick nanoparticle films. The films were contacted to the thermoelectric measurement heating plates with indium metal and measurements were taken after equilibrating for 6 minutes. The Seebeck

coefficient was calculated from measurements taken at ~295 K using a Keithley 182 Sensitive Digital voltmeter with the heating plate temperature controlled by a Lakeshore 330 controller.

5.2.e Microelectrode Fabrication and Conductivity Measurements.

Microelectrode patterns were fabricated using a literature procedure.[23] Au pads were prepared via electron beam lithography using a Hitachi S4700 SEM on MMA/PMMA films and developed with methyl-isobutyl ketone (MIBK). Chromium and gold were deposited (3 nm and 50 nm respectively) using electron beam evaporation before lift-off with acetone. $Zn_xCo_{3-x}O_4$ films were spin cast on the microelectrode patterns and subsequently annealed. Conductivity measurements were performed using a Keithley 2636A SourceMeter with Signatone micropositioners (S-725) and probe tips (SE-TL).

5.2.f Dye-loading measurements.

Dye-loading was quantified using the change in absorbance values (Figure S6) and the maximum extinction coefficient of P1, 5.8 x 10^4 $M^{-1}\cdot cm^{-1}$ at 468 nm.[24]

5.2.g DSSC assembly and characterization.

Processed thin films were submerged in a 0.3 mM P1 acetonitrile solution overnight. Platinum counter electrodes were fabricated on FTO glass with a powder-blasted pinhole. A 5 mM H_2PtCl_6 solution in IPA was dropcast on the FTO and annealed at 380 ^oC for 30 mins in air to produce the Pt counter electrode thin film. The DSSC was sandwiched using a 25 um thick Surlyn polymer gasket using a custom-built heating apparatus. Sandwiched devices were backfilled with

electrolyte (10:1 LiI:I_2 in acetonitrile) using a custom-built vacuum chamber. The cell is sealed with additional Surlyn polymer and a microscope coverslip. The AM 1.5G illumination source was a Newport Oriel 150W Class ABB Solar Simulator which was calibrated before each use with a certified reference Newport 91150 V solar cell. A Keithley 2636A SourceMeter was used for all electrical measurements.

5.3 Results and Discussion

$Zn_xCo_{3-x}O_4$ spherical nanoparticles were synthesized via a mechanochemical solid-state preparation. Typical mechanochemical syntheses require high levels of mechanical energy introduced via ball milling over several hours.[25,26] In contrast, the preparation developed here is a highly facile, low-energy reaction using manual grinding of $Co(NO_3)_2 \cdot 6H_2O$, $Zn(NO_3)_2 \cdot 6H_2O$ and NaOH to form a mixed metal hydroxide of general formula $Zn_xCo_{3-x}(OH)_6$, as shown in Figure 5.1A. Upon calcination at temperatures ranging from 300 to 500 °C, a phase-pure spinel is observed. An advantage of this synthesis is that by simply tuning the starting ratio of cobalt and zinc nitrates, the Zn concentration in the spinel lattice is directly tuned. Five Zn concentrations were studied, where x = 0, 0.25, 0.5, 0.75, and 1, given the general formula, $Zn_xCo_{3-x}O_4$. The morphology of the hydroxide and calcined oxide are confirmed via scanning electron microscopy (SEM) imaging, and the oxide forms nanospheres of 24 ± 5 nm diameter as shown in Figure 5.1B-C. The nanospheres form because of the significant change in density between the oxide (6.11

$g \cdot cm^{-1}$) and the hydroxide (3.60 $g \cdot cm^{-1}$).[27]

Elemental composition of $Zn_xCo_{3-x}O_4$ was analyzed via energy-dispersive x-ray spectroscopy (EDS), confirming that the Zn concentration is unchanged throughout the synthesis (Figure 5.2A) and is facilely adjusted within the range of x = 0 to x = 1. Prior to calcination, any unreacted material is rinsed away with H_2O. The synthetic preparation is described in detail in Section 5.2.b. Powder x-ray diffraction (PXRD) patterns (Figure 5.2B) show peaks consistent with spinel lattice. Notably, no peaks characteristic of a wurtzite phase are present in any sample, indicating the absence of ZnO. X-ray photoelectron spectroscopy (XPS) confirms the presence of Zn^{2+} and Co^{3+} (Figure 5.4). To characterize the uniformity of Zn within the nanoparticles, EDS mapping in a scanning transmission electron microscope (STEM) was performed, confirming a homogeneous

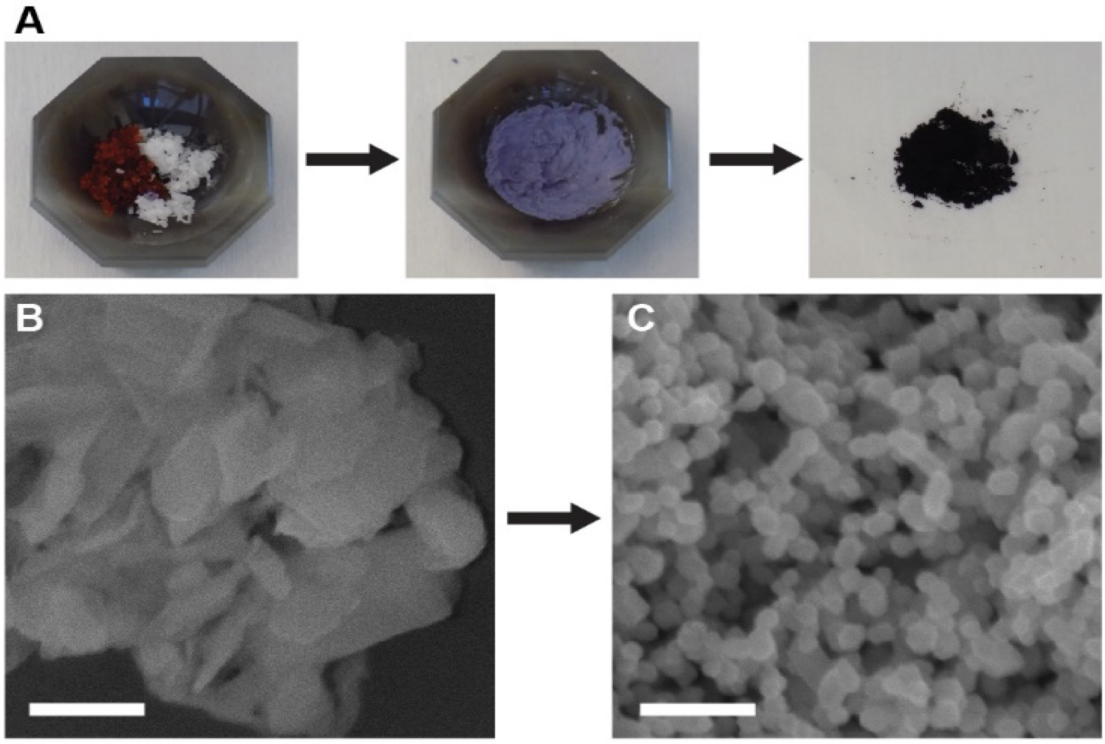

Figure 5.1. Mechanochemical synthesis of $Zn_xCo_{3-x}O_4$. (A) Optical images of solid-state nanoparticle synthesis of $Zn_xCo_{3-x}O_4$, showing conversion of the metal salts (left) to the mixed metal hydroxide (middle) and finally the metal oxide (right). (B and C) SEM images of $ZnCo_2(OH)_6$ nanosheets (panel B) and $ZnCo_2O_4$ nanoparticles (panel C). Scale bars, 100 nm.

composition throughout the material, as shown in Figure 5.5.

The $Zn_xCo_{3-x}O_4$ nanoparticles were processed into thin films on glass slides by spin casting pastes prepared by a modification of literature procedures[28] (see section 5.2.c). As shown in Figure 5.3, the films are black, and absorbance spectra show increasing absorbance in the 300-500 nm range with increasing Zn concentration. Tauc plots (Figure 5.6) were used to determine the band gaps, as shown in Figure 3B, for each Zn stoichiometry. As the Zn concentration increases, the band gap also increases. The band gap of $ZnCo_2O_4$ is 2.17 eV, which agrees well with the literature value of 2.2 eV.[14] With decreasing Zn concentration, the optical band gap decreases to a value of 1.85 eV for Co_3O_4, also in agreement with literature values of 1.8 eV.[29]

We probed the electrical transport characteristics of $Zn_xCo_{3-x}O_4$ by measuring the

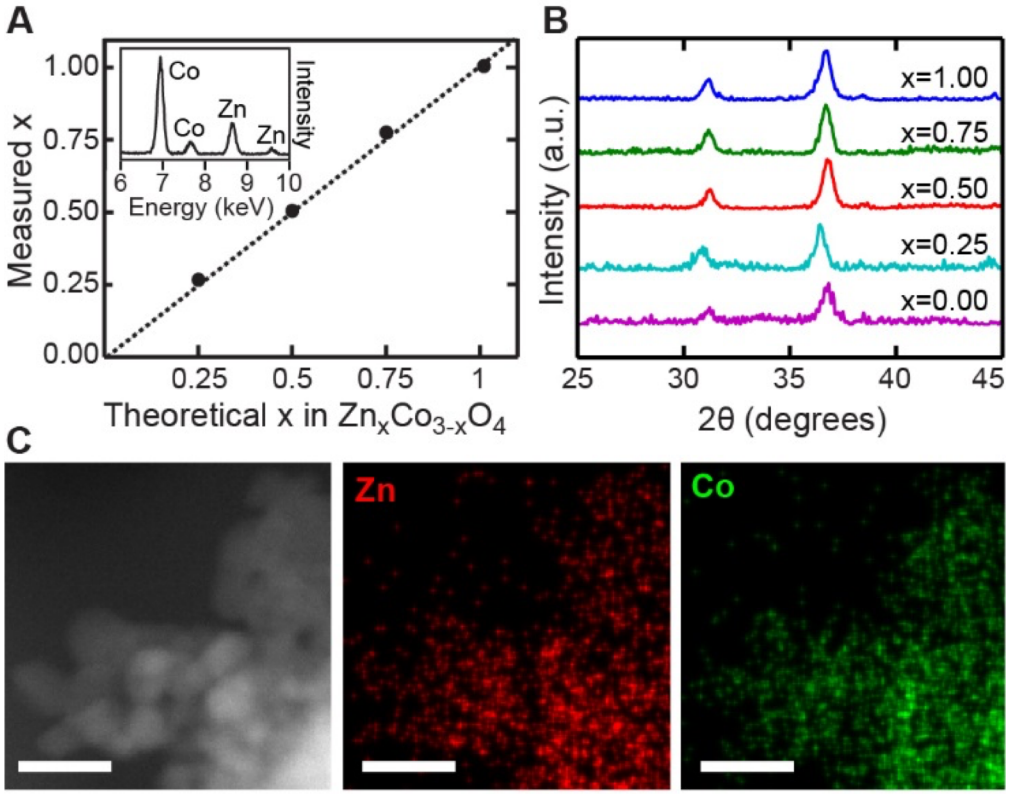

Figure 5.2. Chemical composition of $Zn_xCo_{3-x}O_4$. (A) Zn stoichiometry as measured by EDS. Inset: EDS spectrum of $ZnCo_2O_4$. (B) PXRD patterns for all Zn stoichiometries of $Zn_xCo_{3-x}O_4$. (C) STEM image (left) and EDS maps of Zn (middle) and Co (right). Scale bars, 20 nm.

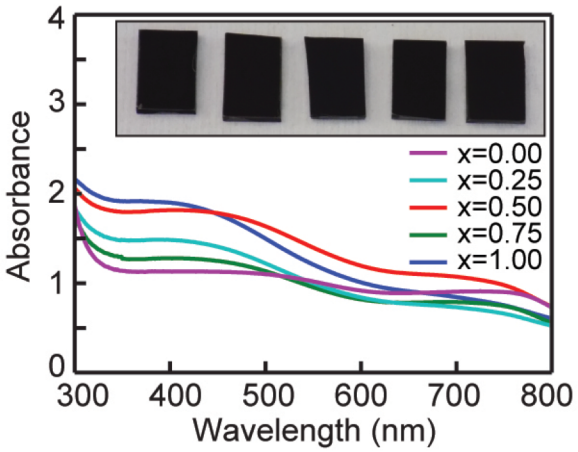

Figure 5.3. Optical properties. Absorbance spectra of $Zn_xCo_{3-x}O_4$ with various stoichiometries. Inset: photograph of 1.2 μm-thick films with Zn stoichiometries from left to right: x = 0, 0.25, 0.50, 0.75, 1.

conductivity and doping level of thin films (Figure 5.7A). Conductance measurements performed with micron-scale electrodes (Figure 5.8) indicate that the conductivity increases by two orders of magnitude with increasing Zn concentration. Mott-Schottky analysis (Figure 5.9) yielded the doping level of each stoichiometry of $Zn_xCo_{3-x}O_4$ (Figure 5.7A).[30] The doping concentration increased by more than one order of magnitude as the Zn substitution increased. This increase most likely results either from an increase in cation vacancies or an increase in the divalent metal (Zn^{2+}) occupying a trivalent site (Co^{3+}),

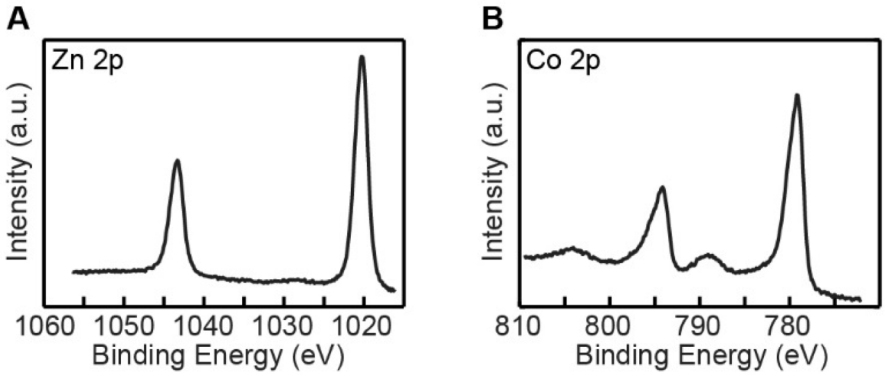

Figure 5.4. XPS spectra of $Zn_xCo_{3-x}O_4$ collected in the (A) Zn 2p region and (B) Co 2p region. On the basis of literature data, peaks at 1043.4 eV and 1020.3 eV are assigned to Zn^{2+}.[38] Main peaks at 794.1 eV and 780.0 eV are observed for several cobalt oxidation states. Satellite peaks at 804.1 eV and 789.1 eV are attributed to Co^{3+}.[39]

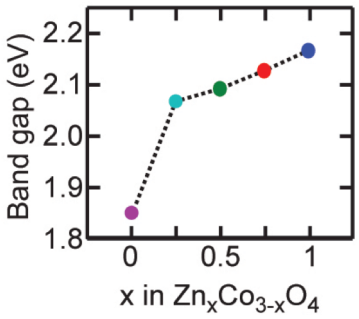

Figure 5.5. Optical properties of $Zn_xCo_{3-x}O_4$. Optical bandgap of various stoichiometries of $Zn_xCo_{3-x}O_4$.

consistent with previous reports.[14,15,31] The electrical mobility of $Zn_xCo_{3-x}O_4$ (Figure 5.7B) was determined from the conductivity and doping level and shows an increase of more than one order of magnitude with increasing Zn concentration. The values range from a low of 2.41 x 10^{-5} $cm^2 \cdot V^{-1} \cdot s^{-1}$ for x = 0 to a maximum of 3.58 x 10^{-4} $cm^2 \cdot V^{-1} \cdot s^{-1}$ for x = 0.75. The measured mobility value for Co_3O_4 is on the same order-of-magnitude as literature values.[32,33] The mobility of the mesoscopic $ZnCo_2O_4$ is approximately two orders of magnitude lower than the previously-reported dense thin film.[13] The difference can be attributed to interparticle hopping required for charge transport in the nanoparticle film. Compared to previous reports on NiO mesoporous films, mobility values of $Zn_xCo_{3-x}O_4$ are

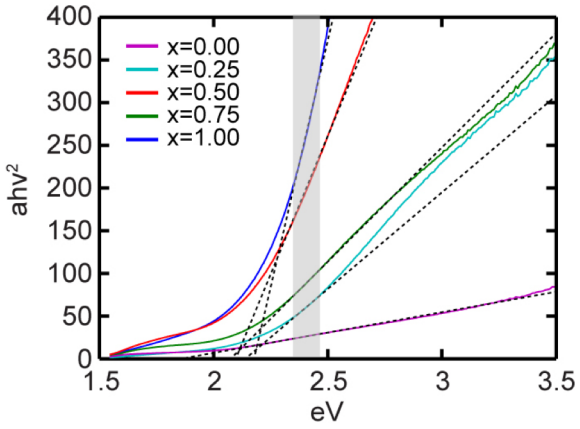

Figure 5.6. Tauc plot of $Zn_xCo_{3-x}O_4$. Shaded area denotes the region fit to a line. Dashed lines represent the linear fits used to determine the bandgap by intercepts with the horizontal axis.

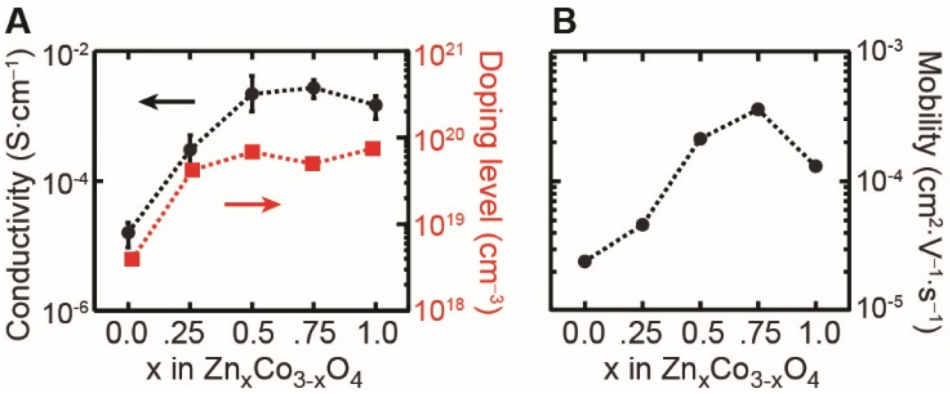

Figure 5.7. Electrical transport properties of $Zn_xCo_{3-x}O_4$. (A) Conductivity (black circles and left-hand axis) and doping level (red squares and right-hand axis) as a function of Zn stoichiometry. (B) Electrical mobility as a function of Zn stoichiometry.

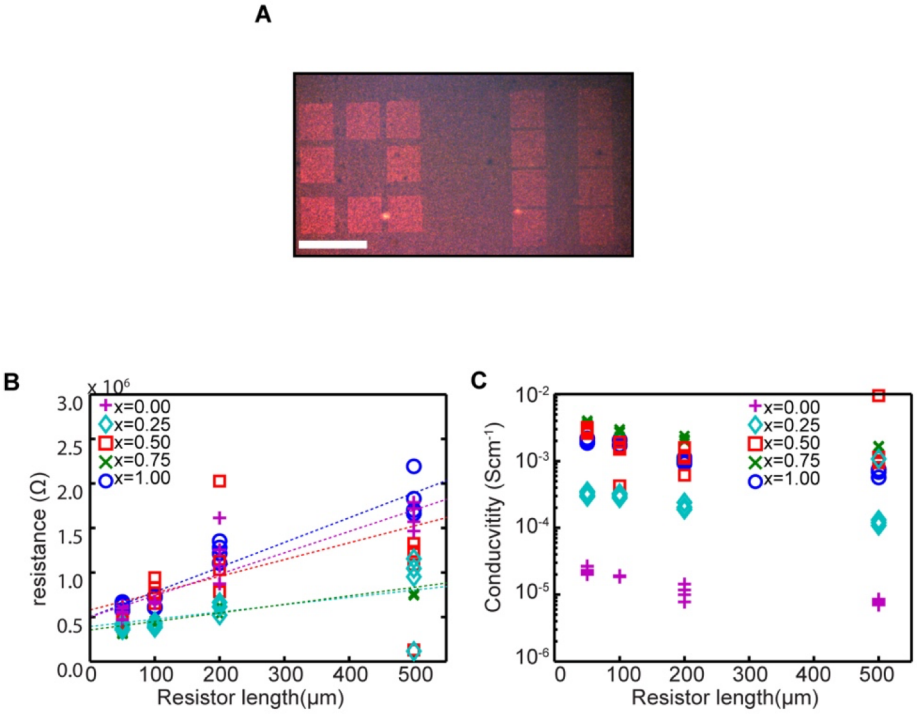

Figure 5.8. Conductivity measurements on $Zn_xCo_{3-x}O_4$.(A) Optical image of a microelectrode pattern consisting of 3 nm Cr and 50 nm Au pads fabricated by electron-beam lithography and metal evaporation. A thin-film 800 nm thick was spin cast on top of the electrodes; scale bar, 1 mm. (B and C) Resistance *vs*. resistor length for $Zn_xCo_{3-x}O_4$, where the resistor length is the distance between microelectrode pads. x = 0.00 data scaled by a factor of 0.01; x = 0.25 data scaled by a factor of 0.1. Dashed lines represent linear fits to data sets for each stoichiometry, and conductivity values were calculated from the slope of the line using a film thickness of 800 nm.

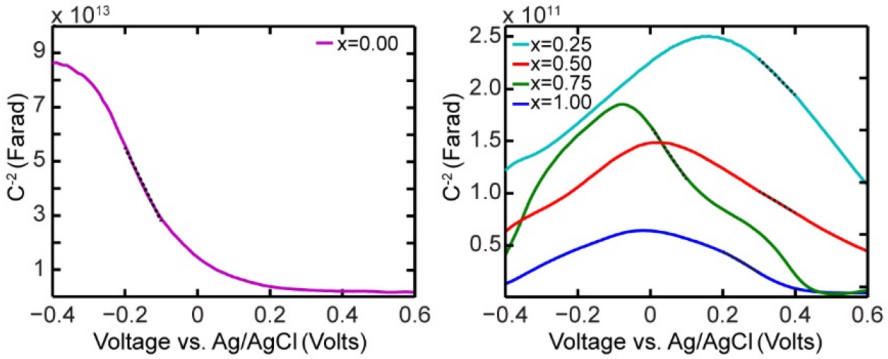

Figure 5.9. Mott-Schottky plots of $Zn_xCo_{3-x}O_4$. Linear fits to extract slopes shown as dashed lines. Mott-Schottky analysis performed in a three electrode cell at 1 Hz.

comparable given similar annealing conditions.[23] The Seebeck coefficient of $ZnCo_2O_4$ was measured to be 8050 ± 10 $V \cdot K^{-1}$ (Figures 5.10), additionally confirming the p-type conductivity of the material.

DSSCs were fabricated to probe how the $Zn_xCo_{3-x}O_4$ thin films perform as a mesoscopic hole-conducting photocathodes. Devices with all five Zn concentrations were prepared using 1.2 μm-thick films, the P1 molecular chromophore, and an I^-/I_3^- acetonitrile

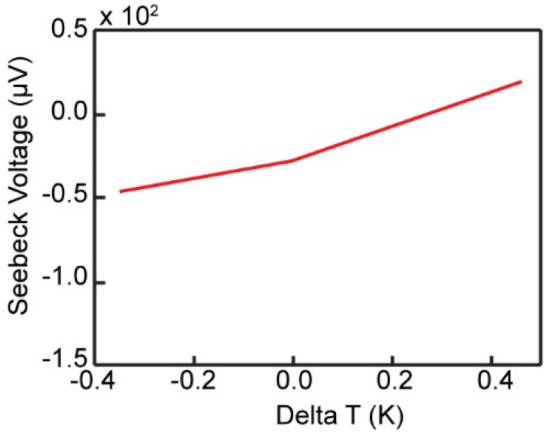

Figure 5.10. Seebeck measurement for $ZnCo_2O_4$. The Seebeck coefficient measured is 8050 ± 10 $V \cdot K^{-1}$. The Seebeck coefficient is the ratio between the voltage differences over the temperature change.

electrolyte. Full experimental conditions are described in section 5.2.g. Current density-voltage (*J-V*) characteristics were collected in the dark and under AM1.5G one-sun illumination. *J-V* curves are plotted in Figure 5.9A for all Zn concentrations. Full metrics are provided in Table 5.1. With increasing Zn substitution in the spinel lattice, the short-

Table 5.1. *J-V* metrics for $Zn_xCo_{3-x}O_4$ DSSCs

X: $Zn_xCo_{3-x}O_4$	Average J_{sc} ($mA \cdot cm^{-2}$)	Average V_{oc} (mV)	FF (%)	η (%)
0.00	0.11 ± 0.02	106 ± 7	34 ± 2	0.0039 ± 0.0005
0.25	0.17 ± 0.06	111 ± 8	33.6 ± 0.9	0.0064 ± 0.002
0.50	0.21 ± 0.03	108 ± 2	34.3 ± 0.6	0.0080 ± 0.002
0.75	0.27 ± 0.05	114 ± 3	35.2 ± 0.2	0.011 ± 0.002
1.00	0.37 ± 0.09	128 ± 5	33.8 ± 0.1	0.016 ± 0.004

circuit current density (J_{sc}) increased significantly, ranging from 0.11 ± 0.02 $mA \cdot cm^{-2}$ to 0.37 ± 0.09 $mA \cdot cm^{-2}$ for Co_3O_4 and $ZnCo_2O_4$, respectively (Figure 5.5B). We attribute the increase in current to the substantial increase in mobility. Absorption spectroscopy (Figure 5.10) confirmed that the dye-loading on all samples was the same (Figure 511B), and, therefore, not the cause for an increase in J_{sc}. Methods used to quantify dye-loading are described in Section 5.2.f.

Further material and device optimization was pursued on the highest performing Zn concentration, $ZnCo_2O_4$. The P1 chromophore features a carboxylic acid linker group which binds to a metal oxide via a surface oxygen.[34] Poor oxygen coverage of the surface would explain the relatively poor dye loading on $ZnCo_2O_4$ compared to other metal oxides.[35] It is possible for the surface to be metal-terminated as a result of carbothermal reduction, which can occur in the presence of the polymer, hydroxypropyl cellulose (HPC),

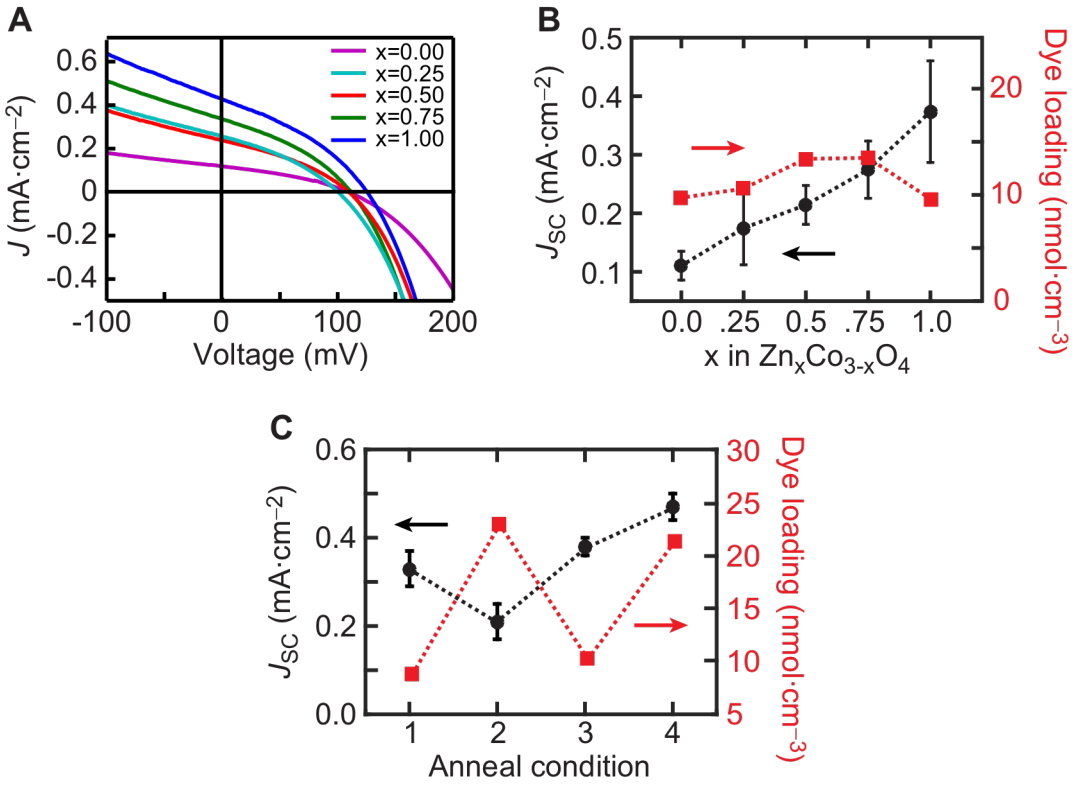

Figure 5.11. $Zn_xCo_{3-x}O_4$ DSSC characterization. (A) *J-V* curves under 1-sun illumination for $Zn_xCo_{3-x}O_4$ of various stoichiometries calcined in air at 300 °C. (B and C) J_{sc} (black circles and left-hand axes) and dye-loading (red squares and right-hand axes) as a function of Zn stoichiometry (panel B) and as a function of annealing condition for $ZnCo_2O_4$ (panel C). In panel C, annealing conditions are 1: air 300 °C; 2: UVO 200°C; 3: UVO 200 °C, air 300 °C; 4: UVO 50 °C; air 300 °C, UVO 200 °C.

used to process the nanoparticles into a paste for spin casting. Annealing the spin-cast films at sufficiently high temperatures (≥300 °C) in air results in a combustion reaction of the HPC, leaving behind the mesoporous metal oxide thin films. However, these conditions are also favorable for a carbothermal reduction because of the presence of hydrocarbons, oxygen, and sufficiently high temperatures.[36] Although these processing conditions are standard for n-type DSSCs, TiO_2, an exceptionally stable metal oxide, is unlikely to undergo carbothermal reduction.[36,37] Consequently, methods used for n-type DSSCs cannot necessarily be translated to p-type DSSCs, and separate processing conditions will often need to be developed.

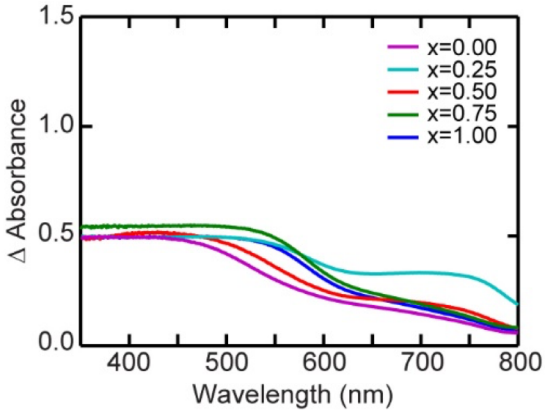

Figure 5.12. Change in absorbance for $Zn_xCo_{3-x}O_4$ thin films dyed with the P1 molecular chromophore.

Operating under the hypothesis that dye-loading would improve with increased surface oxygen, we pursued alternate strategies to produce a mesoscopic thin film of $ZnCo_2O_4$. The films were treated in an environment more oxidizing than air by using an ultraviolet/ozone (UVO) system. The UVO treatment allows for the HPC removal at lower temperatures via alternate reaction mechanisms. Ozone can strip away the HPC, leaving a mesoporous thin film while preventing carbothermal reduction and maintaining the oxygen-terminated surface. When the films were treated only at 200 °C under UVO atmosphere (condition 2), a nearly three-fold increase in dye-loading, from 8.8 to 23 $nmol \cdot cm^{-3}$, was observed compared to films annealed in air at 300 °C. UVO-treated films were then tested in a DSSC configuration.

Figure 5.11C illustrates the changes in photocurrent and dye-loading with successive annealing treatments. Although the UVO treated films (condition 2) featured higher dye-loading, the J_{sc} decreased by 21% to 0.26 ± 0.04 $mA \cdot cm^{-2}$. We hypothesized that the low-temperature UVO treatment preserved the oxygen-terminated surface advantageous for dye-loading but was insufficient to sinter the individual nanoparticles together to create an electrically interconnected, mesoporous scaffold. By combining the two annealing techniques, allowing for the UVO removal

of the HPC at low temperatures and electrical sintering of the particles at higher temperatures in air, the J_{sc} improves from 0.26 ± 0.04 mA·cm^{-2} to 0.38 ± 0.02 mA·cm^{-2}. The order of the annealing treatments dictates the device performance. Several conditions were tested, and we report a subset here (Figure 5.9C) to demonstrate trends. The most successful process (annealing condition 4) results from three successive treatments of the film. First, the HPC is removed via a low-temperature (50 °C) UVO treatment. Second, a high-temperature air anneal at 300 °C electrically sinters the film, and third, a 200 °C UVO treatment increases the oxygen concentration on the surface, which led to the highest J_{sc} of 0.47 ± 0.04 mA·cm^{-2}, a one-sun power-conversion efficiency of 0.025 %, and a dye loading of 21 nmol·cm^{-2}. Finally, incident photon-to-current efficiency for a $ZnCo_2O_4$ DSSC was measured and compared to the absorbance profile of the dye used, P1, to confirm the origin of the photocurrent is from the chromophore as shown in Figure 5.13.

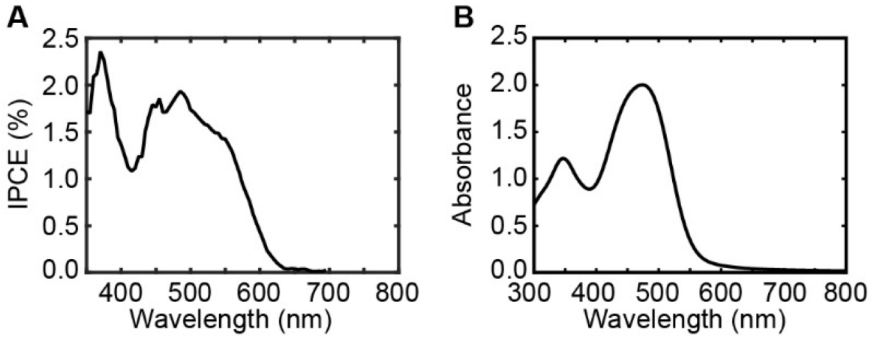

Figure 5.13. (A) Incident photon-to-current efficiency (IPCE) for a $ZnCo_2O_4$ device sensitized with molecular chromophore P1. (B) Absorbance of P1.

5.4 Conclusions

Here, we have presented a solid-state preparation of nanoparticulate $Zn_xCo_{3-x}O_4$ with highly tunable Zn concentration and a pure spinel phase. Tuning the Zn concentration within the spinel lattice improved the electrical properties of the material, significantly increasing the mobility one order of magnitude from ~10^{-5} to ~10^{-4} cm^2·V^{-1}·s^{-1}. The

$Zn_xCo_{3-x}O_4$ nanoparticles were processed into a mesoscopic photocathode, which was characterized in a p-type DSSC configuration. Evaluation of DSSC performance with respect to Zn concentration resulted in the trend of increased performance with increased Zn concentration. Through further optimization, UVO treatments on $ZnCo_2O_4$ photocathodes resulted in a nearly threefold increase in dye-loading from 8.8 to 21 $nmol \cdot cm^{-3}$ and an increase J_{sc} from 0.33 ± 0.04 to 0.47 ± 0.04 $mA \cdot cm^{-2}$. This initial evaluation of $ZnCo_2O_4$ as a mesoporous photocathode demonstrates promise for the further development of this material for solar energy devices.

5.5 Acknowledgements

This work was primarily funded by the UNC Energy Frontier Research Center, and EFRC funded by the U.S. Department of Energy, Office of Science, Office of Basic Energy Sciences, under award DE-SC0001011. S.M.M. acknowledges a National Science Foundation graduate research fellowship.

REFERENCES

(1) O'Regan, B.; Grätzel, M. A Low-Cost, High-Efficiency Solar Cell Based on Dye-Sensitized Colloidal TiO_2 Films. *Nature* **1991**, *353*, 737–740.

(2) Yella, A.; Lee, H. W.; Tsao, H. N.; Yi, C.; Chandiran, A. K.; Nazeeruddin, M. K.; Diau, E. W. G.; Yeh, C. Y.; Zakeeruddin, S. M.; Gratzel, M. Porphyrin-Sensitized Solar Cells with Cobalt (II/III)-Based Redox Electrolyte Exceed 12 Percent Efficiency. *Science (80-.).* **2011**, *334* (6056), 629–634.

(3) Perera, I. R.; Daeneke, T.; Makuta, S.; Yu, Z.; Tachibana, Y.; Mishra, A.; Bäuerle, P.; Ohlin, C. A.; Bach, U.; Spiccia, L. Application of the Tris(acetylacetonato)iron(III)/(II) Redox Couple in P-Type Dye-Sensitized Solar Cells. *Angew. Chemie Int. Ed.* **2015**, *54*, 3758–3761.

(4) Li, Y.; Hasin, P.; Wu, Y. NixCo3-XO4 Nanowire Arrays for Electrocatalytic Oxygen Evolution. *Adv. Mater.* **2010**, *22* (17), 1926–1929.

(5) Yu, M.; Draskovic, T. I.; Wu, Y. Cu(I)-Based Delafossite Compounds as Photocathodes in P-Type Dye-Sensitized Solar Cells. *Phys. Chem. Chem. Phys.* **2014**, *16* (11), 5026–5033.

(6) Ahmed, J.; Blakely, C. K.; Prakash, J.; Bruno, S. R.; Yu, M.; Wu, Y.; Poltavets, V. V. Scalable Synthesis of Delafossite CuAlO2 Nanoparticles for P-Type Dye-Sensitized Solar Cells Applications. *J. Alloys Compd.* **2014**, *591*, 275–279.

(7) Alibabaei, L.; Luo, H.; House, R. L.; Hoertz, P. G.; Lopez, R.; Meyer, T. J. Applications of Metal Oxide Materials in Dye Sensitized Photoelectrosynthesis Cells for Making Solar Fuels: Let the Molecules Do the Work. *J. Mater. Chem. A* **2013**, *1* (13), 4133.

(8) Li, F.; Fan, K.; Xu, B.; Gabrielsson, E.; Daniel, Q.; Li, L.; Sun, L. An Organic Dye-Sensitized Tandem Photoelectrochemical Cell for Light Driven Water Splitting. *J. Am. Chem. Soc.* **2015**, *137*, 9153–9159.

(9) Maeda, K.; Domen, K. Photocatalytic Water Splitting: Recent Progress and Future Challenges. *J. Phys. Chem. Lett.* **2010**, *1* (18), 2655–2661.

(10) Alibabaei, L.; Brennaman, M. K.; Norris, M. R.; Kalanyan, B.; Song, W.; Losego, M. D.; Concepcion, J. J.; Binstead, R. A.; Parsons, G. N.; Meyer, T. J. Solar Water Splitting in a Molecular Photoelectrochemical Cell. *Proc. Nat. Acad. Sci. USA* **2013**, *110*, 20008–20013.

(11) Yu, Z.; Li, F.; Sun, L. Recent Advances in Dye-Sensitized Photoelectrochemical Cells for Solar Hydrogen Production Based on Molecular Components. *Energy Environ. Sci.* **2014**, *8*, 760–775.

(12) Nattestad, A.; Mozer, A. J.; Fischer, M. K. R.; Cheng, Y.; Mishra, A.; Bäuerle, P.; Bach,

U. Highly Efficient Photocathodes for Dye-Sensitized Tandem Solar Cells. *Nat. Mater.* **2009**, *9* (1), 31–35.

(13) Mercado, C. C.; Zakutayev, A.; Zhu, K.; Flynn, C. J.; Cahoon, J. F.; Nozik, A. J. Sensitized Zinc–Cobalt–Oxide Spinel P-Type Photoelectrode. *J. Phys. Chem. C* **2014**, *118* (44), 25340–25349.

(14) Perkins, J. D.; Paudel, T. R.; Zakutayev, A.; Ndione, P. F.; Parilla, P. A.; Young, D. L.; Lany, S.; Ginley, D. S.; Zunger, A.; Perry, N. H.; et al. Inverse Design Approach to Hole Doping in Ternary Oxides: Enhancing P-Type Conductivity in Cobalt Oxide Spinels. *Phys. Rev. B* **2011**, *84*, 1–8.

(15) Zakutayev, A.; Paudel, T. R.; Ndione, P. F.; Perkins, J. D.; Lany, S.; Zunger, A.; Ginley, D. S. Cation off-Stoichiometry Leads to High P-Type Conductivity and Enhanced Transparency in Co 2ZnO 4 and Co 2NiO 4 Thin Films. *Phys. Rev. B* **2012**, *85* (8), 1–8.

(16) Kim, T. W.; Woo, M. A.; Regis, M.; Choi, K. S. Electrochemical Synthesis of Spinel Type ZnCo2O4 Electrodes for Use as Oxygen Evolution Reaction Catalysts. *J. Phys. Chem. Lett.* **2014**, *5* (13), 2370–2374.

(17) Luo, W.; Hu, X.; Sun, Y.; Huang, Y. Electrospun Porous ZnCo2O4 Nanotubes as a High-Performance Anode Material for Lithium-Ion Batteries. *J. Mater. Chem.* **2012**, *22* (18), 8916.

(18) Wang, W.; Yang, Y.; Yang, S.; Guo, Z.; Feng, C.; Tang, X. Synthesis and Electrochemical Performance of ZnCo2O4 for Lithium-Ion Battery Application. *Electrochim. Acta* **2015**, *155*, 297–304.

(19) Wu, R.; Qian, X.; Zhou, K.; Wei, J.; Lou, J.; Ajayan, P. M. Porous Spinel Zn(x)Co(3-x)O(4) Hollow Polyhedra Templated for High-Rate Lithium-Ion Batteries. *ACS Nano* **2014**, *8* (6), 6297–6303.

(20) Ren, Z.; Botu, V.; Wang, S.; Meng, Y.; Song, W.; Guo, Y.; Ramprasad, R.; Suib, S. L.; Gao, P.-X. Monolithically Integrated Spinel M(x)Co(3-x)O(4) (M=Co, Ni, Zn) Nanoarray Catalysts: Scalable Synthesis and Cation Manipulation for Tunable Low-Temperature CH(4) and CO Oxidation. *Angew. Chem. Int. Ed. Engl.* **2014**, *53* (28), 7223–7227.

(21) Liu, B.; Zhang, J.; Wang, X.; Chen, G.; Chen, D.; Zhou, C.; Shen, G. Hierarchical Three-Dimensional $ZnCo_2O_4$ Nanowire Arrays/carbon Cloth Anodes for a Novel Class of High-Performance Flexible Lithium-Ion Batteries. *Nano Lett.* **2012**, *12* (6), 3005–3011.

(22) Yan, L.; Ren, T.; Wang, X.; Gao, Q.; Ji, D.; Suo, J. Excellent Catalytic Performance of ZnxCo1−xCo2O4 Spinel Catalysts for the Decomposition of Nitrous Oxide. *Catal. Commun.* **2003**, *4* (10), 505–509.

(23) Flynn, C. J.; Oh, E. E.; McCullough, S. M.; Call, R. W.; Donley, C. L.; Lopez, R.; Cahoon, J. F. Hierarchically-Structured NiO Nanoplatelets as Mesoscale P-Type Photocathodes for Dye-Sensitized Solar Cells. *J. Phys. Chem. C* **2014**, *118* (26), 14177–

14184.

(24) Qin, P.; Zhu, H.; Edvinsson, T.; Boschloo, G.; Hagfeldt, A.; Sun, L. Design of an Organic Chromophore for P-Type Dye-Sensitized Solar Cells. *J. Am. Chem. Soc.* **2008**, *130* (27), 8570–8571.

(25) Tsuzuki, T.; McCormick, P. Mechanochemical Synthesis of Nanoparticles. *J. Mater. Sci.* **2004**, *9*, 5143–5146.

(26) Šepelák, V.; Düvel, A.; Wilkening, M.; Becker, K. D.; Heitjans, P. Mechanochemical Reactions and Syntheses of Oxides. *Chem. Soc. Rev.* **2013**, *42* (18), 7507–7520.

(27) *CRC Handbook for Chemistry and Physics*, 96th ed.; Haynes, W. M., Ed.

(28) Ito, S.; Murakami, T. N.; Comte, P.; Liska, P.; Grätzel, C.; Nazeeruddin, M. K.; Grätzel, M. Fabrication of Thin Film Dye Sensitized Solar Cells with Solar to Electric Power Conversion Efficiency over 10%. *Thin Solid Films* **2008**, *516* (14), 4613–4619.

(29) Zakutayev, A.; Perkins, J. D.; Parilla, P. A.; Widjonarko, N. E.; Sigdel, A. K.; Berry, J. J.; Ginley, D. S. Zn–Ni–Co–O Wide-Band-Gap P-Type Conductive Oxides with High Work Functions. *MRS Commun.* **2011**, *1* (1), 23–26.

(30) Skoog, D.; Holler, J.; Crouch, S. *Principles of Intrumental Analysis*, 6th ed.; Brooks/Cole: Belmont, CA, 2007.

(31) Ndione, P. F.; Shi, Y.; Stevanovic, V.; Lany, S.; Zakutayev, A.; Parilla, P. A.; Perkins, J. D.; Berry, J. J.; Ginley, D. S.; Toney, M. F. Control of the Electrical Properties in Spinel Oxides by Manipulating the Cation Disorder. *Adv. Funct. Mater.* **2014**, *24* (5), 610–618.

(32) Chougule, M. A.; Pawar, S. G.; Godse, P. R.; Sakhare, R. D.; Sen, S.; Patil, V. B. Sol–gel Derived Co3O4 Thin Films: Effect of Annealing on Structural, Morphological and Optoelectronic Properties. *J. Mater. Sci. Mater. Electron.* **2012**, *23* (3), 772–778.

(33) Kim, Y.; Lee, J. H.; Cho, S.; Kwon, Y.; In, I.; Lee, J.; You, N. H.; Reichmanis, E.; Ko, H.; Lee, K. T.; et al. Additive-Free Hollow-Structured Co3O4 Nanoparticle Li-Ion Battery: The Origins of Irreversible Capacity Loss. *ACS Nano* **2014**, *8* (7), 6701–6712.

(34) Pérez León, C.; Kador, L.; Peng, B.; Thelakkat, M. Characterization of the Adsorption of Ru-Bpy Dyes on Mesoporous TiO 2 Films with UV-Vis, Raman, and FTIR Spectroscopies. *J. Phys. Chem. B* **2006**, *110* (17), 8723–8730.

(35) Dell'Orto, E.; Raimondo, L.; Sassella, A.; Abbotto, A. Dye-Sensitized Solar Cells: Spectroscopic Evaluation of Dye Loading on TiO_2. *J. Mater. Chem.* **2012**, *22* (22), 11364.

(36) Atkins, P. W.; de Paula, J. *Physical Chemistry*, 8th ed.; 2006.

(37) Nazeeruddin, M. K.; Baranoff, E.; Grätzel, M. Dye-Sensitized Solar Cells: A Brief Overview. *Sol. Energy* **2011**, *85* (6), 1172–1178.

(38) Dearden, C. A.; Walker, M.; Beaumont, N.; Hancox, I.; Unsworth, N. K.; Sullivan, P.; McConville, C. F.; Jones, T. S. High Voltage Hybrid Organic Photovoltaics Using a Zinc Oxide Acceptor and a Subphthalocyanine Donor. *Phys. Chem. Chem. Phys.* **2014**, *16* (35), 18926–18932.

(39) Zhu, J.; Gao, Q. Mesoporous MCo2O4 (M = Cu, Mn and Ni) Spinels: Structural Replication, Characterization and Catalytic Application in CO Oxidation. *Microporous Mesoporous Mater.* **2009**, *124* (1–3), 144–152.

Chapter 6: CuO functionalized transparent nanoparticles: A hole transport layer with applications in solar energy conversion

To be submitted by S. M. McCullough, T. Moot, T. S. Teitsworth, and J. F. Cahoon

6.1 Introduction:

Solar energy conversion continues to be an active area of research with particular focus on the long-run goal of artificial photosynthesis.[1–5] A dye-sensitized photoelectrosynthetic cell (DSPEC), or artificial leaf, is a target device architecture for a solar-to-fuel device. Solar-to-fuel approaches obviate some challenges solar-to-electric devices face by storing the absorbed light energy as a stable chemical bond in a storable molecular fuel. An additional benefit of a DSPEC design is that CO_2, an air pollutant of interest, would be sequestered and contained within a closed fuel cell system where the same constituents can be repeatedly reduced in the DSPEC and oxidized in a fuel cell feasibly ad infinitum.[1]

In order for a DSPEC to be most effective, two photoactive electrodes must work synergistically in tandem. A tandem cell can, in principle, provide an increase in photovoltage sufficient to drive target catalytic processes such as water splitting. An additional advantage of using a tandem or Z-scheme design is complementary light absorbance with the photoanode half-cell absorbing the blue wavelengths and the photocathode half-cell absorbing the red wavelengths. By implementing two photoactive electrodes, we can more precisely design chromophores for each electrode to absorb the available solar spectrum more completely and use otherwise foregone lower energy photons advantageously.[6,7]

A primary challenge facing the realization of a high-efficiency tandem design is mismatched photocurrent, where the photoanode's photocurrent significantly outpaces that of the photocathode. To develop the electrodes' materials capabilities separately, the DSPEC design is split into two half cells with a dye-sensitized solar cell (DSSC) architecture. Presently, the power conversion efficiencies of n-type DSSCs significantly exceeds those of p-type DSSCs with record efficiencies of 14% and 2.5% respectively.[8,9]

High charge recombination rates have primarily limited performance of NiO based p-type DSSCs due to large concentrations of defects throughout the electrode material.[10–12] Metal oxide semiconductors such as TiO_2 and NiO depend on native defects, usually in the form of vacancies, to act as the electronic dopant. Conveniently, TiO_2 features a native doping level on the order of 10^{18} cm^{-3} which is sufficiently high for conductivity but low enough to suppress excessive recombination. Inconveniently, NiO's native doping level is on the order of 10^{20} cm^{-3} which introduces an exceedingly high concentration of defects and debilitating recombination which also gives rise to the black color of the nominally wide bandgap material.[13,14] Despite attempts to passivate and control defect density in NiO, the material continues to lag behind in performance compared to TiO_2.[12,15–17] Despite various attractive qualities, the high density of native defects in NiO continue to sabotage the material's viability as a hole transport layer, and, consequently, the demand for a high-performance hole transport material for mesoporous photocathodes has still not been met.

When considering alternatives to NiO, several wide bandgap p-type materials including copper delafossites, cobalt spinels, and lead titanate have emerged as candidates, and yet none have outperformed NiO DSSCs.[18–25] Consequently, the search for an improved photocathode material continues. Despite over 25 years of research on DSSCs, some of the fundamental

processes in DSSCs operation are not fully understood on a microscopic scale, although preliminary modeling has been developed by several investigators.[26–29] In this report, we introduce a novel electrode material, TiCuO, that consists of ~2 nm copper(II) oxide nanoparticles bound to the surface of ~20 nm TiO_2 nanoparticles. Although TiO_2 is often described as a chemically inert material, we use the surface defects to nucleate the CuO nanoparticles on the surface. The use of TiO_2 as a scaffold and support for various nanoparticles materials has been demonstrated for catalytic applications, although this is the first report of CuO.[30–32] In general, chemically modified TiO_2 nanoparticles for solar energy conversion applications have resulted in a diverse library of materials.[33–43] All of these previously reported materials continue to use the modified TiO_2 as an improved electron transport layer. The use of an insulator such as Al_2O_3 for the mesoporous electrode in a DSSC has not been reported previously. Here, we report CuO functionalized TiO_2 (TiCuO) and CuO functionalized Al_2O_3 (AlCuO) to fulfill the role of a hole transport layer in a p-DSSC.

6.2 Experimental Materials and Methods

6.2.a Materials and Reagents

All materials were used as received. TiO_2 aeroxide nanoparticles (20 nm) were purchased from Acros Organics. Copper(II) oxide nanoparticles were purchased from US Research Nanomaterials, Inc. (40 nm). Aluminum oxide nanoparticles 20% wt in isopropanol were purchased from (<50 nm) Sigma Aldrich. Copper(II) nitrate trihydrate (purum), ethyl cellulose (300 cP), anhydrous α-terpineol, absolute ethanol, iodine (99.99%), and lithium iodide (99.9%) were purchased from Sigma Aldrich. FTO glass was purchased from Hartford glass. 25 μm Surlyn polymer was purchased from Solaronix.

6.2.b. TiCuO nanoparticle synthesis

TiCuO was synthesized using purchased TiO_2 nanoparticles as a precursor and an aqueous solution of $Cu(NO_3)_2$ in a non-stirred pressure vessel with a teflon sleeve held at 80 °C for one week. Additional syntheses were performed under identical conditions except at 120 °C and 150 °C. The vessel was left to cool to ambient temperature naturally. The collected powder was rinsed with water and dried at 40 °C.

6.2.c. AlCuO nanoparticle synthesis

AlCuO was prepared at 80 °C identically to TiCuO except Al_2O_3 nanoparticles were used in place of TiO_2.

6.2.d Mesoporous thin film preparation

Each metal oxide powder was prepared as thin film electrodes using a spin coating paste with synthetic details previously described.[14] Films were calcined at 600 °C for 45 minutes, and the calcined films were subsequently dye-loaded when required using a 0.1 mM P1 solution in acetonitrile.

6.2.e Analytical Methods

Powder x-ray diffraction (PXRD) patterns were collected using a Rigaku Multiflex diffractometer with a scan rate of 2°/minute. Ultraviolet-visible spectroscopy was performed on an Agilent Cary 5000 UV-Vis-NIR spectrophotometer using the integrating sphere attachment. X-ray photoelectron spectroscopy (XPS) was performed on Kratos Axis Ultra DLD x-ray photoelectron spectrometer. Electrochemical analysis was performed in a three electrode cell using $TBAClO_4$ in acetonitrile as the supporting electrolyte, Ag/AgCl as the reference electrode, Pt as

the counter electrode, the metal oxide of interest on FTO as the working electrode and a CH Instruments 604E potentiostat. Conductance measurements were performed on a CH Insturments 760E bipotentiostat using a Pt interdigitated array (IDA) electrode, Pt counter electrode, Ag/AgCl reference electrode and $TBAClO_4$ in acetonitrile as the supporting electrolyte. The IDA electrode was purchased from CH Instruments. The conductance measurement used an applied bias of 5 mV between the two working electrodes and a scan rate of 0.02 V/s. Transmission electron microscopy (TEM) including high-angle annular dark field (HAADF) and energy dispersive x-ray spectroscopy (EDS) was performed on a . Electrochemical impedance spectroscopy (EIS) was performed on a Gamry Reference 600 electrochemical impedance spectrometer in a two electrode configuration using the Pt electrode as both counter and the reference electrodes.

6.2.f. DSSC assembly and testing

Dye-sensitized solar cells were fabricated using previously reported methods.[14] The electrolyte used was a LiI/I_2 solution in water. Device measurements were taken on a Keithley 2636A SourceMeter under AM1.5G solar simulation.

6.2.g Microelectrode fabrication for resistance measurements

The gold microelectrode pattern used for the resistance measurements was fabricated on a silicon nitride wafer. An MMA/PMMA (MMA EL9, PMMA A2, Microchem) resist stack was spin-coated onto the wafer and the electrode pattern defined via electron beam lithography (JC Nabity Lithography Systems). Metal (3nm chromium, 100nm gold) was deposited onto the pattern electron beam evaporation (Thermionics VE-100). The desired metal oxide film was spincast and annealed on top of the gold microelectrode patterns. Measurements were taken with a Keithley 2636A SourceMeter and Signatone micromanipulators (S725) with probe tips (SE-TL)

6.3 Results and Discussion

By introducing a ultrasmall nanoparticles on the surface of transparent nanoparticles, in this case TiO_2, sufficient p-type character is introduced such that when processed into p-DSSCs, the behavior of the device in the dark switches compared to the n-type TiO_2 devices. As shown in Figure 6.1, the CuO decorated nanoparticles featured low charge transfer resistance when a positive bias was applied to the working electrode in both acetonitrile based electrolytes (Figure 6.1A) and water based electrolytes (Figure 6.1B). TiO_2, the current champion n-type material for DSSCs, produces the opposite result of high charge transfer resistance when positive bias was applied to the working electrode in the acetonitrile based electrolyte as is expected for a TiO_2 DSSC sensitized with P1. When the CuO is deposited on the TiO_2 scaffold, the behavior switches

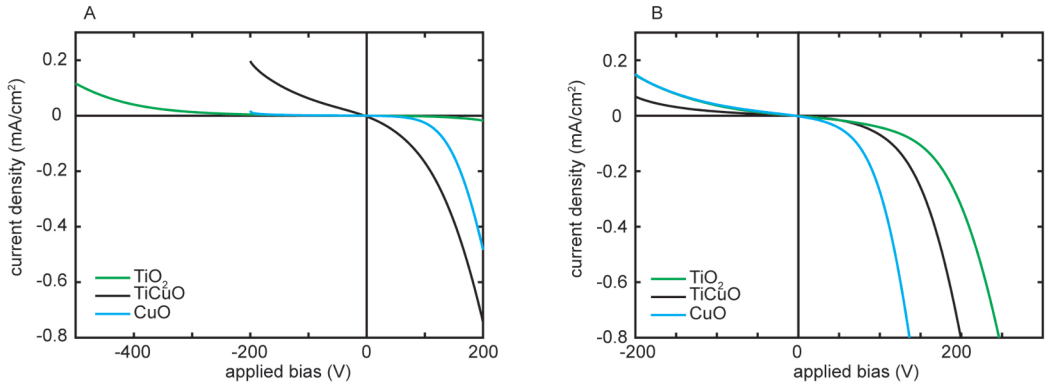

Figure 6.1. Device performance for TiO_2, TiCuO, and CuO in the dark. Dashed lines denote *J-V* scans in the light and solid curves denote *J-V* scans in the dark. (A) TiO_2, TiCuO, and CuO DSSCs using an acetonitrile based I^-/I_3^- electrolyte. (B) TiO_2, TiCuO, and CuO DSSCs using an aqueous based I^-/I_3^- electrolyte.

to more closely match the p-type CuO DSSC. The charge transfer trends were also observed in electrochemical impedance spectroscopy where the charge transfer resistance increased as the applied bias increased for TiCuO and the opposite trend was observed for TiO_2. Figure 6.2A plots the charge transfer resistances extracted from a double-Randles fit for TiCuO and TiO_2 for a

variety of applied biases. A representative Bode plot with the fitted circuit is included in Figure 6.2B.

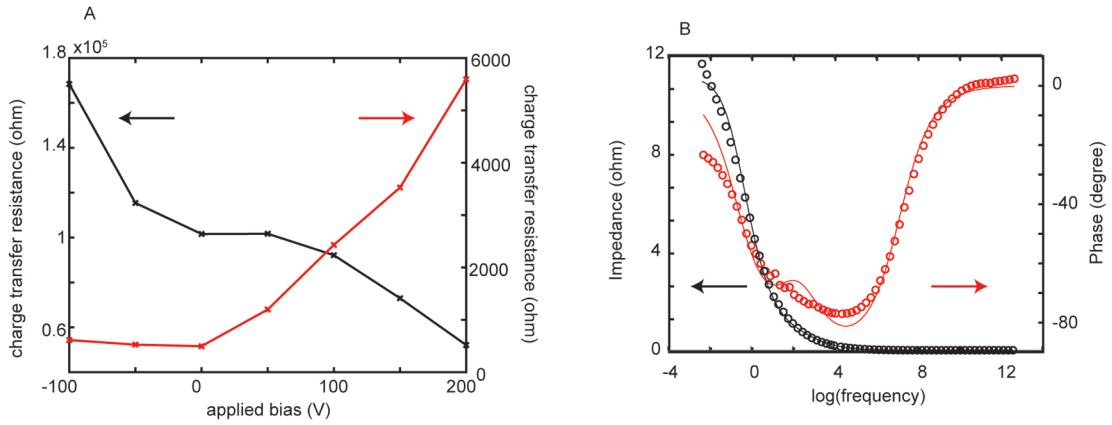

Figure 6.2. EIS results for TiCuO and TiO_2. (A) Charge transfer resistances extracted from a double Randles fit for TiCuO in black and TiO_2 in red. (B) Representative Bode plot for TiCuO at 0 V applied bias. The circles are collected data and the line represents the fit.

The synthesis of the TiCuO nanoparticles employed the most reactive sites on the defective TiO_2 nanoparticles' surface. The surface of TiO_2 provides a location for the CuO to nucleate. The exact morphology of the TiCuO product is shown in Figure 6.3A with HAADF imaging and elemental EDS maps (Figure 6.3B-6.3D), and the morphology and elemental EDS maps of AlCuO is shown in Figure 6.4A-D. We observe that only the mildest reaction conditions yield a product where enough CuO is deposited on the larger nanoparticulate scaffold to be useful for hole conduction, but not so much material is deposited that the sample is overwhelmed by pure-phase CuO. Elevated reaction temperatures of 120 °C and 150 °C resulted in the growth of select nucleated CuO particles into long rods which ultimately overwhelmed the TiO_2 particles. Despite mild reaction conditions of 80 °C, we do observe a minimal number of CuO particles reaching up to 20 nm in diameter in the TiCuO sample. In terms of CuO surface density, we estimate between 20-30 CuO nanoparticles per TiO_2 particle in TiCuO and between 25-35 CuO particles per Al_2O_3

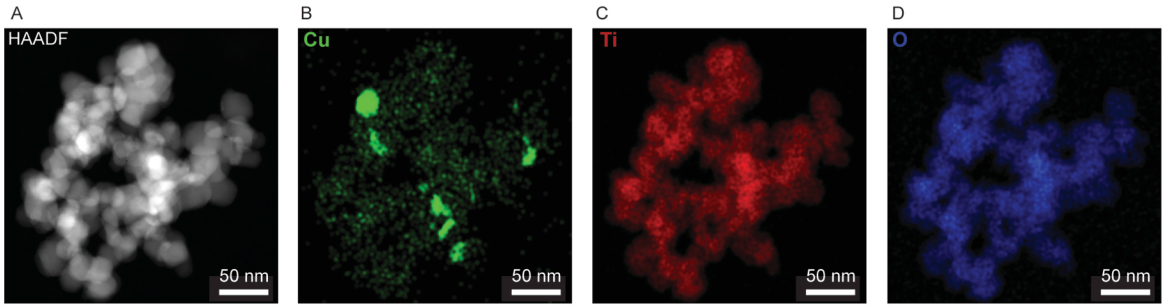

Figure 6.3. TiCuO Morphology. A: HAADF image of TiCuO nanoparticles. B: Cu EDS elemental map. C: Ti EDS elemental map. D: O EDS elemental map. ~2 nm CuO particles are detected throughout the material with some incidents of pure phase CuO particles as large as 20 nm in diameter.

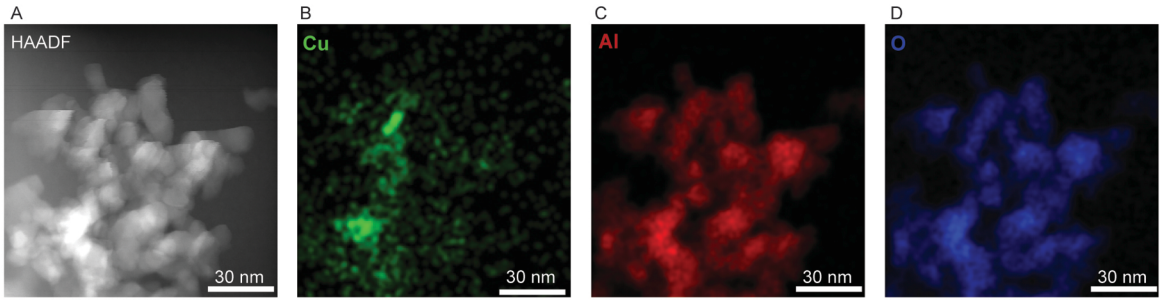

Figure 6.4. AlCuO Morphology. A: HAADF image of AlCuO nanoparticles. B: Cu EDS elemental map. C: Ti EDS elemental map. D: O EDS elemental map. Analogously to TiCuO, ~2 nm CuO particles are detected throughout the material with some incidents of pure phase CuO particles as large as 20 nm in diameter in the AlCuO material.

particle in AlCuO. Figure 6.5 includes EDS elemental maps and HAADF images of the high temperature TiCuO synthetic products. Atomic concentrations in TiCuO samples acquired via EDS for Cu were measured at 1.3%, 13.0%, 25.8% for 80 °C, 120 °C, and 150 °C reaction temperatures respectively. Because of the desirable concentration and size of CuO nanoparticles bound to the TiO_2 scaffold with the 80 °C preparation, all subsequent analysis is done on either the TiCuO or AlCuO nanoparticles both synthesized at 80 °C unless otherwise noted.

The TiCuO and AlCuO nanoparticles were characterized by UV-Vis spectroscopy which indicated high transparency within the visible range. The CuO particles on the TiO_2 or Al_2O_3 particles are sufficiently small in size that they introduce minimal competitive absorbance with the chromophore despite CuO having a small band gap of 1.7 eV, which would typically preclude it from being used as a DSSC electrode material. By employing the ultrasmall nanoparticles, we can still use the advantageously situated valence band edge of CuO and also circumvent the competitive optical absorbance. TiCuO films maintain the high surface area of the TiO_2

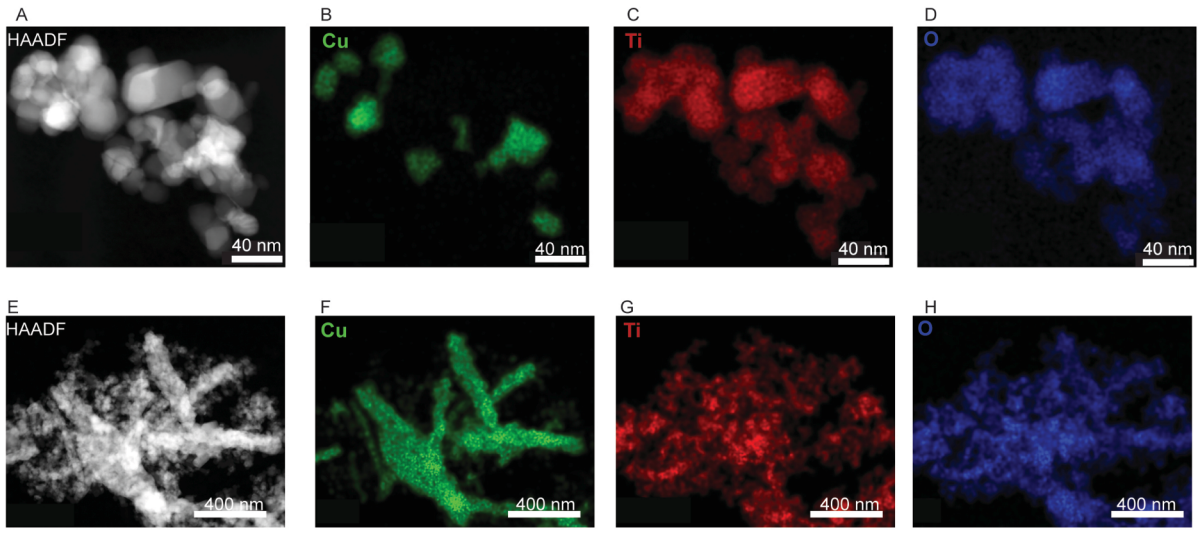

Figure 6.5. TiCuO morphology synthesized at elevated temperature. HAADF with EDS mapping of TiCuO prepped at 120 °C (A-D) and 150 °C (E-H). Larger crystal grains of CuO grown in at higher synthetic temperatures. Eventually, given enough time and heat, the CuO particles grow into large rods (F) ultimately overwhelming the TiO_2 starting material.

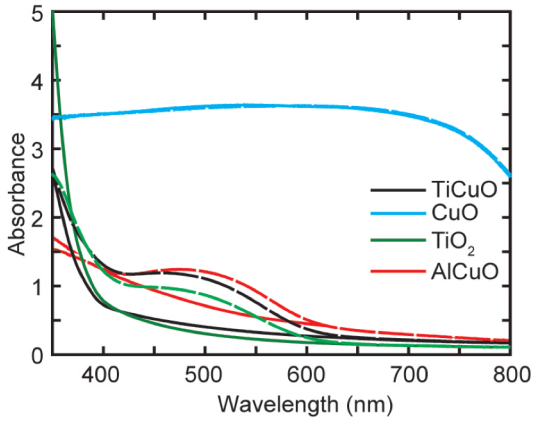

Figure 6.6. UV-Vis spectroscopy of TiCuO, CuO, TiO_2, and AlCuO with and without P1 dye loaded on the surface. The solid lines represent the films without dye and the dashed lines represent the dye loaded films.

nanoparticles scaffold resulting in a high dye loading of P1. Similar dye-loading results were observed for AlCuO. UV-Vis absorbance traces of all films before and after dye-loading are shown in Figure 6.6.

Additional chemical characterization included powder x-ray diffraction (Figure 6.7). Patterns indicate that the anatase peaks from the TiO_2 nanoparticle starting material are maintained and no additional diffraction peaks were detected from the introduction of the CuO phase from the powder tested as synthesized or from a post-synthesis 600 °C annealed powder. XPS analysis was performed on the TiCuO nanoparticlate film (Figure 6.8) and the spectrum included signals for Ti, Cu, and O as expected. The Ti 2p peaks at 464 eV and 458 eV were consistent with Ti(IV) as expected for the anatase phase, and the Cu peaks at 952 eV and 932 eV are consistent with Cu(II). The XPS spectrum indicates no evidence of either Ti^0 or Cu^0 metallic impurities. XPS data could not be collected on AlCuO because of Al_2O_3 is an insulator and the material charged precluding analysis.

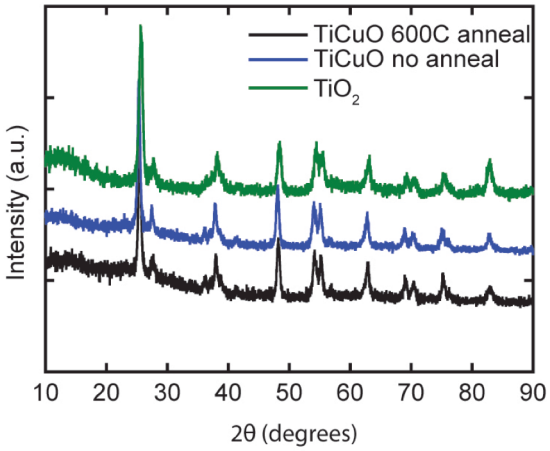

Figure 6.7. PXRD data of TiO_2 nanoparticles, TiCuO nanoparticles as synthesized, and TiCuO nanoparticles with at 600 °C post anneal.

To determine the suitability of TiCuO and AlCuO for use as photocathodes, electrochemical characterization of the mesoporous nanoparticle films must be done to probe where electrochemically active states are available. By calculating the density of states (DOS) from cyclic voltammetry capacitive curves, we can determine the relative changes in position and quantity for states present in TiCuO compared to the pure phases of TiO_2 and CuO. We observe that the DOS available in the TiCuO material falls in between the states present for CuO and TiO_2 (Fig 6.9A) The onset of states for CuO occurs at -0.5 vs. Ag/AgCl, whereas the exponential increase in DOS at the valence band edge of CuO ($E_{VB,CuO}$) is at ~0.5 V vs Ag/AgCl, similar to literature reports of 0.70 vs. Ag/AgCl. The large density of states above the band in CuO can be attributed to a significant defect density which is also present in other p-type metal oxides.[12] Notably, the onset of DOS for TiCuO occurs at 0.75 V vs. Ag/AgCl, which is consistent with the $E_{VB,CuO}$. The valence band edge of TiO_2 is too negative with respect to vacuum at -7.3 eV and is outside of the solvent electrochemical window.

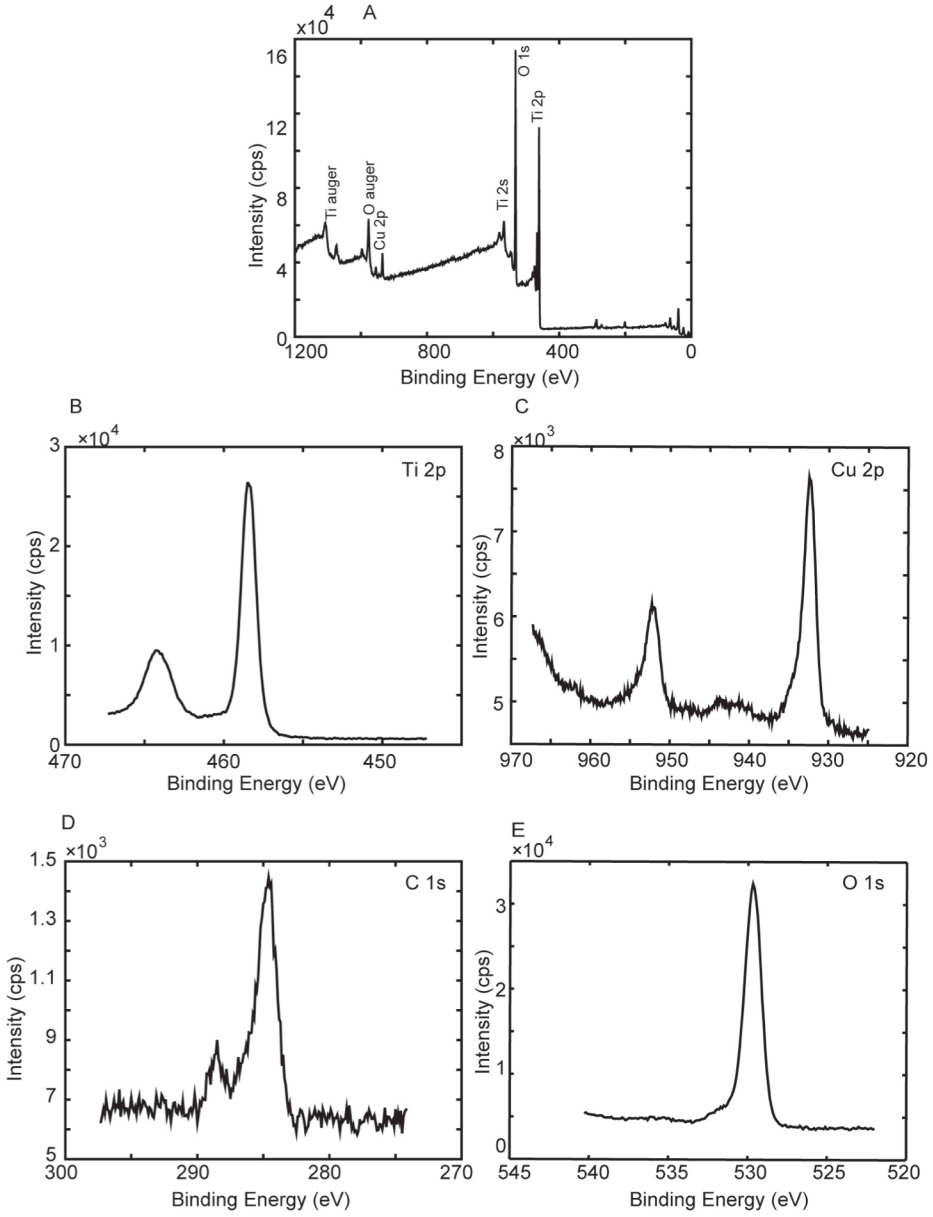

Figure 6.8. XPS analysis for TiCuO. (A) Full scan for TiCuO. (B-E) High resolution XPS data for TiCuO synthesized at 80 °C.

The data suggests that DOS from TiCuO are contributed from the CuO nanoparticles within the range required for P1 injection. We argue that the DOS present in TiCuO is advantageous for a p-DSSC because of the position of the I^-/I_3^- Nernst potential gives a large theoretical V_{OC} of 550 mV while also having efficient injection for the P1 chromophore. Additionally, we note that the

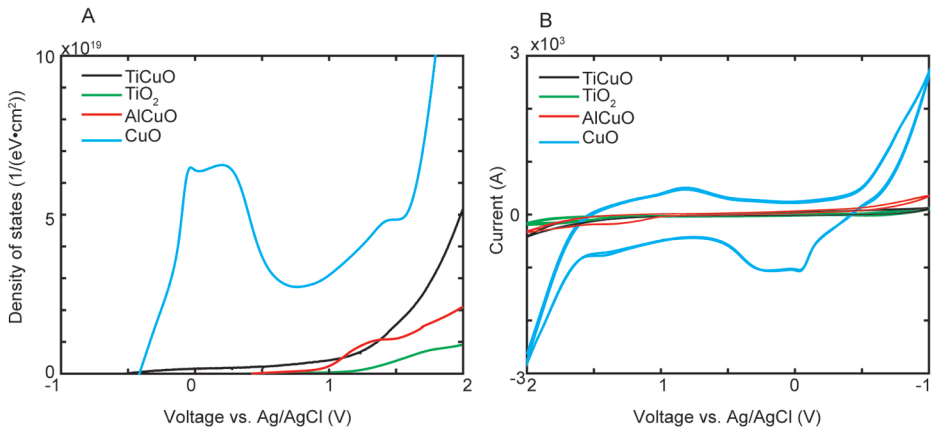

Figure 6.9. Density of states (A) and cyclic voltammograms (B) of TiCuO, TiO_2, AlCuO, and CuO.

excited state oxidative potential of the chromophore P1 is at -5.88 eV vs. vacuum and cannot injection into at TiO_2 valence band at -7.3 eV vs. vacuum. Cyclic voltammograms used to calculate DOS are shown in Figure 6.9B.

Additionally, the film's resistance was measured across different distances on a gold microelectrode pattern (Figure 6.10A). A linear fit of the resistance and the known film thickness were used to calculate a film conductivity of 3.85×10^{-8} S/cm (Figure 6.10B). However, this measurement with the electrode in air does not fully describe the behavior in a DSSC configuration

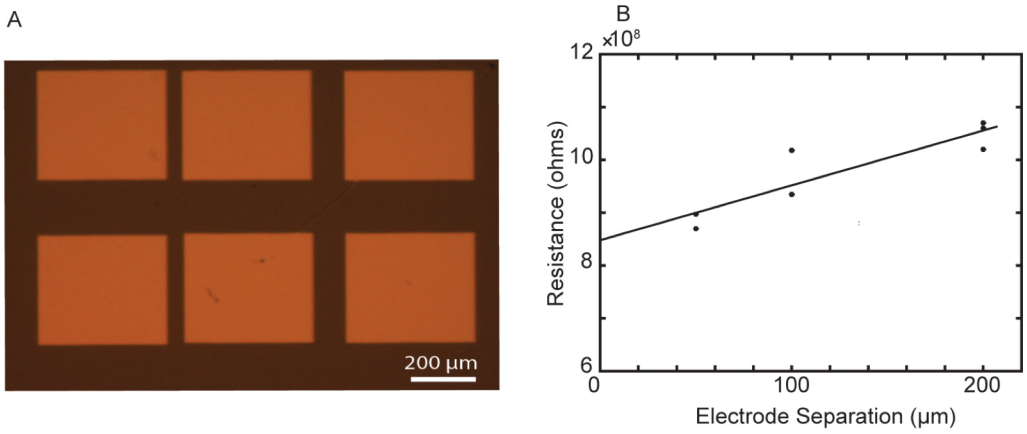

Figure 6.10. Conductivity measurements of TiCuO. (A) Au microelectrode pattern (B) Resistance measurements from Au microelectrode patterns.

because of the influence of the electrochemical environment and the influence of the electrolyte on the charge conduction of the electrode. Using an interdigitated array (IDA) Pt electrode, we measured conductance (Figure 6.11) across a wide electrochemical window and observed that conductance states begin to grow in at -0.23 V vs. Ag/AgCl which is similar to the density of states

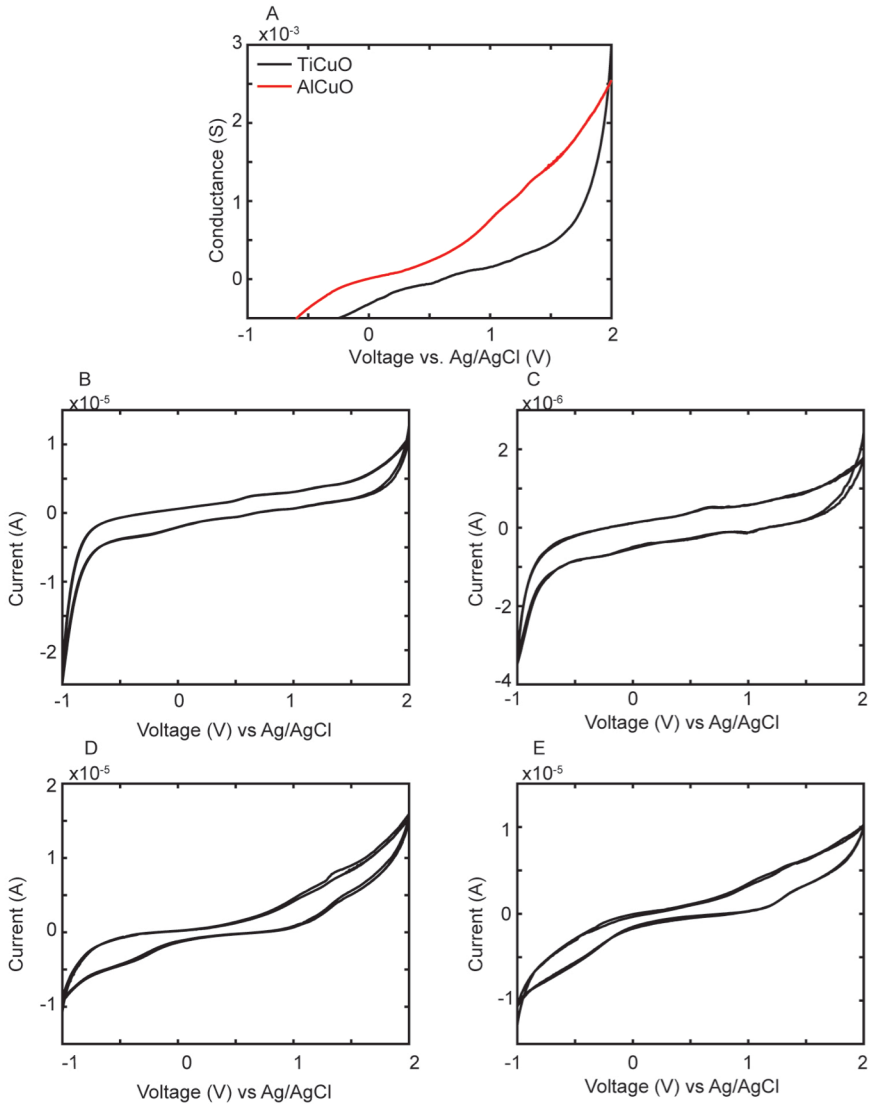

Figure 6.11. IDA measurements on TiCuO and AlCuO. (A) Conductance calculated from the IDA electrode measurements. (B) CV for working electrode 1 for TiCuO. (C) CV for working electrode 2 for TiCuO. (C) CV for working electrode 1 for AlCuO. (D) CV for working electrode 2 for AlCuO.

observed in Figure 6.9A for pure phase CuO indicating that conducting states in TiCuO are contributed from the CuO particles.

Finally, DSSC performance was tested to vet the TiCuO and AlCuO materials as a hole transport layers. The four different materials were used as the working electrodes, TiO_2, TiCuO, CuO, and AlCuO. DSSCs with pure TiO_2 do not feature any significant cathodic or anodic photocurrent from the TiO_2 device as would be expected for this architecture and aqueous electrolyte system. Pure CuO p-DSSCs produced the same average photocurrent to the TiCuO devices at 0.12 ± 0.04 mA/cm^2. The photovoltage for the TiCuO devices was significantly larger at 122 ± 3 mV versus 69 ± 13 mV measured for the CuO devices. Full statistics can be found in Table 6.1 for the acetonitrile electrolyte and Table 6.2 for the aqueous electrolyte, and champion curves are plotted for the aqueous electrolyte in Figure 6.12. The limited photocurrent could feasibly be a result of some adverse electron injection into the TiO_2 core. No anodic photocurrent for the pure-phase TiO_2 in observed in the aqueous devices because the recombination from the I_2 acting as an efficient electron scavenger in the electrolyte. Ultrafast dynamics will be employed in

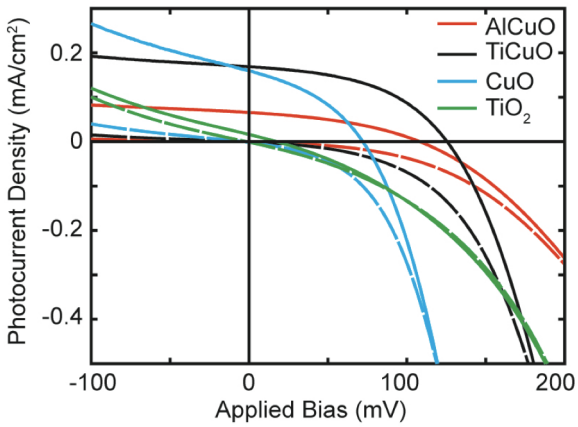

Figure 6.12. Champion *J-V* curves for AlCuO, TiCuO, CuO, and TiO_2 sensitized with P1 in an aqueous electrolyte.

future work to establish if electron injection into TiO_2 states is occurring in addition to hole injection into CuO states.

Table 6.1. *J-V* metrics for AlCuO, CuO, TiCuO, TiO_2 in an acetonitrile electrolyte.

Electrode material	J_{SC} (mA/cm_2)	V_{OC} (mV)	FF (%)	PCE (%)
AlCuO	0.008 ± 0.012	24 ± 82	29 ± 1	1.7± 1.7
CuO	0.045± 0.007	80 ± 14	37 ± 4	13± 4.1
TiCuO	0.11 ± 0.06	57 ± 3.8	26 ± 8	24 ± 2
TiO_2	-0.11 ± 0.03	241 ± 11	28 ± 1	78 ± 5

Table 6.2. *J-V* metrics for AlCuO, CuO, TiCuO, TiO_2 in an aqueous electrolyte.

Electrode material	J_{SC} (mA/cm^2)	V_{OC} (mV)	FF (%)	PCE x 10^{-4}(%)
AlCuO	0.064 ± 0.014	100. ± 10.	35 ± 2	22± 6.4
CuO	0.12± 0.04	69 ± 14	37 ± 4	29± 10
TiCuO	0.12 ± 0.04	122 ± 3	37 ± 11	58 ± 30
TiO_2	0.009 ± 0.008	18 ± 18	21 ± 9	0.7 ± 0.8

6.4 Conclusions

If we want to be able to design a better photocathode material, we need to attack the problem from a fundamentally different approach and leverage the design of a DSSC advantageously. By designing a material with such a small concentration of the p-type material, CuO, present only on the electrode's surface, we can use the material's appropriately positioned valence band edge and circumvent some of the disadvantageous properties such as the competitive absorbance caused by the 1.7 eV bandgap. We have presented both the functionalization of TiO_2 and Al_2O_3 nanoparticles, and future work will extend to other appropriate scaffolds and feasibly other semiconducting materials of interest.

6.5 Acknowledgements

This work was primarily funded by the UNC Energy Frontier Research Center, and EFRC funded by the U.S. Department of Energy, Office of Science, Office of Basic Energy Sciences, under award DE-SC0001011. Thank you to Aaron Taggart and Kyle Brennaman for assistance with the IDA measurements. Thank you to James McBride for TEM imaging. Thank you to Carrie Donley for XPS measurements.

REFERENCES

(1) Brennaman, M. K.; Dillon, R. J.; Alibabaei, L.; Gish, M. K.; Dares, C. J.; Ashford, D. L.; House, R. L.; Meyer, G. J.; Papanikolas, J. M.; Meyer, T. J. Finding the Way to Solar Fuels with Dye-Sensitized Photoelectrosynthesis Cells. *J. Am. Chem. Soc.* **2016**, *138* (40), 13085–13102.

(2) Yu, Z.; Li, F.; Sun, L. Recent Advances in Dye-Sensitized Photoelectrochemical Cells for Solar Hydrogen Production Based on Molecular Components. *Energy Environ. Sci.* **2014**, *8*, 760–775.

(3) Montoya, J. H.; Seitz, L. C.; Chakthranont, P.; Vojvodic, A.; Jaramillo, T. F.; Nørskov, J. K. Materials for Solar Fuels and Chemicals. *Nat. Mater.* **2016**, *16* (1), 70–81.

(4) Tuller, H. L. Solar to Fuels Conversion Technologies: A Perspective. *Mater. Renew. Sustain. Energy* **2017**, *6* (1), 3.

(5) Nocera, D. G. Solar Fuels and Solar Chemicals Industry. *Acc. Chem. Res.* **2017**, *50* (3), 616–619.

(6) Sherman, B. D.; Bergkamp, J. J.; Brown, C. L.; Moore, A. L.; Gust, D.; Moore, T. A. A Tandem Dye-Sensitized Photoelectrochemical Cell for Light Driven Hydrogen Production. *Energy Environ. Sci.* **2016**, *9* (5), 1812–1817.

(7) Alibabaei, L.; Luo, H.; House, R. L.; Hoertz, P. G.; Lopez, R.; Meyer, T. J. Applications of Metal Oxide Materials in Dye Sensitized Photoelectrosynthesis Cells for Making Solar Fuels: Let the Molecules Do the Work. *J. Mater. Chem. A* **2013**, *1* (13), 4133.

(8) Perera, I. R.; Daeneke, T.; Makuta, S.; Yu, Z.; Tachibana, Y.; Mishra, A.; Bäuerle, P.; Ohlin, C. A. A.; Bach, U.; Spiccia, L.; et al. Application of the tris(acetylacetonato)iron(III)/(II) Redox Couple in P-Type Dye-Sensitized Solar Cells. *Angew. Chemie - Int. Ed.* **2015**, *54* (12), 3758–3762.

(9) Kakiage, K.; Aoyama, Y.; Yano, T.; Oya, K.; Fujisawa, J.; Hanaya, M. Highly-Efficient Dye-Sensitized Solar Cells with Collaborative Sensitization by Silyl-Anchor and Carboxy-Anchor Dyes. *Chem. Commun.* **2015**, *51* (88), 15894–15897.

(10) Daeneke, T.; Yu, Z.; Lee, G. P.; Fu, D.; Duffy, N. W.; Makuta, S.; Tachibana, Y.; Spiccia, L.; Mishra, A.; B??uerle, P.; et al. Dominating Energy Losses in NiO P-Type Dye-Sensitized Solar Cells. *Adv. Energy Mater.* **2015**, *5* (4).

(11) D'Amario, L.; Antila, L. J.; Pettersson Rimgard, B.; Boschloo, G.; Hammarström, L. Kinetic Evidence of Two Pathways for Charge Recombination in NiO-Based Dye-Sensitized Solar Cells. *J. Phys. Chem. Lett.* **2015**, *6* (5), 779–783.

(12) Flynn, C. J.; McCullough, S. M.; Oh, E.; Li, L.; Mercado, C. C.; Farnum, B. H.; Li, W.; Donley, C. L.; You, W.; Nozik, A. J.; et al. Site-Selective Passivation of Defects in NiO

Solar Photocathodes by Targeted Atomic Deposition. *ACS Appl. Mater. Interfaces* **2016**, *8*, 4754–4761.

(13) Ros, C.; Fabrega, C.; Monllor-Satoca, D.; Hernández-Alonso, M. D.; Penelas-Pérez, G.; Morante, J. R.; Andreu, T. Hydrogenation and Structuration of TiO_2 Nanorods Photoanodes: Doping Level and the Effect of Illumination in Trap-States Filling. *J. Phys. Chem. C* **2018**, *23*, 3295–3304.

(14) Flynn, C. J.; Oh, E. E.; McCullough, S. M.; Call, R. W.; Donley, C. L.; Lopez, R.; Cahoon, J. F. Hierarchically-Structured NiO Nanoplatelets as Mesoscale P-Type Photocathodes for Dye-Sensitized Solar Cells. *J. Phys. Chem. C* **2014**, *118* (26), 14177–14184.

(15) Dini, D.; Halpin, Y.; Vos, J. G.; Gibson, E. a. The Influence of the Preparation Method of NiOx Photocathodes on the Efficiency of P-Type Dye-Sensitized Solar Cells. *Coord. Chem. Rev.* **2015**, *304–305*, 179–201.

(16) Wood, C. J.; Summers, G. H.; Clark, C. A.; Kaeffer, N.; Braeutigam, M.; Carbone, L. R.; D'Amario, L.; Fan, K.; Farré, Y.; Narbey, S.; et al. A Comprehensive Comparison of Dye-Sensitized NiO Photocathodes for Solar Energy Conversion. *Phys. Chem. Chem. Phys.* **2016**.

(17) D'Amario, L.; Boschloo, G.; Hagfeldt, A.; Hammarström, L. Tuning of Conductivity and Density of States of NiO Mesoporous Films Used in P-Type DSSCs. *J. Phys. Chem. C* **2014**, *118* (34), 19556–19564.

(18) Moot, T.; Isayev, O.; Call, R. W.; McCullough, S. M.; Zemaitis, M.; Lopez, R.; Cahoon, J. F.; Tropsha, A. Material Informatics Driven Design and Experimental Validation of Lead Titanate as an Aqueous Solar Photocathode. *Mater. Discov.* **2017**, *6*, 1–8.

(19) Yu, M.; Draskovic, T. I.; Wu, Y. Cu(I)-Based Delafossite Compounds as Photocathodes in P-Type Dye-Sensitized Solar Cells. *Phys. Chem. Chem. Phys.* **2014**, *16* (11), 5026–5033.

(20) Ahmed, J.; Blakely, C. K.; Prakash, J.; Bruno, S. R.; Yu, M.; Wu, Y.; Poltavets, V. V. Scalable Synthesis of Delafossite $CuAlO_2$ Nanoparticles for P-Type Dye-Sensitized Solar Cells Applications. *J. Alloys Compd.* **2014**, *591*, 275–279.

(21) Yu, M.; Natu, G.; Ji, Z.; Wu, Y. P-Type Dye-Sensitized Solar Cells Based on Delafossite $CuGaO_2$ Nanoplates with Saturation Photovoltages Exceeding 460 mV. *J. Phys. Chem. Lett.* **2012**, *3* (9), 1074–1078.

(22) Wang, J.; Ibarra, V.; Barrera, D.; Xu, L.; Lee, Y.-J.; Hsu, J. W. P. Solution Synthesized P-Type Copper Gallium Oxide Nanoplates as Hole Transport Layer for Organic Photovoltaic Devices. *J. Phys. Chem. Lett.* **2015**, 1071–1075.

(23) Jiang, T.; Bujoli-Doeuff, M.; Farré, Y.; Blart, E.; Pellegrin, Y.; Gautron, E.; Boujtita, M.; Cario, L.; Odobel, F.; Jobic, S. Copper Borate as a Photocathode in P-Type Dye-

Sensitized Solar Cells. *RSC Adv.* **2016**, *6* (2), 1549–1553.

(24) McCullough, S. M.; Flynn, C. J.; Mercado, C. C.; Nozik, A. J.; Cahoon, J. F. Compositionally-Tunable Mechanochemical Synthesis of Zn X Co 3−x O 4 Nanoparticles for Mesoporous P-Type Photocathodes. *J. Mater. Chem. A* **2015**, *3*, 21990–21994.

(25) Mercado, C. C.; Zakutayev, A.; Zhu, K.; Flynn, C. J.; Cahoon, J. F.; Nozik, A. J. Sensitized Zinc–Cobalt–Oxide Spinel P-Type Photoelectrode. *J. Phys. Chem. C* **2014**, *118* (44), 25340–25349.

(26) Peter, L. M. Characterization and Modeling of Dye-Sensitized Solar Cells. *J. Phys. Chem. C* **2007**, *111* (18), 6601–6612.

(27) Labat, F.; Le Bahers, T.; Ciofini, I.; Adamo, C. First-Principles Modeling of Dye-Sensitized Solar Cells: Challenges and Perspectives. *Acc. Chem. Res.* **2012**, *45* (8), 1268–1277.

(28) Bisquert, J.; Fabregat-Santiago, F.; Mora-Seró, I.; Garcia-Belmonte, G.; Gimenez, S. Electron Lifetime in Dye-Sensitized Solar Cells: Theory and Interpretation of Measurements. *J. Phys. Chem. C* **2009**, *113*, 17278–17290.

(29) De Angelis, F.; Di Valentin, C.; Fantacci, S.; Vittadini, A.; Selloni, A. Theoretical Studies on Anatase and Less Common TiO_2 Phases: Bulk, Surfaces, and Nanomaterials. *Chem. Rev.* **2014**, *114* (19), 9708–9753.

(30) Yu, H.; Zheng, X.; Yin, Z.; Tag, F.; Fang, B.; Hou, K. Preparation of Nitrogen-Doped TiO_2 Nanoparticle Catalyst and Its Catalytic Activity under Visible Light. *Chinese J. Chem. Eng.* **2007**, *15* (6), 802–805.

(31) Ba-Abbad, M. M. .; Kadhum, A. A. H. .; Mohamad, A. B. .; Takriff, M. S. .; Sopian, K. . Synthesis and Catalytic Activity of TiO_2 Nanoparticles for Photochemical Oxidation of Concentrated Chlorophenols under Direct Solar Radiation. *Int. J. Electrochem. Sci.* **2012**, *7* (6), 4871–4888.

(32) Xiang, Q.; Yu, J.; Jaroniec, M. Synergetic Effect of MoS_2 and Graphene as Cocatalysts for Enhanced Photocatalytic H_2 Production Activity of TiO_2 Nanoparticles. *J. Am. Chem. Soc.* **2012**, *134* (15), 6575–6578.

(33) Jansons, A. W.; Koskela, K. M.; Crockett, B. M.; Hutchison, J. E. Transition Metal-Doped Metal Oxide Nanocrystals: Efficient Substitutional Doping through a Continuous Growth Process. *Chem. Mater.* **2017**, *29* (19), 8167–8176.

(34) Navas, J.; Fernández-Lorenzo, C.; Aguilar, T.; Alcántara, R.; Martín-Calleja, J. Improving Open-Circuit Voltage in DSSCs Using Cu-Doped TiO_2 as a Semiconductor. *Phys. Status Solidi Appl. Mater. Sci.* **2012**, *209* (2), 378–385.

(35) Zhang, W.; Zhou, W.; Wright, J. H.; Kim, Y. N.; Liu, D.; Xiao, X. Mn-Doped TiO_2 Nanosheet-Based Spheres as Anode Materials for Lithium-Ion Batteries with High

Performance at Elevated Temperatures. *ACS Appl. Mater. Interfaces* **2014**, *6* (10), 7292–7300.

(36) Rimoldi, L.; Ambrosi, C.; Di Liberto, G.; Lo Presti, L.; Ceotto, M.; Oliva, C.; Meroni, D.; Cappelli, S.; Cappelletti, G.; Soliveri, G.; et al. Impregnation versus Bulk Synthesis: How the Synthetic Route Affects the Photocatalytic Efficiency of Nb/Ta:N Codoped TiO_2 Nanomaterials. *J. Phys. Chem. C* **2015**, *119* (42), 24104–24115.

(37) Janisch, R.; Gopal, P.; Spaldin, N. A. Transition Metal-Doped TiO_2 and ZnO—present Status of the Field. *J. Phys. Condens. Matter* **2005**, *17* (27), R657–R689.

(38) Chen, X.; Burda, C. The Electronic Origin of the Visible-Light Absorption Properties of C-, N- and S-Doped TiO_2 Nanomaterials. *J. Am. Chem. Soc.* **2008**, *130*, 5018–5019.

(39) Breault, T. M.; Bartlett, B. M. Lowering the Band Gap of Anatase-Structured TiO_2 by Coalloying with Nb and N: Electronic Structure and Photocatalytic Degradation of Methylene Blue Dye. *J. Phys. Chem. C* **2012**, *116* (10), 5986–5994.

(40) Lu, L.; Xia, X.; Luo, J. K.; Shao, G. Mn-Doped TiO_2 Thin Films with Significantly Improved Optical and Electrical Properties. *J. Phys. D. Appl. Phys.* **2012**, *45* (48), 1764–1769.

(41) Wang, Y.; Hao, Y.; Cheng, H.; Ma, J.; Xu, B. I. N. The Photoelectrochemistry of Transition Metal-Ion-Doped TiO2 Nanocrystalline Electrodes and Higher Solar Cell Conversion Efficiency Based on Zn^{2+} -Doped TiO2 Electrode. *J. Mater. Sci.* **1999**, *34*, 2773–2779.

(42) Jing, L.; Xin, B.; Yuan, F.; Xue, L.; Wang, B.; Fu, H. Effects of Surface Oxygen Vacancies on Photophysical and Photochemical Processes of Zn-Doped TiO_2 Nanoparticles and Their Relationships. *J. Phys. Chem. B* **2006**, *110* (36), 17860–17865.

(43) Brancho, J. J.; Bartlett, B. M. Challenges in Co-Alloyed Titanium Oxynitrides, a Promising Class of Photochemically Active Materials. *Chem. Mater.* **2015**, *27* (21), 7207–7217.

Chapter 7: Conclusions

7.1 Conclusions and Future Work

Although current photocathode performance as a hole transport layer still has yet to match the performance of photoanodes, the allure of a tandem dye-sensitized photoelectrosynthesis cell remains. Advances in understanding how photocathodes operate and what limits their performance present an opportunity for improvements in p-type materials sufficient to meet the requirements for a tandem cell. In this thesis, a variety of tactics were employed to investigate several different candidate materials for the photocathode. The first strategy used was to improve upon the current champion material, NiO, by conformally coating the electrode with a shell of Cu_XO. Although the design of the core-shell NiO/Cu_XO was successfully synthesized for both Cu_2O and CuO, a negligible change in device performance was observed overall. A core-shell architecture may still be viable in the long run with better matched materials.

A DSSC's constituent parts include a mesoporous working electrode, a molecular sensitizer, a redox couple containing liquid electrolyte, and a counter electrode. The primary thrust of much of the work presented here and in the community on the whole centers on fundamentally improving the metal oxide electrode material itself. However, tuning the local environment of the photocathode by adjusting the electrolyte, performance gains can be obtained independently or in addition to material improvements. Exploration of the cation effects in NiO p-DSSCs resulted in the determination that using Mg^{2+} can increase device performance with a notable 60 mV increase

in V_{OC} compared to the most commonly used Li^+. Addressing a complex problem such as the DSPEC often demands isolating certain components, such as the photocathode, but at times observing the system on aggregate can provide insight otherwise unobserved, and re-evaluating initial assumptions can, at times, provide unexpected results.

In addition to pursuing improvements on the current champion material, the exploration of an alternative, $Zn_XCo_{3-X}O_4$ was pursued. A novel mechanochemical synthesis enabled precise tuning of the ratio of Zn^{2+} to Co^{3+} present in the spinel lattice which allowed for precise tuning of several physical and chemical parameters including optical bandgap ranging from 1.85 eV for x = 0 to 2.17 eV for x=1 and mobility ranging from 2.41 x 10^{-5} $cm^2 \cdot V^{-1} \cdot s^{-1}$ for x = 0 to 3.58 x 10^{-4} $cm^2 \cdot V^{-1} \cdot s^{-1}$ for x = 0.75. Despite an increase in mobility as the Zn concentration increases, the DSSC performance still fell short of expectations based on the thin film performance of $ZnCo_2O_4$, and it did not exceed NiO's performance in an analogous cell.[1,2] Small crystal grains and disorder within the lattice likely are contributing high levels of defects reflected in the high doping levels on the order of 10^{20} and are limiting the material's performance overall.

The last venture reported here centers around designing the photocathode material in a fundamentally different fashion. By depositing ultrasmall particles of CuO on a transparent nanoparticulate core (TiO_2 or Al_2O_3), we have enabled the use of a small bandgap material for its electronic properties while maintaining optical transparency. Results show that even on an n-type core of TiO_2, the deposition of CuO results in a hole transport layer that successfully supports cathodic photocurrent. Deposition on two different core materials, TiO_2 and Al_2O_3 demonstrate the generalizability of this approach and indicate its viability in future pursuits for additional applications requiring a hole-transport layer.

Several different approaches have been pursued to improve performance of the mesoporous photocathode for use in a dye-sensitized system. Although all the avenues explored yielded successful p-type DSSCS, the performance has been insufficient to displace the current champion architecture. The demand for a renewable sustainable fuel source requires that we continue to search for a material or combination of materials that meet the needs of a dye-sensitized system. Future work will focus on continuing work on alternative architectures exploiting desirable properties such as valence band positions while circumventing problematic problems such as small bandgaps.

REFERENCES

(1) Mercado, C. C.; Zakutayev, A.; Zhu, K.; Flynn, C. J.; Cahoon, J. F.; Nozik, A. J. Sensitized Zinc–Cobalt–Oxide Spinel P-Type Photoelectrode. *J. Phys. Chem. C* **2014**, *118* (44), 25340–25349.

(2) Flynn, C. J.; Oh, E. E.; McCullough, S. M.; Call, R. W.; Donley, C. L.; Lopez, R.; Cahoon, J. F. Hierarchically-Structured NiO Nanoplatelets as Mesoscale P-Type Photocathodes for Dye-Sensitized Solar Cells. *J. Phys. Chem. C* **2014**, *118* (26), 14177–14184.